Dielectric studies of some oxide materials, nitride ceramics and glasses

Md. Akhtaruzzaman

DIELECTRIC STUDIES OF SOME OXIDE MATERIALS,

NITRIDE CERAMICS AND GLASSES

by

Md. Akhtaruzzaman, M.Sc.

(Graduate Society)

A Thesis submitted to the University of Durham in candidature for the degree of Doctor of Philosophy

February, 1989.

Dedicated to the memory of those to whom
I lost forever during my course of research
and to the struggle against Oppression, Evil
and Discrimination.

ABSTRACT

This thesis is primarily concerned with the evaluation and comparison of the dielectric behaviour of materials which may find application as substrates in microelectronic high-performance packaging. In the introductory chapter the factors governing the choice of the most suitable dielectric substrate for compatibility with silicon technology are reviewed; it is shown that in addition to good dielectric properties the thermal conductivity is important if high power packages are required together with the ability to obtain good matching of thermal expansion coefficients. This is followed by a survey of the present theories of dielectric behaviour with special emphasis on the Universal law of dielectric response and its applicability to oxide and glass ceramics which exhibit hopping conductivity. The experimental methods for the measurement of dielectric parameters are outlined in Chapter 3 which includes an account of techniques developed for studying materials only available as powders. The three substrate systems studied were aluminium oxide, aluminium nitride and glass-on-molybdenum and in the case of the two former materials a range of both pure and impure specimens were examined both in single crystal and sintered polycrystalline form. The detailed experimental results are presented and discussed in the three succeeding chapters for each of the materials in turn; these results include the values of permittivity and dielectric loss, measured over a frequency range of 5×10^2 Hz to 1×10^7 Hz, the temperature variation of permittivity both in the low temperature (85K to 293K) and high temperature (20°C to about 600°C) regions and the d.c. and a.c. conductivity in the high temperature range. In their pure form each of these materials would be suitable as a substrate, having permittivities at room temperature of $\epsilon'_s = 10.2$ for polycrystalline Al_2O_3, $\epsilon'_s = 9.2$ for polycrystalline AlN (which has a thermal conductivity of about

one-hundred times that of alumina) and $\epsilon'_s = 6.5$ for glass-on-molybdenum and dielectric losses in the region of $\tan\delta \sim 10^{-3}$. The effect of impurities is shown to be very significant leading in all cases to some increase in permittivity and a much larger increase in dielectric loss. The measurements made on powders are given and discussed in Chapter 7. In the studies on the powders used as starting materials for the manufacture of substrates it was shown that by making measurements at low temperature (77K) the effects of intergranular space charge polarization could be overcome yielding information valuable for quality control of impurity content; measurements made on powders of some high temperature oxide superconducting materials are also given. The final chapter, Chapter 8, summarises the overall conclusions of the research and makes some suggestions for future work.

ACKNOWLEDGEMENTS

I would especially like to express my gratitude to my supervisor, Dr.J.S.Thorp, for his unfailing guidance, advice and every possible help throughout the work and the preparation of this thesis; he has made this very pleasant. To him, I owe special thanks and outstanding appreciation.

My sincere thanks to Professor J.Woods for giving me access to the facilities of the Applied Physics Group, School of Engineering and Applied Science, the technical staff, especially to Mr.C.Savage, Mr.J.Gibson, Mr.M.Wilson, and others for their help in the construction of apparatus. I appreciate the cooperation that I received from Mr.E.Evangelinos regarding the basic high frequency measurement techniques and also others, especially to Dr.B.L.J.Kulesza, in that group. Regarding structural and microstructural studies, I am thankful to Dr.G.J.Russell (deceased) and Mr.N.F.Thompson for their help. I am also thankful to Dr.Haider Al-Allak and Dr.Abdullah Al-Dhafiri for their advice and discussion from time to time. I owe very much to my parents, sister, well wishers, friends and departmental colleagues at home who extended their encouragement and sympathy during the tenure of my research.

I am especially thankful to my wife, Mrs.Mohua Zaman, for her constant support, help and encouragement towards me and her patience in many difficult situations. I would like to extend my gratitude to the Commonwealth Scholarship Commission in the United Kingdom for the award of the Commonwealth (academic staff) Scholarship, and to the University of Rajshahi, Bangladesh, for granting study leave. Thanks are also extended to Mrs.S.Mellanby for typing this thesis.

M. Akhtaruzzaman

CONTENTS

CHAPTER ONE

INTRODUCTION

1.1

In the past few decades (from the 1950's to the present) there has been a tremendous development in the electronic industry. Dielectric materials have found ever increasing uses and potential uses in the fabrication of components and devices. For example, dielectric thin films with islands of metal interspersed in them, usually known as "cermets", are used as resistors in the production of integrated circuits (IC's). Solid bulk dielectrics of several types of material, including polymers, are used in capacitor manufacture. In a different area, that of microelectronics, the thin film dielectric is found to be essential in the stages of fabrication in order to provide insulation between, for example, the channel and the gate in a field effect transistor (FET); these very thin insulating layers (e.g. of SiO_2 or Si_3N_4), are usually formed by oxidation or nitridation respectively of the silicon as the devices are made. Again, the piezoelectric property of some dielectric materials (e.g. quartz) has found very wide use in transducers in applications ranging from crystal controlled oscillators and frequency standards to the generation of acoustic waves in ultrasonic detection techniques and sonar. Another important area is the use of dielectric materials showing ferroelectric to paraelectric transitions for opto-electronic devices; here the main requirements are for high speed switching of laser or other beams of light from one direction to another which is accomplished by utilizing the two states of the dielectric. A well established but nonetheless very important area is that of electrical appliances (e.g. transformers, motors, heating elements, cables and insulated wires) where the insulating properties of the dielectric materials are exploited.

In particular, within the general field of the design, fabrication and production of micro-electronic components there is a more specific area concerned with the problems of packaging high performance devices. In turn, the factors involved in the provision of high performance packages may themselves be subdivided, for example, into those concerned primarily with the silicon chip design and manufacture, photolithography or screen-printing of circuitry and connecting leads, the electrical characterization of the assembly, the provision of special materials for construction and bonding and matters to do with hermeticity and environmental testing. The topics discussed in this thesis relate to one such important aspect of packaging, namely the provision of the most appropriate dielectric substrate on which to mount the silicon chip.

It is perhaps helpful here to outline the main features of a high performance package so that an appreciation can be gained of the factors influencing the choice of substrate material. The arrangement is illustrated diagrammatically by the exploded view given in Fig (1.1). The silicon chip is bonded to a dielectric substrate on which conductor tracks (the input/output leads) are deposited, usually by screen-printing techniques. Connections from these input/output leads to external circuitry are made via a lead frame. To ensure both hermetic sealing and some degree of overall electrical shielding, a ceramic lid support is also mounted on the substrate with a metal or metallised ceramic lid on top. As silicon devices become larger and operating frequencies rise, the device performance is increasingly affected by the type of package used to house the chip. It is found that one of the major problems encountered, in particular with large, high speed devices, is that of heat dissipation since the silicon chip is acting as a heat source of significant magnitude. Being of course a semiconductor, the electrical behaviour of the chip is strongly

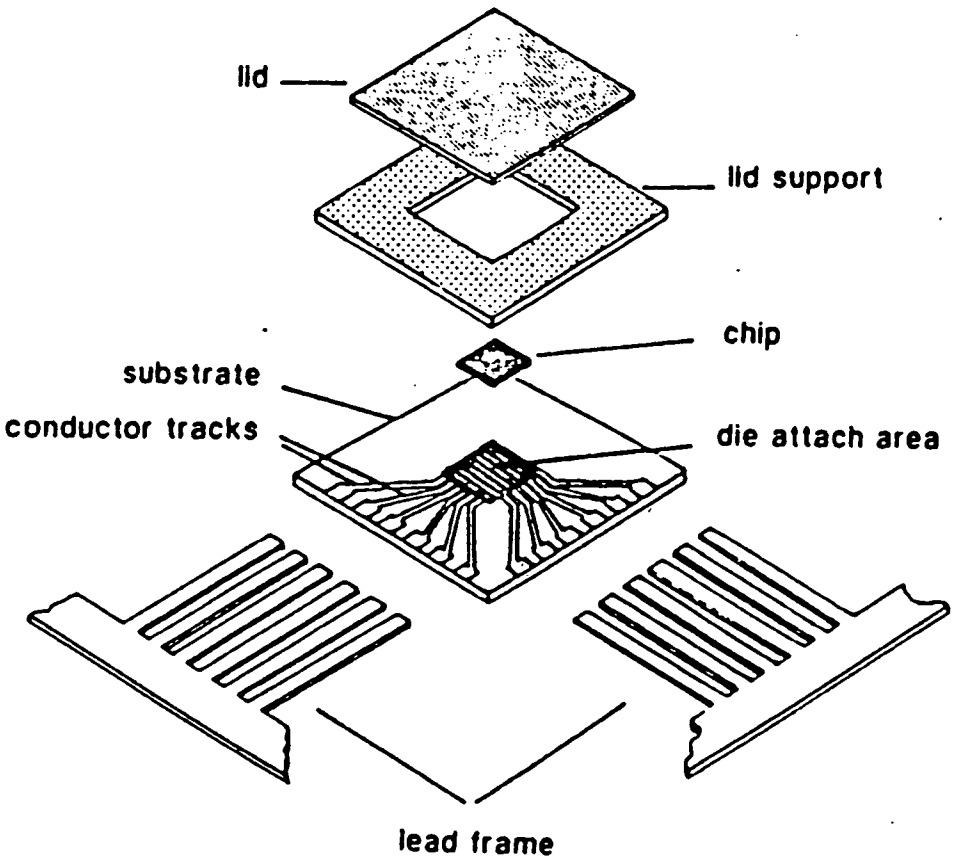

Figure 1.1 Exploded view of a package

temperature dependent and hence it is essential to drain away this heat input so that the temperature of the silicon can be kept within very tightly controlled limits. This focuses attention on the need for good thermal conductivity of the substrate material. Conventional ceramic packages (based on alumina substrates) often perform poorly in this respect. Several solutions have been proposed, including the use of aluminium nitride (which has a value of thermal conductivity nearly a hundred times greater than that of aluminium oxide) and copper-tungsten inserts. Although these materials have adequately large thermal conductivities to meet current power dissipation requirements they do not yet provide a cheap, easily produced, alternative to alumina and have not yet achieved widespread use in microelectronic packaging. Thus there is still a requirement for a substrate which can combine high thermal conductivity and good electrical performance with relatively low cost and production by conventional processing routes. The glass-on-metal substrates aim to fill this need. In these a thin layer of glass-ceramic provides an electrically insulating material on which to print the conductor tracks and by ensuring that the glass-ceramic does not cover the central well (the die attach area) it is possible to remove heat from the device directly into the metal base. There are other reasons why the glass-on-metal systems look attractive. Unfortunately, it is not possible to choose materials for the substrate on the basis of their thermal conductivities alone. During operation the temperature of a device and its surroundings may rise by large amounts. If the thermal expansion coefficients of the device and the metal substrate are not the same the device may become stressed as thermal cycling takes place and this would lead to reduced performance. This consideration precludes the use of materials such as copper which, in addition to having a high thermal conductivity, has a very high thermal coefficient of expansion of about 14.1×10^{-6} $^{\circ}C^{-1}$;

Since that of a silicon device is $3.0 \times 10^{-6}\ °C^{-1}$, this would give an unacceptable thermal expansion mismatch. In choosing a metal or alloy for the substrate base (the heat sink) a thermal coefficient of expansion mismatch not exceeding $2 \times 10^{-6}\ °C^{-1}$ would be preferred. This limits the selection to the pure metals tungsten and molybdenum (having thermal expansion coefficients of $4.4 \times 10^{-6}\ °C^{-1}$ and $5.5 \times 10^{-6}\ °C^{-1}$ respectively) and a composite structure of copper/invar/copper layers ($3 \times 10^{-6}\ °C^{-1}$). The problem of matching thermal expansion coefficients is not limited to the metal base. Although the glass ceramic is not in contact with the device it must be firmly bonded to the metal ; one of the main requirements for this is that there should be very little thermal expansion mismatch. If this mismatch is greater than about $2 \times 10^{-6}\ °C^{-1}$ the interface becomes excessively stressed on cooling from the firing temperature and the glass-ceramic coating may either become detached from the metal or cause the whole substrate to bow. In contrast to the behaviour of a glass (in which the thermal expansion coefficient is fixed by the composition) the ability to adjust the proportion of crystalline phases in a glass ceramic by controlling the heat treatment gives a degree of flexibility in the thermal expansion of the overall material. An alternative and simpler way of controlling the thermal expansion coefficient of a glass ceramic is to adjust the composition of the original glass (prior to heat treatment), the heat treatment cycle and the addition of nucleating agents so that the amount of crystalline phase having too high an expansion coefficient is just balanced by the amount of that which has too low an expansion. This procedure can allow very fine control of the thermal expansion coefficient of the final glass ceramic and is one of the main reasons for the potential importance of the glass-on-metal systems as substrates.

The main part of the thesis describes studies of the dielectric

characteristics of three potential substrate materials for high performance packaging, aluminium oxide, aluminium nitride and glass-on-molybdenum. It has been established from previous dielectric studies (in this Research Group) that in some similar materials (e.g. magnesium oxide, Thorp and Rad, (1.1); Thorp, Kulesza, Rad, (1.2); Silicon nitride, Thorp and Sharif (1.3), and a series of oxide and oxy-nitride glasses, Thorp and Kenmuir (1.4), the dominant conductivity mechanism is hopping, Jonscher (1.5), and a central objective was to establish whether this also held for these substrate materials. A related objective, important for its potential importance in connection with quality control during manufacture and production, was to examine the role of impurities in influencing the dielectric behaviour. Chapter 2 gives a brief review of the current ideas on dielectric theory including a summary of the requirements necessary when allowing for the porosity of sintered polycrystalline materials and addition formulae suitable for dealing with composite dielectrics. In Chapter 3 descriptions are given of the main experimental techniques employed for dielectric measurement ; these include primarily the Bridge methods for the frequency range 5×10^2 Hz to 3×10^4 Hz and the extension, using the Q-meter, to an upper frequency limit of around 1×10^7 Hz. Details are also given in Chapter 3 of the adaptations required to permit measurements to be made in the low temperature range (i.e. 85 K to 290 K) and the high temperature range (20°C to 700°C). The results obtained for the three groups of substrate materials, (alumina, aluminium nitride, and glass-on-metal) are presented and discussed in Chapters 4, 5 and 6 respectively.

During the studies on the dielectric substrates, most of which had been supplied as sheets of polycrystalline sintered solids, it became apparent that it would be very helpful to develop methods for making dielectric measurements on powders, since the quality of the starting

materials (and the effects of some subsequent intermediate steps in the fabrication process) could then be monitored, so giving the potential for much enhanced quality control of fabrication routes. The development of measurement techniques for powders is described in Chatper 3, permitted some dielectric studies to be made of powders (specifically aluminium oxide, aluminium nitride, magnesium oxide and magnesium nitride) of materials used either for appraisal of the technique or as starting materials for substrate manufacture and also on some oxide superconductors and related materials; this work is presented in Chapter 7. The final chapter, Chapter 8, summarises the main conclusions of the research and makes some suggestions for future work.

CHAPTER ONE

REFERENCES

1.1 J.S.Thorp and N.E.Rad, J.Mat.Sci., 16 (1981) 255.

1.2 J.S.Thorp, B.L.J.Kulesza and N.E.Rad, J.Mat.Sci., 16 (1981) 1052.

1.3 J.S.Thorp and R.I.Sharif, J.Mat.Sci., 12 (1977) 2274.

1.4 J.S.Thorp and S.V.J.Kenmuir, J.Mat.Sci., 16 (1981) 1407.

1.5 A.K.Jonscher, Nature, 267 (1977) 673.

CHAPTER TWO

DIELECTRIC THEORY

2.1 Dielectric Properties of Materials

Any dielectric material, when subjected to an electric field, is characterized by a complex quantity, generally known as the complex dielectric constant or permittivity. This physical parameter is extremely important and will be considered prior to any specific fields of application. The complex dielectric constant is usually denoted by ϵ^*. It is usually written as $\epsilon^* = \epsilon_o$ for free space where

$\epsilon_o = \frac{10^7}{4\pi c^2} = 8.8542 \times 10^{-12}$ F m^{-1} and 'c' is the velocity of light.

The quantity ϵ^* is often used in the form of a normalized complex dielectric constant, ϵ_r or relative permittivity, i.e.

$$\epsilon_r = \frac{\epsilon^*}{\epsilon_o} = \epsilon' - j\,\epsilon'' \qquad (2.1)$$

For free space its value is equal to unity. Separating the real and imaginary parts of both sides gives,

$$\epsilon' = \text{Real}\left(\frac{\epsilon^*}{\epsilon_o}\right) \qquad (2.2)$$

and

$$\epsilon'' = \text{Imaginary}\left(\frac{\epsilon^*}{\epsilon_o}\right) \qquad (2.3)$$

where ϵ' and ϵ'' are real and imaginary components of the complex dielectric constant respectively. In these relations ϵ' represents the amount of energy which can be stored by the applied electric field in a dielectric material; alternatively, it can be thought of as a

parameter of the dielectric that determines its ability to form a capactor since insertion of a slab of dielectric in a capacitor increases the capacity by a factor of ϵ'. On the otherhand, the imaginary part, ϵ'' is a direct measure of how much energy is dissipated in the form of heat. The relative permittivity, ϵ_r, can be written as,

$$\epsilon_r = \epsilon' (1-j \tan\delta) \tag{2.4}$$

where

$$\tan\delta = \frac{\epsilon''}{\epsilon'} \tag{2.5}$$

The loss tangent, $\tan\delta$, is equal to the ratio of the power lost in heat to the energy stored per cycle in the dielectric material. The real and imaginary components of the complex permittivities are shown by the phasor diagram in (Fig 2.1). For small values of the angle δ, $\tan\delta \simeq \sin\delta$. The quantities ϵ' and ϵ'' are both dimensionless because all values are relative to free space. Therefore they preserve their values irrespective of the selected system of units.

2.2 Polarization

2.2.1 General Description

The dielectric materials have large bandgaps in comparison with semiconductors and metals. Consequently, in an ideal case it is assumed that, at room temperature, there is no free charge in it. However, application of an electric field changes the effective centres of gravity of the positive and negative charges from their original concentric positions (in case of non-polar materials) resulting in polarization. This polarization depends on the total electric field in the material, i.e.

$$\vec{P} = \alpha \vec{E} \tag{2.6}$$

where $\vec{P}$ is the polarization,

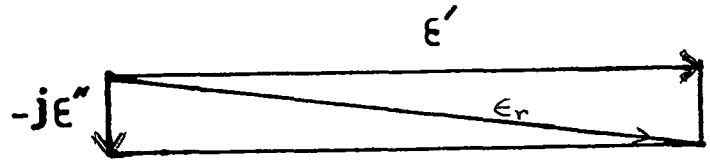

Fig. 2,1 Phasor diagram of ε′ and ε″.

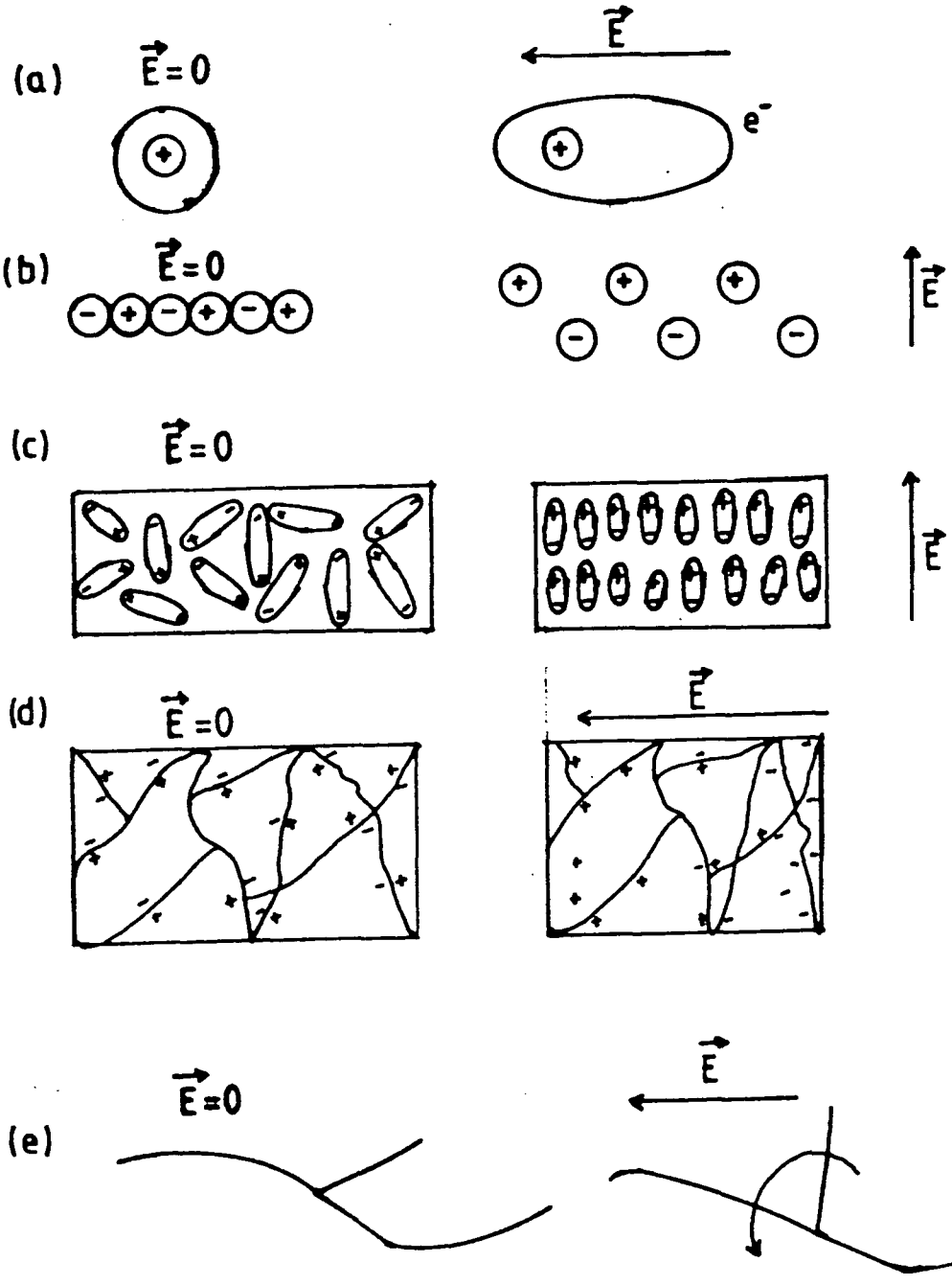

Fig. 2,2 Schematic diagram of polarization mechanisms (with and without electric field.)

(a) Electronic, (b) Ionic, (c) Dipolar (d) Interfacial and (e) Structural polarization.

α is the polarizability factor and

$\vec{E}$ is the electric field.

However, the polarization can also be defined as the electric dipole moment per unit volume, i.e. it is the sum of 'n' electric dipole moments in a unit volume,

$$\vec{P} = \sum_{i=1}^{n} \vec{P}_i \qquad (2.7)$$

From these twin standpoints it can be seen that the degree of the polarization depends both on the electric field and on the arrangement of the atoms in the material. In isotropic materials, the polarization is in the same direction as the electric field causing it and the polarizability is a scalar quantity. In anisotropic materials the polarization has different values in different directions, so 'α' will be a tensor quantity.

The polarization $\vec{P}$, the electric displacement $\vec{D}$ and the electric field $\vec{E}$ are related by

$$\vec{D} = \vec{P} + \epsilon_o \vec{E} \qquad (2.8)$$

and

$$\vec{D} = \epsilon_o \epsilon_r \vec{E} \qquad (2.9)$$

From equations (2.8) and (2.9) one obtains

$$\vec{P} = \epsilon_o \vec{E} (\epsilon_r - 1) \qquad (2.10)$$

where $\vec{P}$ is the polarization

$\vec{E}$ is the electric field

ϵ_r is complex relative permittivity.

There are five main mechanisms of polarization, namely

1. Electronic polarization.
2. Ionic polarization.
3. Dipolar polarization.
4. Interfacial or space-charge polarization.

5. Structural dipole polarization.

Some schematic diagrams of the polarization mechanisms are shown in (Fig 2.2a to 2.2e).

2.2.2 Electronic Polarization

In any material, the positive atomic nucleus is surrounded by the electrons orbiting in different orbitals. Depending on the arrangement of the atoms, there may or may not be an electric dipole moment in the system. If the effective centre of the negative charges is concentric with the effective centre of the positive charges, then there exists no initial dipole moment in the system. By applying an external electric field to the material, the electrons are slightly displaced relative to the nucleus and an electric dipole moment is created; electronic polarization has occurred in the system. It is shown schematically in (Fig 2.2a). The time required for establishing this polarization is of the order of 10^{-15} seconds which corresponds to the ultraviolet range of frequency. Since this mechanism of polarization occurs in all atoms or ions, it can be observed in all dielectrics irrespective of whether other types of polarization are present in the system. This polarization satisfies Maxwell's theory, i.e.

$$\epsilon' = \mu^2 \qquad (2.11)$$

where μ is the refractive index of the dielectric medium at optical wavelengths.

2.2.3 Ionic Polarization

In ionic or partially ionic dielectric materials the presence of an electric field displaces the ions from their equilibrium positions producing an induced electric moment. The time required for this polarization is of the order of 10^{-13} to 10^{-12} seconds and is longer than for electronic polarization. This polarization also arises from the displacement of the nuclei and it is frequency dependent in the infra-red region, when the applied frequency approaches that of the

molecular vibration. This polarization does not satisfy Maxwell's equation (2.11); in this case $\epsilon' > \mu^2$.

2.2.4 Dipolar Orientation

The application of an external electric field to a dielectric medium tends to align the dipoles present in the system with the applied field. The dipoles are pairs of oppositely charged electric charges with equal magnitude (in charge) displaced by arbitrary distances of the order of the atomic dimensions. However, the orientated dipoles reduce the effective field in the system by opposing the applied field in it.

The orientation of the molecules is opposed by their thermal motion, which varies with temperature. As a result at high temperatures the thermal motion practically prevents the orientation of the molecules and hence the polarization should be reduced.

Debye has derived the polarization for polar molecules and showed that molecules with zero rotational energy contribute to orientational polarizability and that the number of this kind of molecule decreases with increasing temperature. Dipole polarization can appear in pure form only in gases, liquids and amorphous bodies.

In crystalline solids at temperatures below the melting point, the dipoles are frozen and so they cannot be oriented and dipole polarization cannot occur in them.

2.2.5 Interfacial or Space Charge Polarization

This kind of polarization arises when there is an interface between the two media which forms a space charge region. It is found in polycrystalline materials and is associated with grain boundaries. Imperfections of crystallinity and impurity, atoms of different radius to those of the dielectric medium may give rise to this polarization. It is prominent at the very low frequencies (< 1Hz in single crystal; < 5.0 kHz in compacted powders) and found to be sensitive to temperature.

At low temperature, this polarization disappears [2.1-2.3]. Also with increasing frequency this polarization decreases rapidly.

2.2.6 Structural Dipole Orientation

There are branches present in the polymeric materials. In an external electric field these branches rotate by taking different positions, relative to each other. This causes structural dipole orientation. Further examples occur in liquids, e.g. aldehydes, ketones and aromatic compounds, where the side group can easily rotate in an external electric field causing different dipole moments and ultimately resulting in different dielectric constants of the different isomers of the material (Fig 2.2e).

2.3 Debye Equations ; The Frequency Dependencies of ϵ' and ϵ''

Debye formulated his theory of the frequency dependence of the complex permittivities mainly for gas and liquid dielectrics in the light of Clausius-Mosotti's internal field concept. Polar and non-polar dielectrics and their behaviour with frequency and temperature received much attention in his work. In a dielectric of any kind, it is possible for several polarization mechanisms to be present each contributing differently depending on ratios of the times of polarization with the period of the applied field. In dielectrics with dipolar polarization, the time required for polarization to occur is comparable with the applied field resulting in frequency dependencies of the complex permittivities. This introduces the concept of the Debye relaxation time, τ_D which can be defined as the time in which the polarization is reduced to 1/e times its original value. Debye states that dielectric relaxation is the lag in dipole orientation behind the applied alternating electric field. The relaxation time τ_D, depends on various factors, such as the viscosity of the medium, the size of the polar molecules, the frequency and the temperature of the material. If the polar molecules are large, or the

viscosity of the medium is high, or the frequency of the applied field is high, the rotary motion of molecules becomes out of step with the field and the polarization will acquire an out-of-phase component. Thus the displacement current acquires a conductance component in phase with the field which results in a thermal dissipation of energy (Fig 2.3).

The dependencies of ϵ' and ϵ'' on frequency are shown in (Fig 2.4a and 2.4b). As the frequency is increased, it is reasonable to expect that the total polarization will decrease and hence ϵ' will decrease. All of the energy applied to the material by the electric field is not used to orient the dipoles, but some is lost to the material by increasing the random thermal motion that exists in every substance. Therefore as ϵ' decreases, ϵ'' should increase. This phenomenon is shown in (Fig 2.5).

The reduction in ϵ' in the frequency region near 10^6 Hz is due to dipolar polarization, whereas at regions near 10^{12} and 10^{15} Hz, atomic and electronic polarizations are responsible. As the frequency increases above $f = 10^6$ Hz the contribution of the dipole orientation eventually disappears, and the permittivity levels off at a lower value ϵ_∞. Where $f > 10^{15}$ Hz, i.e. in the visible frequency range, a final limiting value of $\epsilon' = \mu^2$ (Maxwell's equation) can be reached. At zero frequency (d.c. field), $\epsilon' = \epsilon_s$, where ϵ_s is equal to the static value of dielectric constant.

There are relations between ϵ_∞, ϵ_s, frequency and τ_D which are called Debye equations [2.4]. These can be derived from the relation

$$\epsilon^* = \epsilon_\infty + \frac{\epsilon_s - \epsilon_\infty}{1 + j\omega\tau} \qquad (2.12)$$

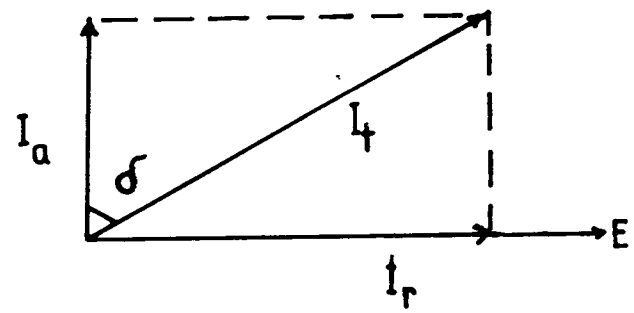

Fig. 2.3 Loss component (I_r) of the applied current in phase with the applied field.

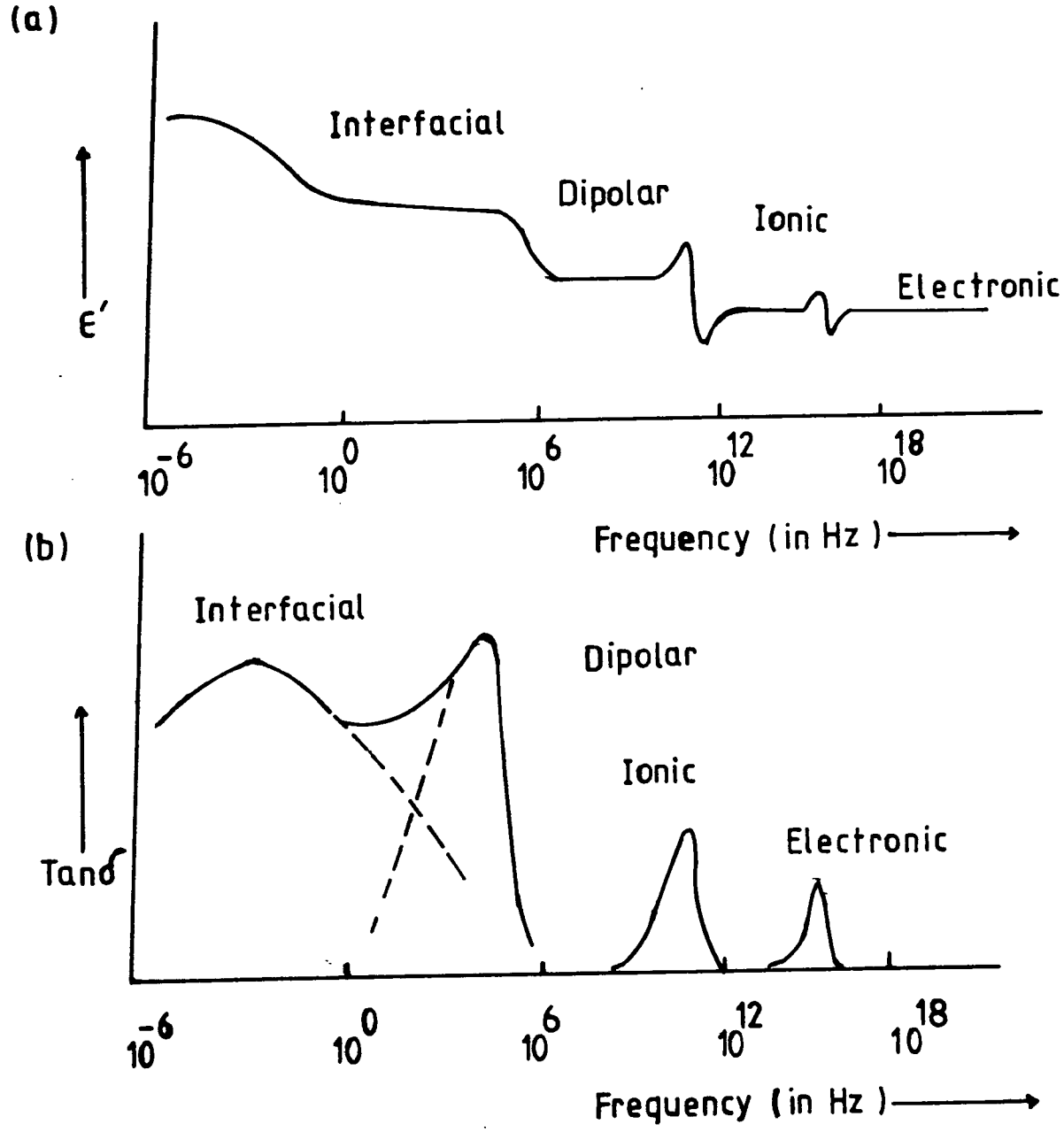

Fig. 2.4 (a) Variation of dielectric permittivity with frequency.
(b) Variation of dielectric loss with frequency.

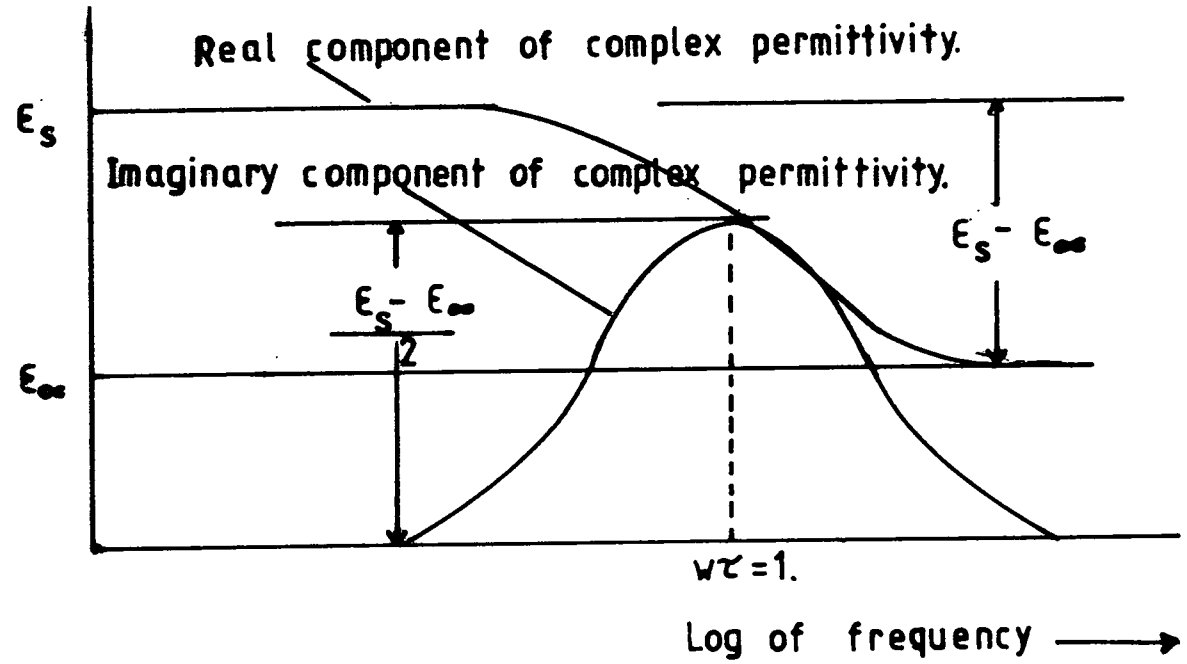

Fig. 2.5 Variation of real and imaginary components of complex permittivity with frequency for Debye relaxation.

Introducing $\epsilon^* = \epsilon' - j\epsilon''$ and comparing real and imaginary parts yields,

$$\epsilon'(\omega) = \epsilon_\infty + \frac{\epsilon_s - \epsilon_\alpha}{1 + \omega^2 \tau_D^2} \tag{2.13}$$

and $$\epsilon''(\omega) = \frac{(\epsilon_s - \epsilon_\alpha)\omega\tau_D}{1 + \omega^2 \tau_D^2} \tag{2.14}$$

where ϵ^* is the complex permittivities

τ_D is the Debye relaxation time

ϵ_s is the static value of the dielectric constant

ϵ_α is the limiting value of the dielectric constant

ω is the angular frequency.

The equations (2.13) and (2.14) are the well-known Debye equations. When $\omega\tau = 1$, a loss peak is obtained. The ratio of the equations (2.14) and (2.13) is

$$\frac{\epsilon''(\omega)}{\epsilon'(\omega) - \epsilon_\alpha} = \omega \tau_D \tag{2.15}$$

and depends on the frequency and the relaxation time.

These equations are plotted in (Fig 2.5). Eliminating $\omega \tau_D$ between equations (2.13) and (2.14) gives

$$\left[\epsilon' - \frac{\epsilon_s - \epsilon_\alpha}{2}\right]^2 + \epsilon''^2 = \left[\frac{\epsilon_s - \epsilon_\alpha}{2}\right]^2 \tag{2.16}$$

which is the equation of a circle. Since $\epsilon'' > 0$ a semicircle will be physically meaningful. The Debye semicircle has the advantage of giving a representation of a simple relaxation process when the relative permittivities ϵ' and ϵ'' are plotted on a complex plane.

The a.c. electrical conductivity can be represented by

$$\sigma_{a.c.}(\omega) \propto \frac{\omega^2}{1 + \omega^2 \tau^2} \qquad (2.17)$$

This applies only for dipolar processes. As can be seen at frequencies $f < \frac{1}{\tau}$, $\sigma_{a.c.}$ is proportional to ω^2. This result differs from that obtained on the hopping model.

2.4 The Jonscher Universal Law ; the Screened-Hopping Model

There are several theories existing at the moment to explain the origin and behaviour of dielectric materials [2.5]. The traditional approach to the interpretation of the frequency dependence of the dielectric loss is based on the Debye polarization mechanism for which the complex dielectric susceptibility $\chi(\omega)$ is given by [2.6].

$$\chi(\omega) = \chi'(\omega) - i\chi''(\omega) = [\epsilon'(\omega) - \epsilon_\infty]/\epsilon_o$$
$$= (1 + i\omega\tau)^{-1} \qquad (2.18)$$

where $\epsilon'(\omega)$ is the complex dielectric permittivity at radian frequency ω,

ϵ_∞ is the limiting high-frequency value of $\epsilon'(\omega)$,

ϵ_o is the permittivity of free space,

χ' is the real component of the complex susceptibility,

χ'' is the imaginary component of the complex susceptibility.

Using the universally applicable Kramers-Kronig relation, the Debye dielectric behaviour takes the following form

$$\frac{\chi''(\omega)}{\chi'(\omega)} = \omega\tau \qquad (2.19)$$

which shows that the ratio of the energy lost to the energy stored in the dielectric system per cycle is not constant but rather depends on the relaxation time, τ. It is relevant to point out here that the Debye interpretation of dielectric polarization was entirely based on the experimental data from the non-interacting substances like gases, vapours and liquids containing a very small concentration of polar molecule in a non-polar solvent. On the otherhand, in solids, the interactions between the atoms and molecules are quite different from those occuring in gases and liquids.

There are two different approaches to treat the dynamics of dielectric polarization: (a) the molecular dipoles and (b) hopping. Again, the "sequential hopping" model is in many ways equivalent to the former approach, replacing the distribution of dipolar relaxation times with a corresponding distribution of hopping times; it also accounts for the d.c. conductivity in the limit of zero frequency. The hopping model predicts that there is no correlation between d.c. conductivity σ_o, and a.c. conductivity $\sigma(\omega)$; it also predicts that $\sigma(\omega)$ is pressure independent but that the d.c. conductivity σ_o does depend on pressure [2.7]. Jonscher has introduced a new "Universal Law" to treat the dynamics of dielectric polarization as a many-body interaction based on a screened-hopping model [2.8]. An earlier attempt to explain the a.c. conductivity mechanism in disordered solids in terms of many-body interactions was made by Pollak and Pike, who associated it with atomic movements and the specific heat anomaly [2.9]. However, the dielectric response of solids based on Jonscher's model does find striking parallels in other branches of physics involving theoretical expressions for time-dependent responses resulting from many-body interactions. According to Jonscher the conditions that must be satisfied in a dielectric system for the Kramers Kronig criterion [2.6,2.7] to apply are: (1) discontinuous hopping of charges between

localised positions, and (2) the presence of a screening-charge adjusting slowly to the rapid hopping.

The first point can be visualised in the following way:

In a conventional picture hopping occurs between two localised levels, each of which is uniquely defined in space and in energy (Fig 2.6a). This model is applicable to media in which the polarization responds sufficiently rapidly. On the otherhand, if the polarization of the dielectric medium responds relatively slowly in comparison with the time taken by the tunnelling process, then the energy level picture must be modified to that shown in (Fig 2.6b). The "empty" and the "occupied" states are separated by a polarization energy W_p, due to the relaxation of the surrounding - lattice and carriers.

In the latter case, the transition from a localised level "i", into an equivalent unoccupied level "j" having the same energy may be considered to occur in three stages (Fig 2.6c). Process (1) is the thermal excitation of the carrier into a virtual state corresponding to the unrelaxed energy of an empty state. The following tunnelling transition (2) is not activated and the process is completed by a gradual relaxation, (3), into the ground state of the newly occupied centre. For this mechanism to be applicable, the equilibrium transition time τ_o, should satisfy the condition $\tau_o \gg \tau_D$, where τ_D is the relaxation time for the polarization process, since otherwise the carrier would be re-excited before it has had a chance to relax. This condition may be expected to be satisfied at low temperatures, such that $kT < W_p$. At higher temperatures the system becomes effectively the same as the model of (Fig 2.6a). This corresponds to a rapidly polarizable medium, since in this case the model has no time to respond to the rapid transition rate and adjusts itself only to the mean occupancy.

The second condition regarding the presence of screening-charge

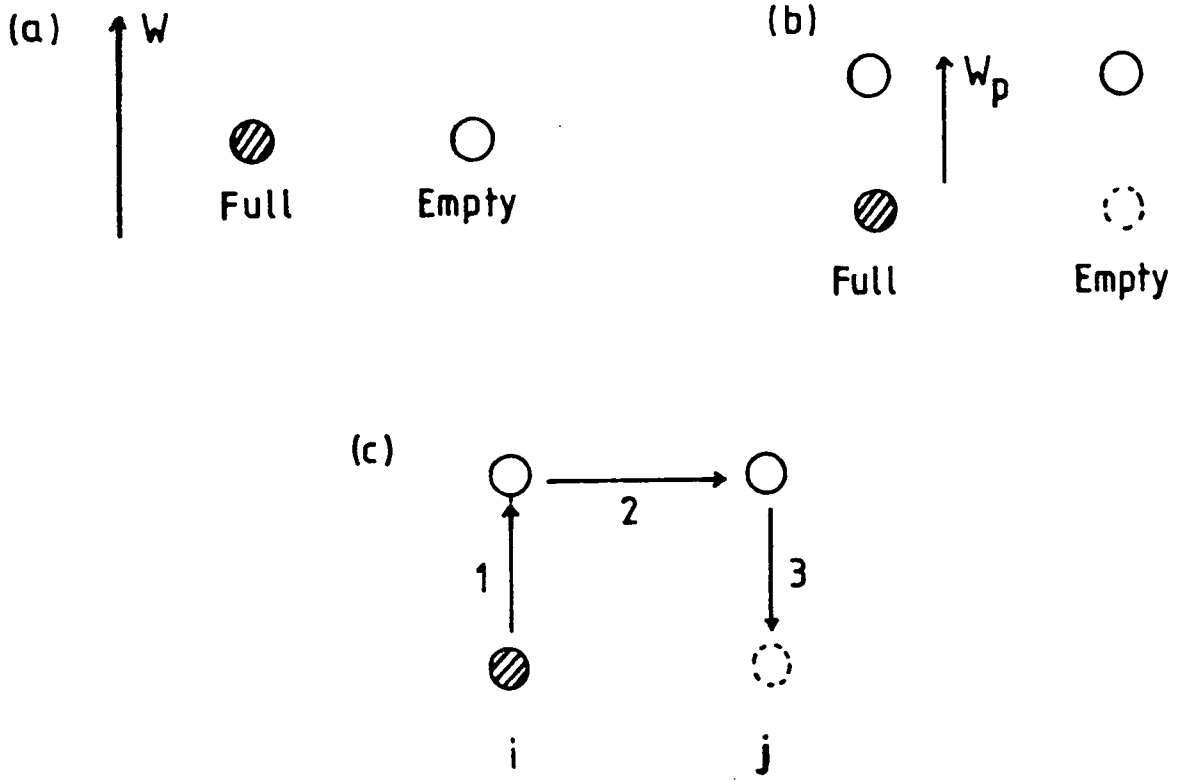

Fig. 2.6 Localised energy levels in hopping between pairs or centres.

(a) Hopping in a medium in which polarization relaxes very rapidly —— the conventional hopping system.

(b) Full and empty centres in a medium in which polarization relaxes slowly;

(c) Three stages of hopping between two centres as in (b).

adjustment leads to the following picture (Fig 2.7). In this aspect of the Jonscher model, the dielectric material is considered to contain a certain density of localised charges. Some of these may be able to hop over many consecutive sites, ultimately giving rise to a d.c. conductivity σ_o. Others may be restricted to shorter ranges with the limiting case of pairs of hopping sites. It should be noted here, however, that the free carrier conduction in the conduction and valence bands lies outside this model. A charge +q localised on a site 'i' imposes a Coulomb-like potential on the surrounding medium and this tends to repel like charges and to attract any oppositely charged particles that may be present in the neighbourhood thus bringing about a partial screening of the charge in question. In a system consisting of localised charges the screening would not be as complete as that due to free charges, since localised charges are not quite free to assume the exact local density demanded by the local value of the potential. This results in the effective value of q on site 'i' to be reduced to some smaller value pq where $p < 1$.

If the charge in question makes a rapid hopping transition to a neighbouring site 'j' through a distance $|\vec{r}_{ij}|$, the screening charge will initially be left behind on site 'i', so that the initial change of polarization is $q|\vec{r}_{ij}|$ and this only gradually decreases to $pq|\vec{r}_{ij}|$ as the screening readjusts itself to the new position of the charge at 'j'. This adjustment time is loosely termed as the relaxation time τ_r. Assuming that the charge remains at site 'j' for a time longer than τ_r ($\tau_r < \tau_D$), the sequence of events involved in a hopping transition may be visualised with reference to (Fig 2.7A). The reduction of the resulting polarization from $q|\vec{r}_{ij}|$ to $pq|\vec{r}_{ij}|$ corresponds to the reduction of the potential energy of the system and the energy loss involved is dissipated through the phonon system. The opposite case where $\tau_D \ll \tau_r$ is more likely to occur in nature and presents a qualitatively

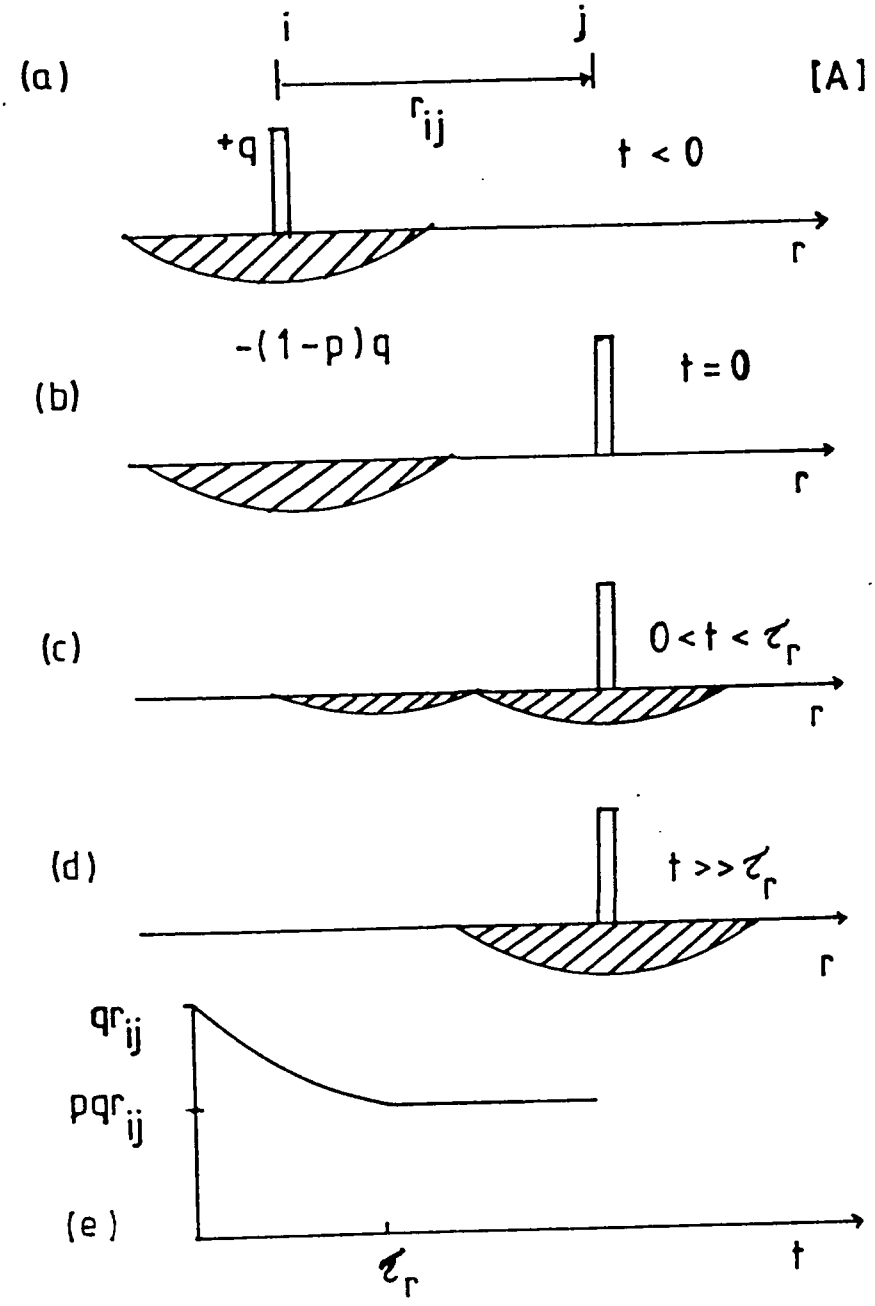

Fig. 2.7 [A] The discontinous jump of a charge q from a localised site i to a site j followed by a slower transfer of the screening charge. Diagrams (a)—(e) show consecutive stages, (e) shows the time dependence of the polarization P resulting from the transition from i to j.

different picture, although the end result is the same. Since the screening space charge cannot follow the individual transitions, the screening charge adjusts itself to the time-averaged occupancies f_i and f_j of the two sites. The application of an external field $\vec{E}$ enhances the downfield rate and reduces the upfield rate resulting in a net charge of occupancies by $\pm f'$ with respect to equilibrium. Each individual net transition may be considered as the transfer of a 'bare' unscreened charge q through the distance $|\vec{r}_{ij}|$, but the subsequent readjustment of the screening charge gives rise to a final polarization $|\vec{P}| = pq|\vec{r}_{ij}|f'$. Since all the net transitions take place in the field $\vec{E}$, the energy derived from the field is $|\vec{E}|qf'|\vec{r}_{ij}|$ but the energy stored in the system after relaxation is only

$$w_s = |\vec{E}|qp|\vec{r}_{ij}|f' \qquad (2.20)$$

and the energy lost is given by

$$w_l = |\vec{E}|q\ (1-p)|\vec{r}_{ij}|f' \qquad (2.21)$$

In either case, $\tau_r < \tau_D$ or, $\tau_D < \tau_r$, the setting up of a given state of polarisation $\vec{P}$ in the system of hopping charges must give rise to a loss of energy which is proportional to the stored energy and which does not depend on the rate at which this state of polarization has been established.

The energy loss w_l arising from the proposed screening mechanism is additional to any loss that may arise in an alternating field from the normal Debye relaxation τ_D. The screening loss extends down to much lower frequencies than the frequency $1/\tau_D$, where τ_D is a thermally activated Debye relaxation time.

An ideal dipolar system cannot give rise to screening since no

transfer of charge can occur. All real molecular dipoles have finite length on an atomic scale and invariably one of their poles is more rigidly fixed in the lattice than the other, as for example, in the case of a polar side group on a rigid carbon chain in a polymer. Jonscher has introduced the concept of a "pinned dipole", the response of which is not purely orientational but contains also an inseparable element of charge translation (Fig 2.7B). The 'pinned dipoles' screen field as hopping charges do, possibly in a less effective way.

By applying Hilbert transforms and the Kramers Kronig relations, Jonscher deduced the following equations for the real and imaginary components of the dielectric susceptibility and a.c. conductivity [2.8]

$$\chi'(\omega) \alpha \omega^{n-1}, \qquad n < 1 \tag{2.22}$$

$$\chi''(\omega) \alpha \omega^{n-1}, \qquad n < 1 \tag{2.23}$$

$$\sigma_{a.c.}(\omega) \alpha \omega^{n}, \qquad n \leq 1 \tag{2.24}$$

where $\chi'(\omega)$ is the real component of dielectric susceptibility,

$\chi''(\omega)$ is the imaginary component of dielectric susceptibility,

$\sigma_{a.c}(\omega)$ is the a.c. conductivity,

and the exponent 'n' usually lies between o.8 and 1.0. Again the a.c. conductivity is expressed by the following equation

$$\sigma(\omega)_{a.c.} = \sigma_o + \epsilon_o \omega \chi''(\omega) \tag{2.25}$$

where σ_o is the d.c. conductivity and $\epsilon_o \omega \chi''(\omega)$is the dielectric conductivity.

The important feature of Jonscher's model is in the extended range of frequencies over which the ratio of the imaginary and real components of the dielectric susceptibility remains constant and independent of frequency [2.6-2.8]

[B]

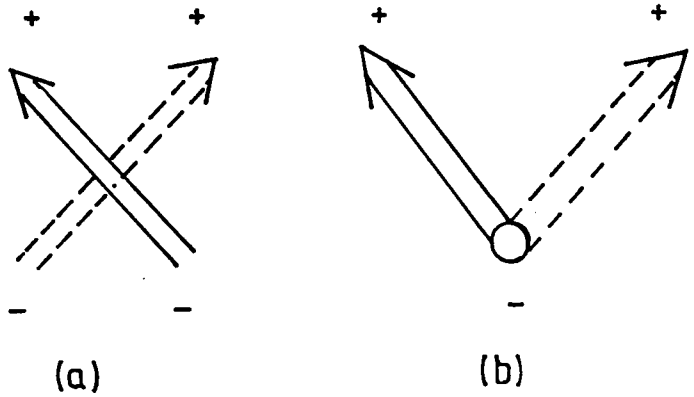

Fig. 2.7 [B] The contrast between a "free" dipole (a) and a "pinned" dipole (b).
A change of the orientation of the former does not bring about any change of the distribution of space charge, while a similar change for the latter does.

$$\frac{\chi''(\omega)}{\chi'(\omega)} = \coth\left(\frac{n\pi}{2}\right) = \text{constant} \qquad (2.26)$$

These predictions vary considerably from those to be expected on the basis of the Debye model.

2.5 Temperature Dependence of Permittivity

The Bosman and Havinga's Equations

In solid dielectric materials the nature of the dependence of dielectric constant on temperature may be determined by various factors. In most cases when the temperature increases, the ionic mechanism of polarization increases and hence the magnitude of ϵ' will be increased. In contrast, the increase of temperature does not affect the electronic polarization. On the otherhand the dipole orientation contribution is also directly proportional to the temperature, i.e. the temperature facilitates the rotation of dipoles in an applied electric field. In polar dielectric materials the molecules cannot orient themselves in the low temperature region. In the case of isotropic and cubic dielectrics, the temperature variation of the dielectric constant behaviour depends on three factors. These factors have been studied by Havinga [2.10]. He has attemped to calculate these factors from the Clausius-Mosotti equation, which is given by

$$\frac{\epsilon'-1}{\epsilon'+2} = \frac{N\alpha}{3\epsilon_o} \qquad (2.27)$$

where N is the number of molecules per unit volume,

ϵ_o is the permittivity of free space

α is the polarizability of molecules

ϵ' is the dielectric constant.

The Clausius-Mosotti equation is a relation between a macroscopic property of a dielectric, (i.e. ϵ', which can be measured

experimentally) and a microscopic property, (i.e. polarizability, α). In equation (2.27) N can be replaced by

$$N = \frac{N_A \rho}{M} \tag{2.28}$$

where N_A is the Avogadro's number (6.022169×10^{23} moles/litre)

M is the molecular weight (in kg)

ρ is the density (kg m^{-3}).

Another version of the Clausius-Mosotti equation may be written as [2.11].

$$\frac{\epsilon'-1}{\epsilon'+2} = \left(\frac{4\pi}{3}\right)\left(\frac{\alpha}{v}\right) \tag{2.29}$$

where v is equal to the volume of a small sphere of material. It must be taken that the volume of the sphere is large relative to the lattice dimensions.

The Clausius-Mosotti equation is applicable to all cubic and isotropic materials and the derivation is based on this assumption. From equation (2.18) one can derive the relation

$$\frac{1}{(\epsilon'-1)(\epsilon'+2)}\left(\frac{\partial \epsilon'}{\partial T}\right)_P = A + B + C \tag{2.30}$$

where A, B and C are the factors which have been calculated by Havinga. They are defined as:

A: This factor arises from volume expansion. As a result of expansion the number of polarizable particles per unit volume is reduced (since the numbers of particles are constant). Therefore by increasing temperature ϵ' decreases.

B: This factor increases the magnitude of ϵ' since it relates to the

increase of polarizability of the particles when the volume expansion occurs.

C: In a constant volume, this factor arises from the dependence of polarizability of the particles on temperature.

In order to determine A, B and C, some physical quantities must be measured experimentally [2.10,2.11]; usually these factors are evaluated from dielectric constant versus temperature data. The magnitudes of A, B and C vary for different materials.

Bosman and Havinga [2.12] have found that the sum of A and B is always positive and hence (A + B) contributes to increasing ϵ'. But the factor C is negative for those types of material with $\epsilon' > 10$ and it is positive for those which have $\epsilon' < 10$.

According to them, the temperature dependence of the dielectric constant (Equation 2.30) is always positive for $\epsilon' < 20$ and it is negative for $\epsilon' > 20$.

At high temperatures the relationship is not valid because other conduction processes (such as ionic conduction) begin to play a major role. In practice the relationship is useful for defining the temperature coefficient of permittivity over the range of environmental temperatures usually encountered, i.e. between about $0^{o}C$ to $200^{o}C$; it is however expected to hold for low temperatures at least down to 77 K.

2.6 Porosity Correction for Powder Samples

Dielectric measurements often have to be made on samples which are not solids in the sense of homogeneous single crystals where the actual density is very close to the true X-ray density. Two particular forms of material are of considerable industrial importance, namely powders and sintered polycrystalline materials. Powders, or powder mixtures, often form the precursors in the powder technology used to make many engineering ceramics. Examples relevant to the present thesis include sintered polycrystalline alumina and aluminium nitride, both of which

are required in sheet form for device applications. It is therefore necessary to devise techniques whereby the dielectric parameters of the matrix solid can be inferred from data obtained from measurements on powders or porous material.

A pressed powder sample is a mixture of air and small particles of the material of which has formed a rigid porous solid after being subjected to an external pressure. The porosity of the resulting solid is described by the term "packing fraction", which is defined as the ratio of the density of the porous sample to the true density of the solid material. The simplest way of representing this porous solid is by a two-layer model,(Fig 2.8a,b) neglecting any additional effects of grain boundaries (Fig 2.2d). On the otherhand, a sintered polycrystalline material (which will have been heat-treated often under pressure) contains fewer voids and consequently has a higher value of packing fraction (about 0.8 to 0.9) but may also be considered as a porous solid. However, the density of the sintered powder is less than the true X-ray density of the material (e.g., hot pressed Si_3N_4). There is a wide range of formulae available in the literature [2.13-2.17] for the correlation between data obtained from the powder and bulk forms of a given material. The expressions vary significantly depending on the particle geometry, particle size distribution and porosity. It is interesting to note that the dielectric correlation formulae available in the literature have been used for the determination of the complex permittivities of solids at frequencies above about 10^6 Hz [2.18].

The most widely used dielectric correlation formulae are those of Böttcher [2.14] are given by

$$\epsilon'_s = \frac{(2\epsilon'_p + 3\delta - 2)\{(3\delta - 1)(\epsilon'^2_p + \epsilon''^2_p) + \epsilon'_p\} - 2\epsilon''^2_p}{(3\delta - 1)^2(\epsilon'^2_p + \epsilon''^2_p) + 2\epsilon'_p(3\delta - 1) + 1} \qquad (2.31)$$

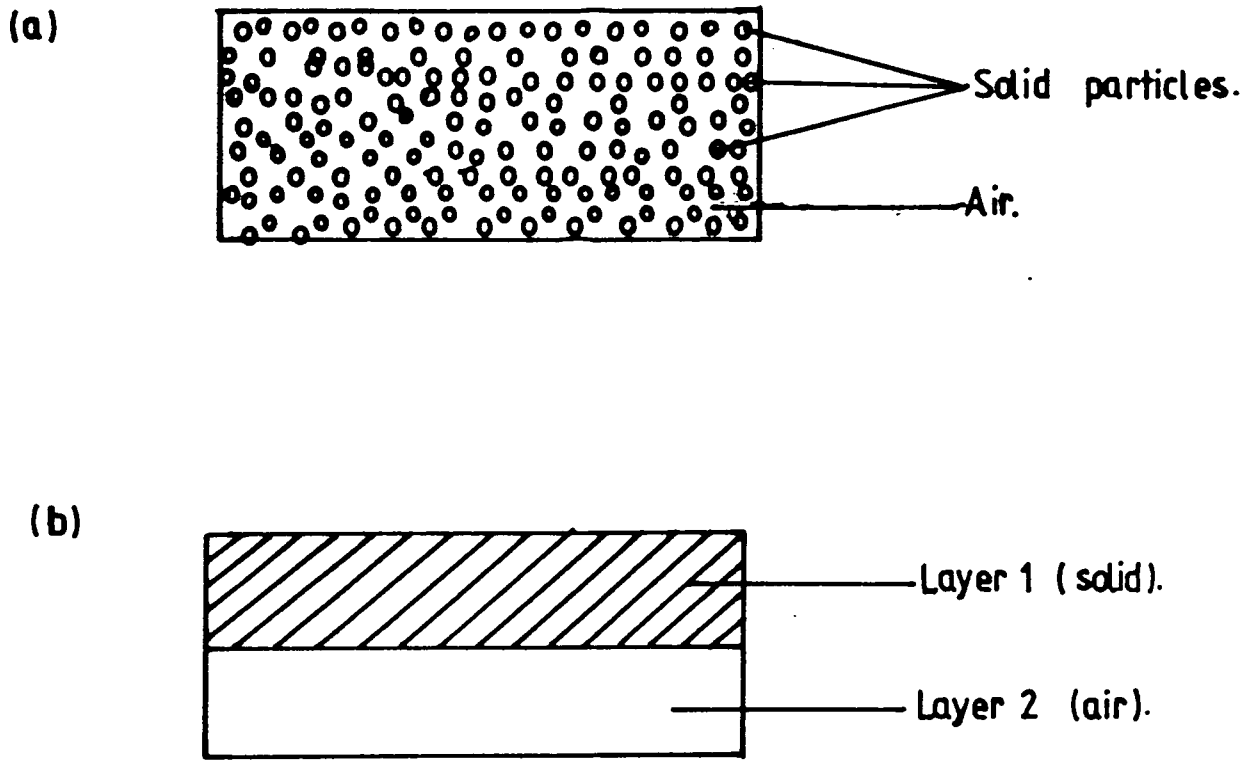

Fig. 2.8 (a) Schematic diagram of a powder sample.
(b) Equivalent two layer model.

and

$$\epsilon''_s = \frac{2(3\delta-1)\,(\epsilon''^{3}_p + \epsilon'^{2}_p\,\epsilon''_p) + \epsilon''_p(3\delta-2) + 4\epsilon'_p\epsilon''_p}{(3\delta-1)^2(\epsilon'^{2}_p + \epsilon''^{2}_p) + 2\epsilon'_p\,(3\delta-1) + 1} \qquad (2.32)$$

where ϵ'_s and ϵ'_p are dielectric constant of solid and powder respectively, ϵ''_s and ϵ''_p are the dielectric loss of solid and powder respectively, δ is the packing fraction.

These expressions apply specifically to spherical particles. On the otherhand a more recent equation is that derived independently by Landau and Lifshitz [2.19] and Looyenga [2.13]. The equation is

$$\epsilon'^{1/3}_p - 1 = \delta(\epsilon'^{1/3}_s - 1) \qquad (2.33)$$

where ϵ'_s is the bulk dielectric constant of the material and ϵ'_p is the dielectric constant of the powder at packing fraction δ. Looyenga has not given a separate formula for the dielectric loss but using the relation $\epsilon^* = \epsilon'-j\epsilon''$, Dube [2.20] obtained the following relation provided $\epsilon''/\epsilon' \ll 1$, (double dashed and single dashed are dielectric loss and dielectric constants respectively)

$$\epsilon''_s = \frac{\epsilon''_p}{\delta}\left(\frac{\epsilon'_s}{\epsilon'_p}\right)^{2/3} \qquad (2.34)$$

where ϵ''_s and ϵ''_p are the dielectric losses for solid and powder respectively. These are also suitable for spherical particles. In the present investigation, an attempt has been made to use the Looyenga's formulae for the dielectric correlation between powder and bulk in the

low frequency range both at room temperature and at 77 K. In all the powders examined here the assumption of spherical particles is a good first approximation, although there may be some distribution of particle size.

The Looyenga expression have been used in preference to Bottcher's because previous work on magnesium oxide [2.21] showed that these gave a better fit to the known values for the solid material.

CHAPTER TWO

REFERENCES

2.1 F.L.Weichman, Canadian J. of Physics, 51 (1973) 680.

2.2 K.V.Rao and A.Smakula, J.Appl.Physics, 36 (1965) 2031.

2.3 I.Broser and C.Reuber, J.Phys.Chem.Sol,27 (1966) 527.

2.4 P.Debye, Polar Molecules, The Chemical Catalog Company Inc., N.Y., 1929.

2.5 R.H.Cole, Physics of Dielectric Solids, 1980 (Conf. Series No.58), Institute of Physics, Bristol and London, p.1.

2.6 A.K.Jonscher, Nature, 253 (1975) 717.

2.7 A.K.Jonscher, Nature, 250 (1974) 191.

2.8 A.K.Jonscher, Nature, 267 (1977) 673.

2.9 M.Pollak and G.E.Pike, Phys.Rev.Lett., 28 (1972) 1449.

2.10 E.E.Havinga, J. of Phys.Chem.Solid, 18 (1961) 253.

2.11 R.A.Bartels and P.A.Smith, Physical Review, B, 7 (1973) 3885.

2.12 A.J.Bosman and E.E.Havinga, Physical Review, 129 (1963) 1593.

2.13 H.Looyenga, Physica, 31 (1965) 401.

2.14 C.J.F. Bottcher, Theory of Electric Polarization, (Amsterdam: Elsevier), 1952.

2.15 K.W.Wagner, Arch Elektrotech, 2 (1914) 378.

2.16 D.Polder and J.H.Van Santen, Physica, 12 (1946) 257.

2.17 D.A.G. Brugeman, Ann.Phys.Lpz, 24 (1935) 636.

2.18 L.K.H.Beck, Progress in Dielectrics, 7 (1967) 71.

2.19 L.D.Landau and E.M.Lifshitz, Electrodynamics of Continuous Media, Pergamon Press, London, 1960.

2.20 D.C.Dube, J.Phys.D: Appl.Phys., 3 (1970) 1648.

2.21 J.S.Thorp and N.E.Rad, J.Mat.Sci.,5 (1986) 157.

CHAPTER THREE

EXPERIMENTAL TECHNIQUES FOR THE MEASUREMENT OF DIELECTRIC PROPERTIES

3.1 D.C.Measurements

Although strictly not a dielectric property, it is convenient to begin the discussion by refering to d.c. conductivity, whose values often form a useful basis of comparison. There are several techniques for measuring the d.c. conductivity of solids which depend upon the nature, geometry and the surroundings of the material concerned. Usually two, three and four probe techniques are extensively used for the determination of the d.c. conductivity of solids (Fig 3.1a,b,c). Generally a metal contact may be either ohmic or rectifying depending on the relative work functions of the metal and the sample. However, for measurements of d.c. conductivity an ohmic contact is essential. A typical metal-dielectric-metal contact and its energy band diagram is shown in Fig 3.2 while Table 3.1 presents some typical values of work functions of metals and dielectrics.

Usually, gold (Au), silver (Ag) and some alloys like Ag-Ga, Bi-Sb, Ag-Sb, are used as contact materials since they provide ohmic contacts. Depending on the problem two, three or four probe techniques can be used for the determination of the d.c. conductivity of solid materials. For those with very high resistivity or very low conductivity (of the order of $10^{-14} \sim 10^{-18}\ \Omega^{-1}cm^{-1}$), as in the case of most of the insulators, two probe technique is generally employed. The limitation of the two probe technique is that the bulk resistance (or the resistivity) of the material under investigation should be considerably higher than that of the contact, so leaving practically no effect of contact resistance on the flow of current. In semiconductors, because

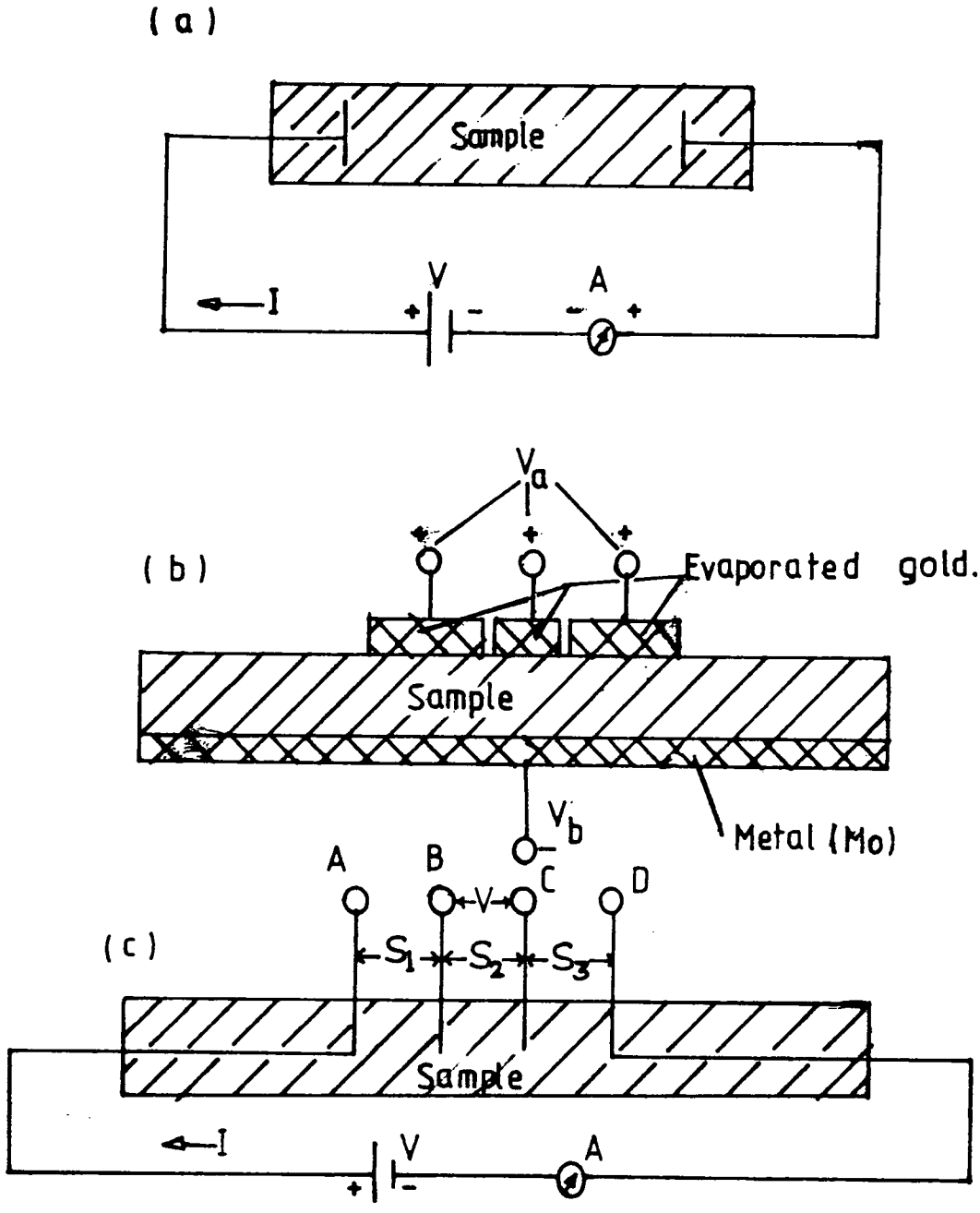

Fig. 3.1 (a) Two probe technique.

(b) Three probe technique.

(c) Four probe technique.

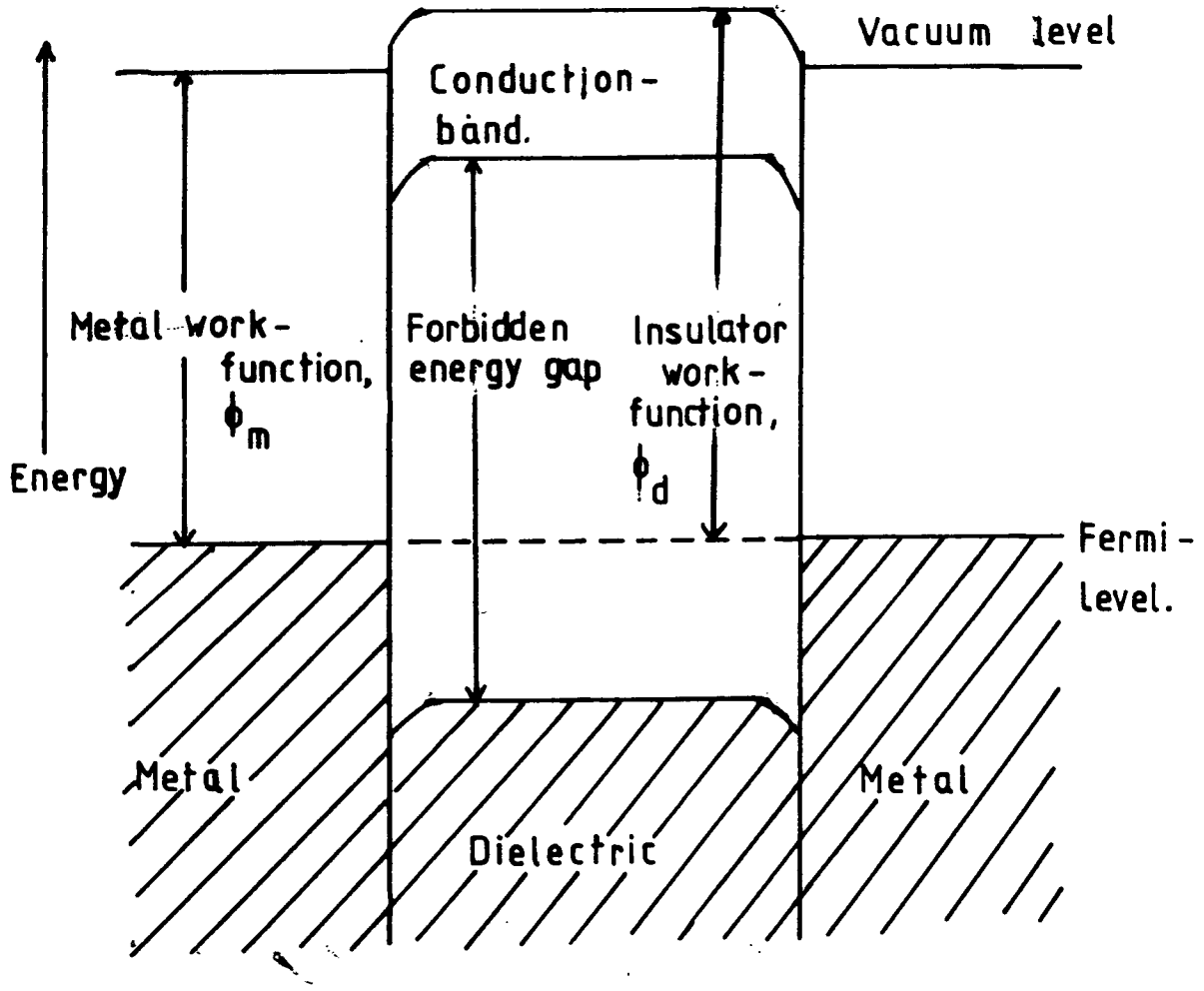

Fig. 3,2 A typical energy band diagram of a metal-insulator-metal contact.

TABLE 3.1: Typical values of work functions of metals and dielectrics at 20°C

Metal	ϕ_m, eV	Dielectric	ϕ_d, eV
Cs	1.9	Pure alumina (Al_2O_3)	~ 5
Mg	3.8	Pure silica (SiO_2)	~ 6
Al	4.2	Polystyrene	4.2
Ag	4.3	Polycarbonate	4.3
Ni	4.7	Boron alumino silicate glass	4.3
Au	4.9	Polyimide	4.4

of the significant contribution of the contact resistance towards the total resistance of the system, the two probe technique for determining d.c. conductivity is inaccurate and hence a four probe technique is usually used. In the four probe technique, the effect of the contact resistance is successfully avoided due to the merit of the technique itself and a precise measuremnet of the d.c. conductivity is possible, if the geometry of the sample is suitable for the system [3.1].

A three electrode technique becomes inevitable when the material under investigation is on a conducting substrate. On the free surface of the test sample a contact of relatively small area with respect to the conducting substrate leads to the current or field spreading effect [3.2-3.4], (Fig 3.3a), producing misleading results because the electrode area is not well defined. To avoid this effect, a third electrode of the form of a ring (a guard ring electrode) is deposited around the central circular electrode (Fig 3.3b,c). Both electrodes are concentric and spaced from each other by a suitably small physical distance. A single mask of proper dimensions is a realistic approach towards solving this problem at the evaporation stage. Because of the fact that both the guard ring and the central electrode are at the same potential the electric field to a very close approximation perpendicular to the electrode and the electrode area, corresponding to the central electrode diameter, is well defined. The d.c. conductivity ($\sigma_{d.c.}$) for the two and three electrode techniques can be expressed by the following equation

$$\sigma_{d.c.} = \frac{1}{\rho_{d.c.}} = \frac{\ell}{R.A} = \frac{\ell I}{VA} \quad (\Omega^{-1}\ cm^{-1}) \qquad (3.1)$$

where ℓ is the length of the sample (in cm) between the electrodes or the thickness, d (in cm) for the present investigation,

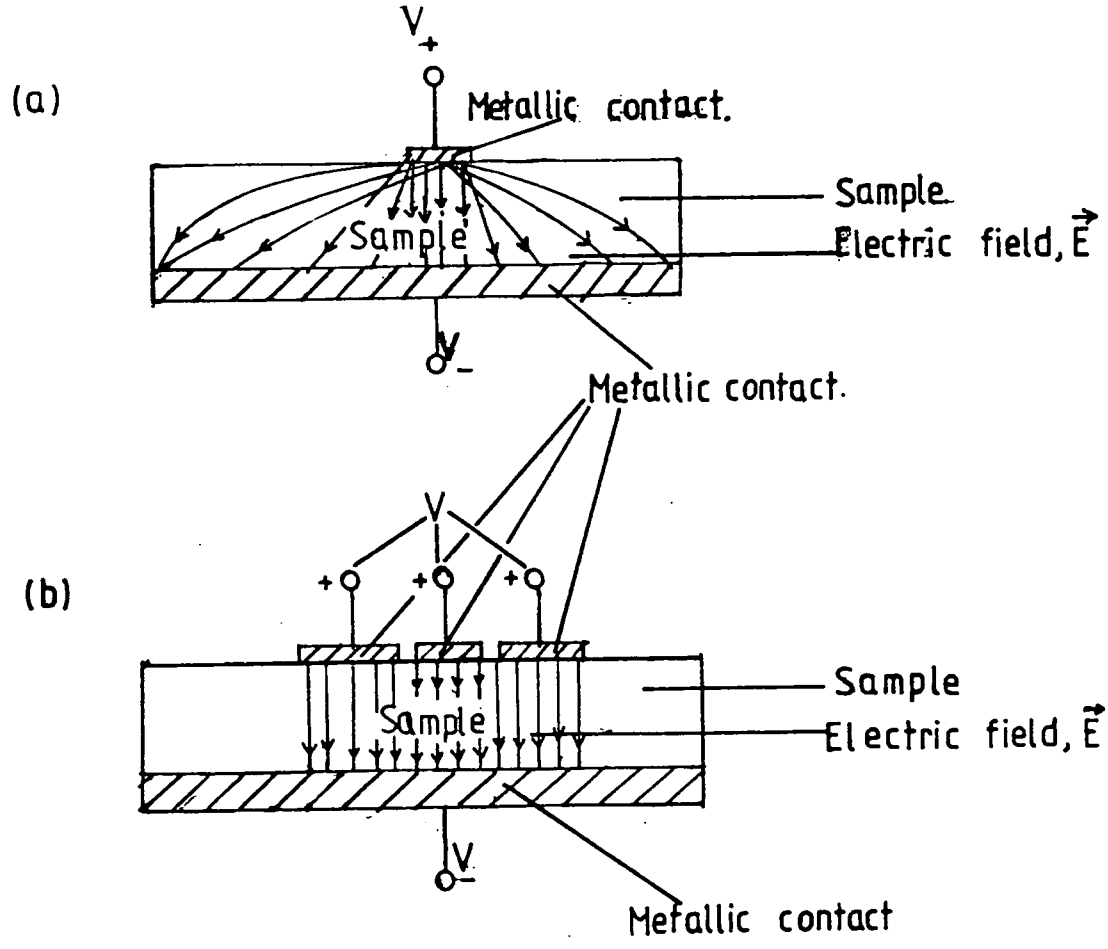

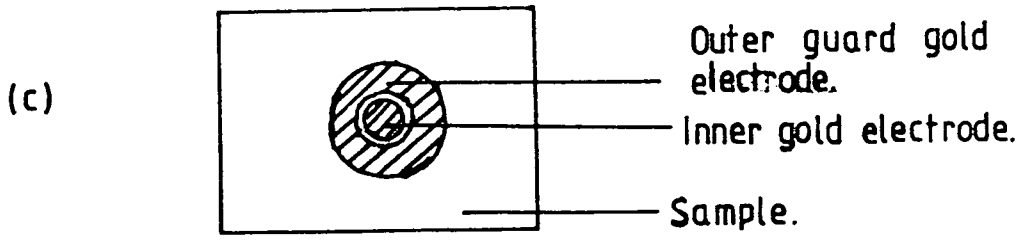

Fig. 3,3 (a) Field spreading effect.

(b) Parallel field distribution.

(c) Top view of the three probe system.

A is the area of the contact electrode (in cm^2),

R is the resistance between the electrodes of the sample (in ohms),

V is the voltage applied beteween the electrodes (in volts),

I is the current through the sample (in amperes),

$\rho_{d.c.}$ is the d.c. resistivity of the sample.

For the four probe technique the d.c. conductivity equation is as follows [3.5],

$$\rho_{d.c.} = \frac{1}{\sigma_{d.c.}} = 2\pi s \frac{V_{23}}{I} \qquad (3.2)$$

where $\sigma_{d.c}$ = d.c. conductivity (Ω^{-1} cm^{-1}),

$s_1 = s_2 = s_3 = s$ is the distance between the pair of points (in cm),

V_{23} is the voltage measured between the second and third electrodes (in volts),

I is the current between the first and the fourth electrodes (in amperes).

The alternative Van der Pauw method is well known for d.c.conductivity or resistivity measurement being especially useful when the sample geometry is irregular with arbitrary shape and size (Fig 3.4). This method provides information about d.c. conductivity and, for semiconducting material parameters such as the mobility, carrier concentration and Hall coefficient when the sample is subjected to a magnetic field. Here conductivity is given by the expression, [3.6],

$$\rho_{d.c.} = \frac{1}{\sigma_{d.c.}} = \frac{\pi d}{\log_e 2} \left[\frac{R_{AB,\,CD} + R_{BC,\,DA}}{2} \right] f\left(\frac{R_{AB,\,CD}}{R_{BC,\,DA}} \right) \qquad (3.3)$$

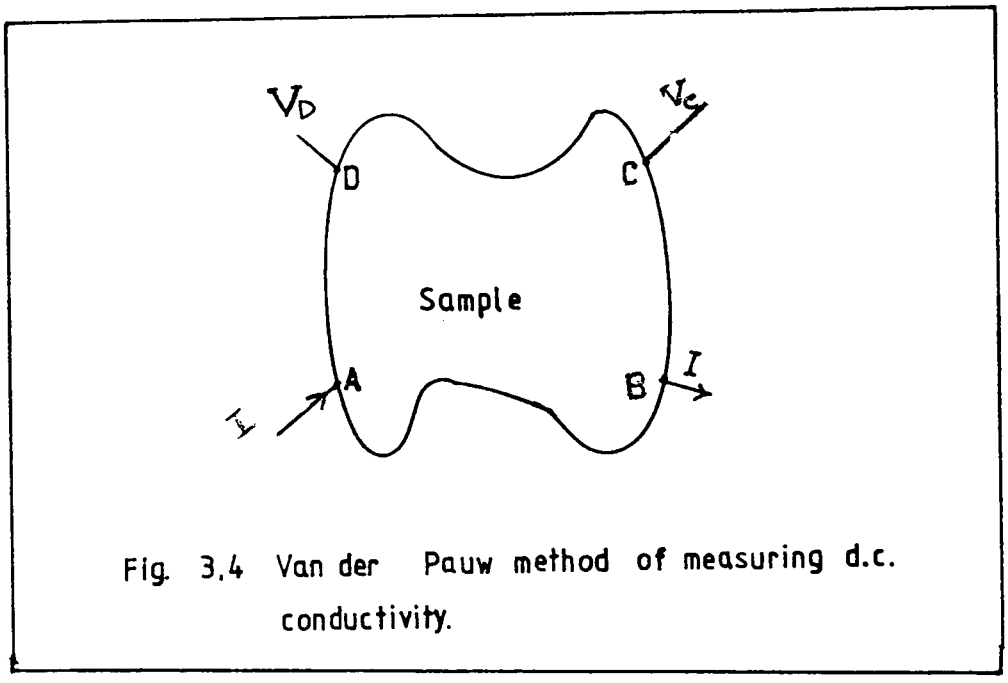

Fig. 3.4 Van der Pauw method of measuring d.c. conductivity.

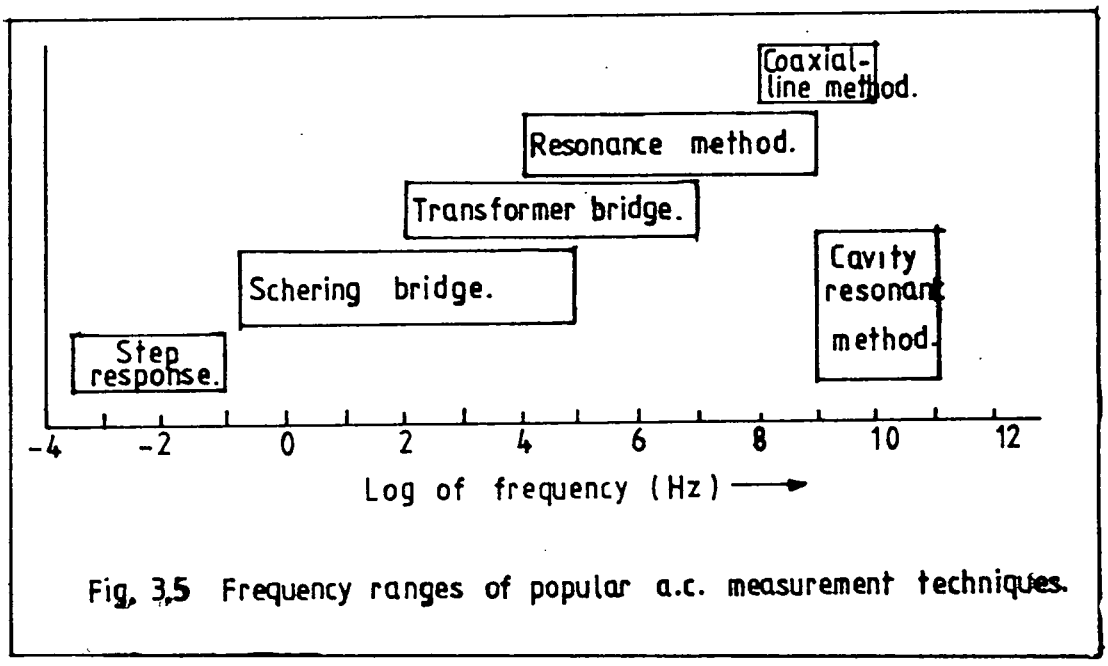

Fig. 3.5 Frequency ranges of popular a.c. measurement techniques.

where $R_{AB,CD}$ is the resistance between A and B when the current is flowing in between the points C and D.

$R_{BC,DA}$ follows the same analogy.

$\rho_{d.c.}$ is the d.c. resistivity of the sample.

$\sigma_{d.c.}$ is the d.c. conductivity of the same.

d is the thickness of the sample.

f $\left(\frac{R_{AB,CD}}{R_{BC,DA}}\right)$ is a correction for electrode assymetry.

3.2 Low Frequency Bridge Techniques

3.2.1 Two Electrode Systems

In order to determine the dielectric properties of solid materials over a wide range of frequencies, it is necessary to use different techniques for the different frequency ranges. Each technique has its performance limited to within a fixed range of frequencies. The frequency ranges of the most popular circuitry are summarised in Fig (3.5) and their main advantages and disadvantages listed in Table (3.2).

At low frequencies ($5x10^2$ Hz - $3x10^4$Hz) bridge techniques are most appropriate and suitable for the precise measurements of complex permittivities and conductivity. In this range of frequencies, the dielectric properties of materials are usually determined by measuring the capacitance and the conductance of the sample held between a pair of micrometer electrodes. The principle of the Wheatstone bridge has long been employed in the measurements of conductance, inductance and capacitance [3.7]. The design of these bridges depends not only on the type and precision of measurement required, but also on the frequency range needed. The electrode systems are made so that the effect due to fringing field at the edge of the specimen are reduced and the entire system is contained in a metal shielding box to eliminate undesirable effects of stray field. Electrodes must be evaporated on the opposite polished surfaces of the specimens to ensure a good electrical contact

TABLE 3.2 Salient Features of a.c. Measuring Circuits

Type	Advantages	Disadvantages
Step response	Simple apparatus; measure low loss.	Not direct reading; ϵ' very inaccurate; time consuming.
Schering bridge	Can be used from low to very high voltages and currents; direct reading.	Strays can give errors; does not usually measure as low loss as transformer bridge.
Transformer (ratio arm) bridge	Strays are generally absent, three terminal measurements are simple; leads can be compensated for; direct reading, very low loss measurable.	Does not measure to highest accuracy over a very wide frequency range.
Resonant circuit	Does measure low loss	Not direct reading; temperature variation is difficult.
Coaxial line	Simple measurement, low loss measurement is possible.	Slight instability in VSWR and position of minima could cause error. Temperature variation is difficult.
Cavity	Does measure low loss	Not direct reading, temperature variation is difficult.

over a well defined area between the specimen and the electrodes of the dielectric test jig; with many materials gold is used for this purpose [3.8]. The usual arrangement for solids, comprises flat, parallel metal plates of known area and separation between which is inserted the sample, in the form of a parallel sided disc of diameter slightly less than that of the electrodes. If the diameter of the sample extends beyond the electrodes then correction for edge effects are necessary.

The permittivity (ϵ'), loss tangent ($\tan\delta$) and a.c.conductivity ($\sigma_{a.c.}$) are expressed by the following equations, [3.9, 3.10].

$$\epsilon' = \frac{C}{C_o} \tag{3.4}$$

$$\tan\delta = \frac{G}{\omega . C} = \frac{\epsilon''}{\epsilon'} \tag{3.5}$$

$$\sigma(\omega) = \frac{d}{A}.G = \omega\, \epsilon_o .\, \epsilon'' \tag{3.6}$$

$$C_o = \epsilon_o \frac{A}{d} \tag{3.7}$$

where C is the nett capacitance of the sample placed between the electrodes (in farad).

c_o is the capacitance of the air with the same gap as the sample between the electrodes (in farad).

$\omega = 2\pi f$ is the angular or radian frequency (in rad/sec).

A is the area of the contact electrode (in metre^2).

d is the thickness of the specimen (in metres).

ϵ_o is the 8.854×10^{-12} (farad/metre), the absolute value of permittivity of free space.

ϵ'' is the imaginary component of the dielectric susceptibility.

G is the conductance of the sample (mho)

In order to allow for the stray capacitance (c_s), if any, present in

in the system, it is necessary to make some simple computation. Although at low frequencies the inductive effect is negligible, care must be taken to make the system non-inductive as best as possible to obtain precise values of capacitance and capacitive conductance. With increase of frequency, the contact electrodes may introduce a significant amount of inductance by introducing a component of inductive conductance, which could be an important source of error in the measurement of conductance (capacitive); although the capacitance part remains almost unaffected.

The total capacitance c_t, with the sample placed in between the electrodes is given by

$$c_t = c + c_s \tag{3.8}$$

where c is the the actual capacitance of the sample

c_s is the stray capacitance present into the system.

The air capacitance c_a, with the same spacing between the electrodes is given by

$$c_a = c_o + c_s \tag{3.9}$$

where c_o and c_s have their usual meanings. From the equations (3.8) and (3.9), the actual capacitance c, of the sample is obtained as

$$c = c_t - c_a + c_o \tag{3.10}$$

In order to avoid surface conductivity the following boundary conditions must be maintained.

$$d \ll D , L$$

where d is the thickness of the sample (in metres)

D is the diameter of the contact electrode (in metres)

L is the distance between the corner and the periphery of the electrodes (in metres).

Corrections for the edge effect have been discussed by Scott, H.H. et al [3.11]. The formula for the edge capacitance with circular electrodes is

$$c_e = \frac{1.113\ D}{8\pi}\left(\ell n\ \frac{8\pi D}{d} - 3\right) \qquad (3.11)$$

where d and D are respectively the thickness of the sample and diameter of the contact. The equivalent circuit of the dielectric is shown in Fig 3.6. The modified form of the dielectric permittivities become

$$\epsilon' = \frac{c}{c_o + c_e} = \frac{c_t - c_a + c_o}{c_o + c_e} \qquad (3.12)$$

$$\tan\delta = \frac{G}{\omega(c_t - c_a + c_o)} \qquad (3.13)$$

$$\epsilon'' = \epsilon'.\ \tan\delta = \frac{G}{\omega\ (c_o + c_e)} \qquad (3.14)$$

The limitation of this technique with increasing frequency is due to the growing importance of stray capacitance and inductance, which ultimately undermine the validity or upset the whole measurement.

3.2.2 Three Electrode Systems (with Guard Ring)

There are a very wide variety of techniques quoted in the literature for measuring the dielectric properties of materials. Three terminal techniques are ideal, particularly with disc electrodes guarded as shown in Fig (3.3b). This arrangement not only eliminates surface conduction but renders the electrical lines of force relatively parallel between the measuring electrodes. It can be shown that edge

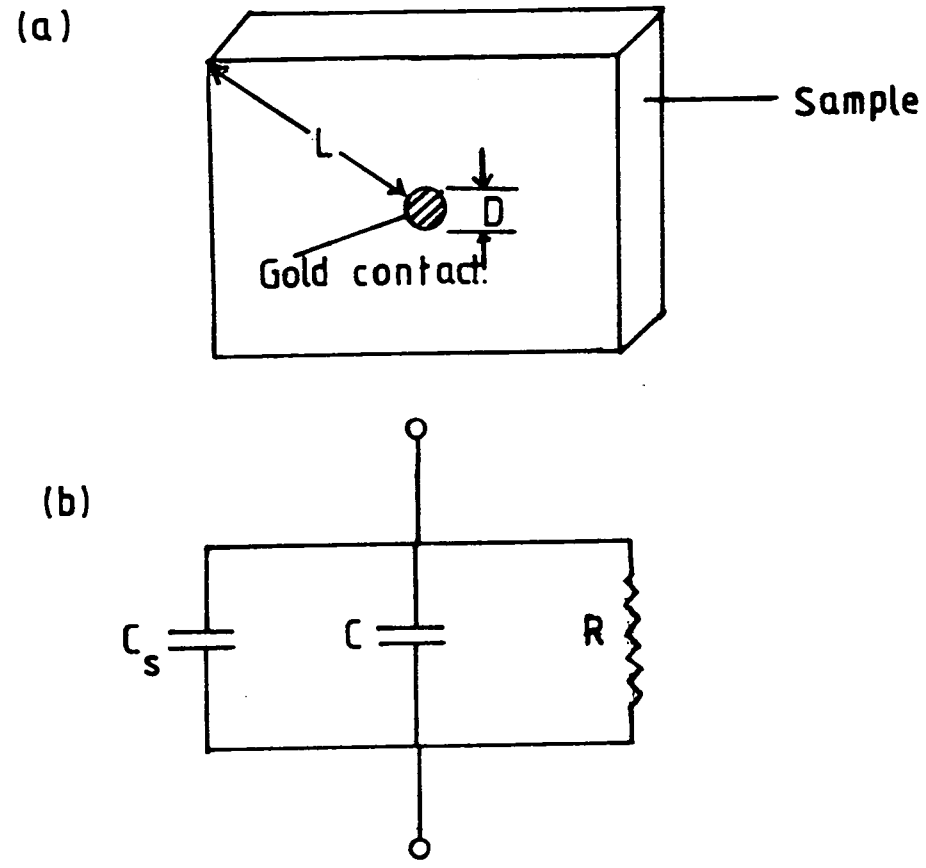

Fig. 3.6 (a) Dielectric sample with evaporated gold contact.

(b) Equivalent circuit of a dielectric sample.

effects have a negligible effect on the capacitance if the guard-centre disc electrode separation is small compared with the sample thickness [3.12]. In a recent publication, D.Evans and J.S.Thorp [3.13] have reported a design of a three electrode dielectric sample holder based on a BNC connector. In their observation they found the similar effect as described above. In the present investigation, thick film of glass on molybdenum metal was characterised by this technique.

3.2.3 Coaxial Holders and Measurements on Powders

It is generally a common practice to use single crystal or a sintered polycrystalline sample for the assessment of the dielectric prperties of solids. It can involve technical difficulties in sample preparation both from the availability and fragility of some materials. One of the main reasons for using powder samples for the determination of the complex permittivities of solids is to overcome these problems. There is a great deal of work has been done by many researchers in this regard. To investigate the dielectric properties of powder samples, it is necessary to design a suitable sample holder to hold the sample properly in position. The powder needs to be compacted to different packing fractions to form porous solids. It is found that a coaxial holder with proper dimensions is suitable for holding, compacting and taking measurements on dielectric powder samples even at low temperature. The use of two metallic guard cylinders eliminates fringing field capacitance.

After compression of the powder sample, a porosity correction is usually made by appropriate formulae to obtain the solid value of the dielectric permittivities. In the low frequency region interfacial polarization on the space charge effect plays an important role and it depends or the purity and perfection of the sample. Again, in this frequency region, if the perfection of the sample deviates from its single crystal to polycrystalline and then to amorphous state, the

space charge polarization contributes noticeably. So, it is self-evident that, in order to determine the dielectric properties of solids by measuring powders, it is essential to allow for or overcome this space-charge-effect.

A study of the previous literature of the low temperature dielectric work shows that at low temperatures (up to 77K) there is no appreciable change in the real component of the dielectric susceptibility. The present investigation confirms that the interfacial or space-charge polarization is extremely sensitive to temperature and reduces exponentially with lowering temperature.

The formula for the capacitance of a coaxial holder with any kind of dielectric in place is given by the following equation, [3.14]

$$c = \frac{2\pi \epsilon_o \epsilon'}{\ell n\left(\frac{b}{a}\right)} \qquad (3.15)$$

where ℓ is the length of the coaxial holder

b is the inner radius of the outer cylinder

a is the radius of the inner cylinder

ϵ' is the real parts of the complex permittivities

ϵ_o is the 8.854×10^{-12} (farad/meter), permittivity of free space.

One limitation of this method of characterizing powders at low temperature in order to obtain the bulk properties is that the dielectric loss at room temperature cannot easily be found because of the unknown contribution from space charge polarization.

3.3 High Temperature Low Frequency Measurement Techniques

The apparatus used for the high temperature low frequency measurement is shown in Fig (3.7). It is a cylindrical furnace with high heat capacity, equipped with an on-off type thyristor controlled

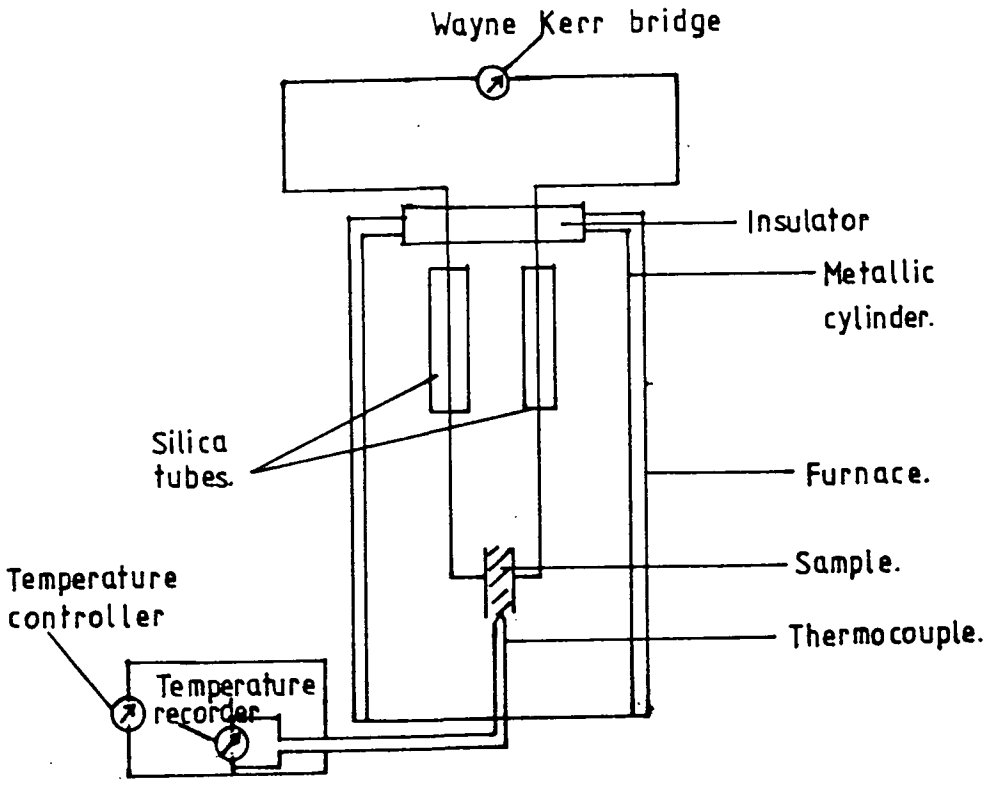

Fig. 3.7 Schematic diagram of high temperature furnace with experimental set up.

temperature unit allowing a precise measurement of the temperature within ± 2°C. The high heat-capacity of the furnace helps in not raising the temperature abruptly; on the otherhand, an optimum driving current for the furnace enables the thyristor to control the temperature efficiently and provides a constant temperature for the reasonable working-time. A Pt/Pt 13% Rh thermocouple was provided with the unit as the temperature sensor and placed along the axis and midway along the furnace tube.

For a good electrical and mechanical contact platinum paste was used on both surfaces of the samples and then two platinum wires attached individually to the respective paste contacts. This contact making task was tedious and undertaken in two steps. Initially, an ordinary hot air blower was used to dry up the paste to make the bonds between the sample-platinum paste and the wire-paste sufficiently strong to hold it adequately. In the second step, the sample with the connecting platinum wires was hung down the furnace tube, previously heated at 350° C for hours, to get a good mechanical and electrical contact between the electrodes and the specimen. The platinum wires were running through the holes of the two silica tubes to ensure the electrical isolation between the wires. It may be stressed here that platinum paste rather than silver paste was used. Silver has been avoided as contact material because of its high diffusion rate at high temperature; Harrop [3.15] has pointed out regarding silver as its notorious and adverse effects if there is any flaw present in the system. On the contrary, K.V.Rao and A. Smakula [3.16] used silver paste for contact electrodes for high temperature measurements without mentioning any inconvenience in using it. There are, to the author's knowledge, no adverse reports on the use of platinum with oxide materials.

A digital meter, previously calibrated against a Pt/Pt 13% Rh

thermocouple, monitored the temperature of the sample precisely. The specimen was surrounded by a stainless steel tube which was located inside and along the furnace. This tube was properly grounded and used as a shield to protect the samples from all unwanted signals due to thermal noise or electrical and other sources external to the specimen. In the present investigation most of the samples were oxides and hence there was no risk of chemical change in carrying out the experiment in the ambient air atmosphere. However, to avoid any oxidation effect with the nitride samples, the temperature in this case was restricted to 350°C.

The procedures of the d.c. and a.c. measurements were exactly the same as in room temperature case. The residual capacitance and the conductance were recorded and deducted from the apparent capacitance and conductance respectively, in order to get the effective values. Although a suitable mask was designed to ensure a precise area of the contact, still there was an error present due to the spreading of a minor amount of platinum paste beyond the specified mask area and hence a back calculation was carried out to rectify this error. The procedure adopted for the correction is as follows:

$$\epsilon'_{r.t} = \frac{c_s - c_{res}}{c_o + c_e} = \frac{c_{nett}}{c_o + c_e} \qquad (3.16)$$

where $\epsilon'_{r.t.}$ is the permittivity at room temperature.

c_s is the sample capacitance with platinum paste (in farads)

c_{res} is the residual capacitance of the assembly without the sample (in farads)

c_o is the capacitance of the equivalent air capacitance (in farads).

c_e is the fringing field capacitance (in farad) at room temperature.

c_{nett} is the nett capacitance of the sample with platinum paste (in farads).

and

$$\tan\delta_{r.t} = \frac{G_s - G_r}{\omega . c_{nett}} = \frac{G_{nett}}{\omega . c_{nett}} \qquad (3.17)$$

$$\epsilon'' = \epsilon' . \tan\delta \qquad (3.18)$$

where $\tan\delta_{r.t.}$ is the loss-tangent at room temperature.

G_s is the conductance of the sample with platinum paste (in mho)

G_r is the residual conductance of the assembly without sample (in mho)

ω is the radian frequency (in radian/sec.)

3.4 Low Temperature Low Frequency Measurement Technique

The apparatus used for the low temperature low frequency measurement is shown in Fig (3.8). The stainless steel cryostat used for this purpose had three chambers: (a) the outermost chamber, (b) the mid-chamber and (c) the innermost chamber. The outermost chamber (a) was always being kept under vacuum to prevent any external flow of heat into the system or vice-versa; it ensured very little loss of liquid nitrogen from the system. The order of vacuum usually needed for this kind of experiment is about 10^{-4} torr and a vacuum unit provided with water-cooled oil diffusion pump backed by a rotary pump is capable of fulfilling this condition. The mid chamber (b) was the reservoir of liquid nitrogen. In the inner chamber (c) the specimen suspended with two non-inductive conducting wires isolated from each other by two silica tubes. The technique for making non-inductive leads from

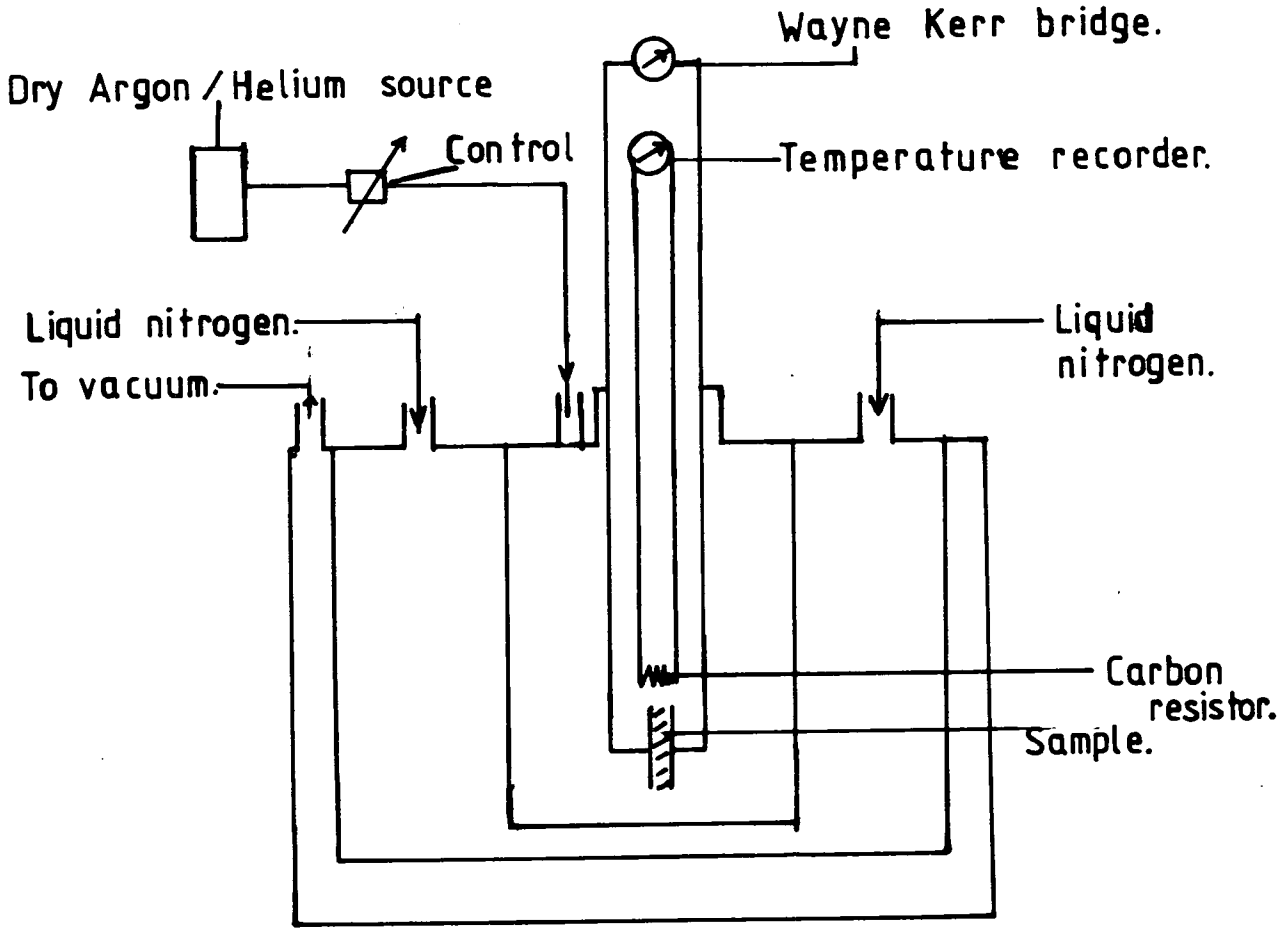

Fig. 3,8 Schematic diagram of a low temperature low frequency measurement equipment.

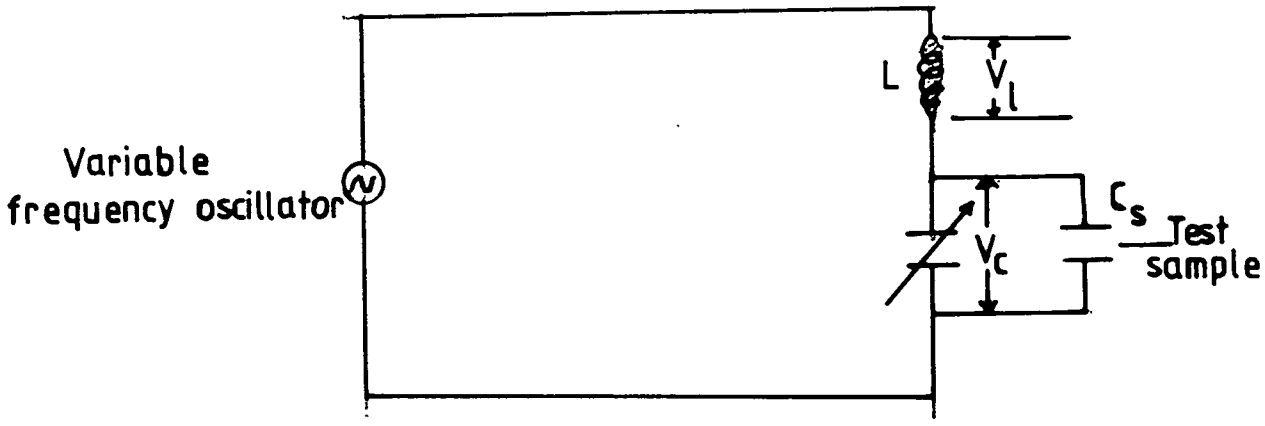

Fig. 3,9 The simplified circuit diagram of the Q-meter method of comlex permittivity measurement.

resistive wire had been exploited for this purpose. It is important to note that both in high and low temperature measurements, it is essential to minimize the effect of inductance, because of the fact that its increasing contribution with increased frequency slightly changes the apparent values of the capacitance and conductance of the specimen. A carbon resistor mounted near the sample but isolated from it and connected to a temperature recorder (THOR cryogenics model 7040) gave a direct temperature reading of the specimen.

The innermost chamber was initially evacuated and then filled with dry argon gas at 740mm of Hg. The pressure difference between the innermost chamber and the surrounding atmosphere held the top plate of the cryostat and the sample firmly in their proper positions. Argon gas was used to provide a thermal conductance between the innermost chamber and the liquid nitrogen chamber. The top plate, provided with four thin metallic electrodes isolated from each other, was designed to suit the experiment. The chamber was refilled with a small volume of liquid nitrogen in order to replace loss of the fluid at intervals of about half an hour. It was necessary to run the system for about fourteen hours to cool down the system to 85 K.

The specimen was suspended inside the inner metallic chamber and the cryostat was properly grounded to avoid any unwanted interference from electrical or other sources external to the specimen. Silver paste was applied for contact electrodes to which were joined on either side non-inductive copper leads. The measurements were taken by using the Wayne Kerr Bridge and the procedure followed for that for the room temperature and high temperature measurements. The procedure for the contact area calculation was the same as followed in the high temperature measurements.

3.5 The Q-Meter Method

In this method, which covers the frequency range from about

$3x10^4$Hz to $1x10^7$ Hz the principle of determining the dielectric permittivity of a material is based on the series resonant circuit (Fig 3.9) when a circuit containing resistance R, inductance L and capacitance C is subjected to an alterating voltage source of variable frequency, it resonates at a particular frequency f_r, is given by

$$f_r = \frac{1}{2\pi\sqrt{LC}} \tag{3.19}$$

The impedance of the circuit at resonance is

$Z = R$ and $j(\omega L - \frac{1}{\omega c}) = 0$; in otherwords, the reactance of the circuit becomes zero and the impedance becomes equal to the resistance present in the circuit. The magnification of the circuit, Q, is defined as

$Q = \frac{X}{R}$, whereas $X = j\omega L = \frac{1}{j\omega c}$ and represents the reactance of the capacitive or inductive elements present in the circuit.

In Fig (3.9) the Q of the circuit equals the ratio of the capacitance voltage V_x, to the source voltage V_s. Therefore,

$$Q = \frac{V_x}{V_s} \tag{3.20}$$

A voltmeter may be connected across either of the reactances and can be calibrated directly in terms of Q. This voltmeter is located on the Q-meter and the Q-value of the circuit is read directly from the meter. The total circuit capacitance C_t, with the sample inserted in between the electrodes of the jig and resonated by the variable capacitor of the Q-meter is given by

$$C_t = C_s + C_1 + C_h + C_L \tag{3.21}$$

where C_s, C_1, C_h, and C_L are the capacitances of the sample, Q-meter,

sample holder and the connecting cables respectively. Consequently, after removing the sample from the electrodes of the test jig and keeping the spacing as before, the resonant condition can be established by changing the variable capacitor of the Q-meter. The circuit capacitance is then given by

$$C_t = C_o + C_2 + C_h + C_L \tag{3.22}$$

where C_o and C_2 are the capacitance of the air capacitor and variable Q-meter capacitor respectively. Combining equations (3.21) and (3.22) yields

$$C_2 - C_1 = C_s - C_o \tag{3.23a}$$

If the edge effect can be neglected, the permittivity is given by

$$C_s = \epsilon' C_o \tag{3.23b}$$

where $C_o = \epsilon_o \cdot \frac{A}{d}$

$\epsilon_o = 8.854 \times 10^{-12}$ F/meter

A = area of the contact (meter^2)

d = thickness of the sample (meter)

Substitution gives for the permittivity

$$C_2 - C_1 = \epsilon' C_o - C_o = C_o (\epsilon' - 1) \tag{3.24}$$

or

$$\epsilon' = \frac{C_2 - C_1}{C_o} + 1 \tag{3.25}$$

Due to fringing effects an edge correction is required. The equation

(3.25) may be modified to

$$\epsilon' = \frac{C_1 - C_2}{C_o + C_e} + 1 \qquad (3.26)$$

where C_e is the edge capacitance. The same correction for loss-tangent is negligible.

The loss tangent ($\tan\delta$) is given by

$$\tan\delta = \frac{Q_2 - Q_1}{Q_1 - Q_2} \cdot \frac{C_2}{C_2 - C_1} = \frac{\epsilon''}{\epsilon'} \qquad (3.27)$$

where Q_2 is the quality factor of the circuit with sample in between the electrodes of the jig.

Q_1 is the quality factor of same circuit but with air between the electrodes with the same gap.

C_2 is the capacitance of the variable capacitor (in farads) with the sample in between the electrodes of the jig.

C_1 is the capacitance of the variable capacitor (in farads) with the air in between the electrodes of the same gap.

In the above C_1 and C_2 are indicated values and in fact the knowledge of the effective capacitances of C_1 and C_2 is required and it is given by [3.17]

$$C_E = C_{ind.} \frac{1}{1-\omega^2 L C_{ind}} \qquad (3.28)$$

where "E" indicates effective and "ind" indicated values respectively.

A further point may be noted regarding the operation of the Q-meter. As the frequency increases, the value of the inductance needed to resonate the circuit decreases, lowering the quality factor of the circuit. The accuracy of the measurement depends on having a high value of the Q-factor and in practice the need for low inductances

limits the upper frequency of operation of this technique.

3.6 Structural and Analytical Appraisal

3.6.1 Scanning Electron Microscopy (SEM):

A Cambridge Stereoscan S600 SEM was used to investigate the surface topographies of the samples of alumina, aluminium-nitride and glass-on-metal substrates. A schematic diagram of the SEM is shown in Fig (3.10). The SEM may be operated in several modes (e.g. secondary emission mode, energy dispersive analysis by X-ray (EDAX), electron beam induced current (EBIC) mode etc) by imaging the signals derived from different interactions which occur between the incident electron beam and the specimen [3.18]. The secondary emission and EDAX modes were used in the present investigation.

(a) Secondary Emission Mode:

The basic principle of operation in this mode is that as the electron beam is scanned across the sample, secondary electrons are emitted from the specimen surface. The secondary electron coefficient depends critically on the composition and orientation of the area illuminated by the primary electron beam. Consequently by imaging the variations in secondary emission high contrast can be obtained. The secondary electron beam on the sample is synchronised to the output signal from the cathode ray tube with the same raster generator to avoid any time-lag in the image formation. In this way a micrograph of the sample is produced on the screen. There is a problem, however, with the insulating sample; the surfaces of which become electrostatically charged by the electron beam. This induced field deflects the electron beam and so destroys the SEM image of the sample. In the present investigation, as the samples were highly insulating a conducting path was provided by evaporating a thin gold film on the surface of the sample to avoid the charge-build-up effect.

(b) Energy Dispersive Analysis of X-rays (EDAX):

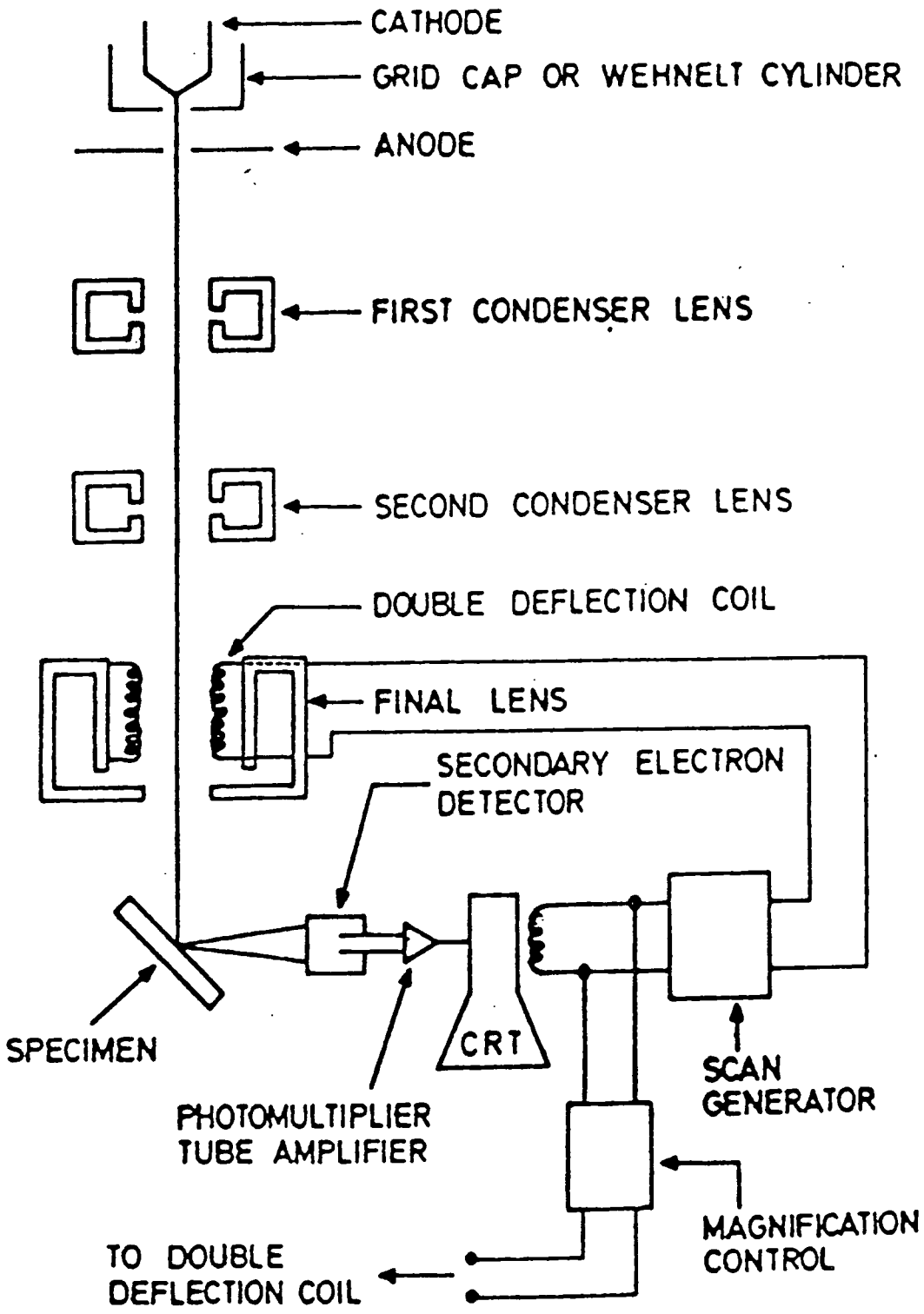

Fig. 3·10 Schematic diagram of the Scanning Electron Microscope

As the operating voltage of the SEM is 25 kV X-rays are produced by the interaction of the electron beam with the sample. Each element produces its own characteristic X-ray spectrum which may be analysed to identify the element. The X-rays emitted from the surface of the sample pass through a thin beryllium window into a pre-cooled reverse biased p-n junction Si(Li) detector. This leads to the ejection of photo-electrons which give up most of their energy in the formation of electron-hole pairs. The reverse bias on the p-n junction forces the electron hole pairs to form a charge pulse. This charge pulse is converted into a voltage pulse by a suitable charge sensitive pre-amplifier. The amplitude of the voltage pulse is proportional to the magnitude of the charge released by the photoelectron which in turn is proportional to the energy of the incident X-ray photons originating from the elements of the sample. Thus an energy spectrum of the X-rays can be built up and analysed in a multichannel analyser to identify the elements present in the sample. The resulting spectrum can be displayed on the screen or printed in a printer for the permanent record. Again, it was necessary to evaporate thin gold film on the surface of the sample (as was needed for the secondary emission mode) to eliminate charging effects. The main advantage of EDAX is that, since the diameter of the electron beam used in the SEM is only about 5 microns, analysis of small volumes becomes possible.

3.6.2 Reflection High Energy Electron Diffraction (RHEED)

The main objectives of using RHEED in the present investigation were twofold; firstly to identify the impurity phase and secondly to observe the degree of crystallinity.

When a parallel beam of electron waves impinges on a crystal at an angle θ in Fig (3.11a) to a set of crystallographic planes of interplanar spacing d and Miller indices (hkl) diffraction will result if the ray paths from successive planes in the system differ from each

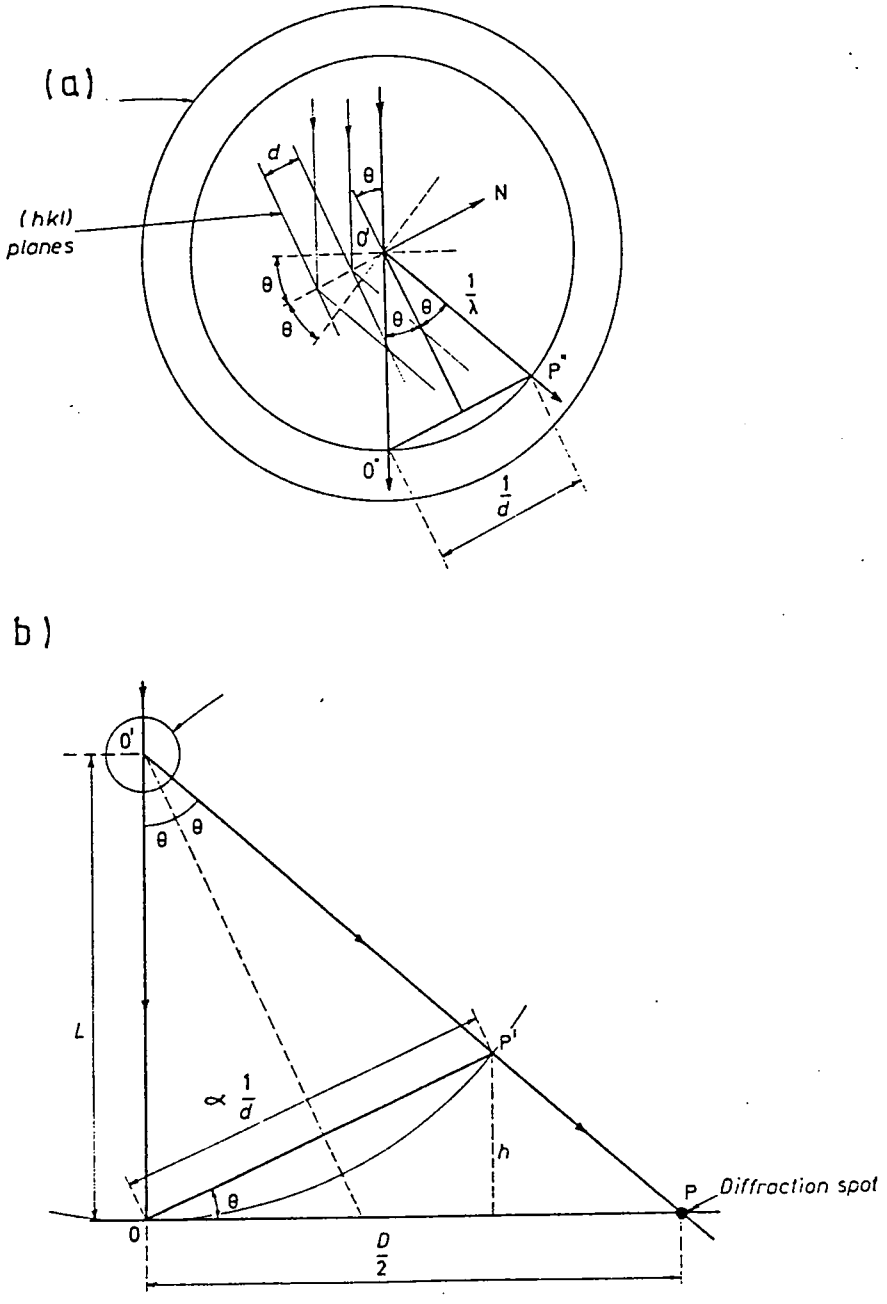

Fig. 3·11 Schematic diagram illustrating the RHEED technique.

other by an exact number of wavelangths. Hence the requirement for the diffraction can be expressed as follows

$$\lambda = 2\, d_{hkl} \sin\theta_{hkl} \qquad (3.29)$$

where λ is the wavelength of the electron wave (in Å)

d is the interplanar spacing (in Å)

θ is the Bragg angle between the incident beam and the atomic planes and (hkl) are the Miller indices of the planes concerned.

In RHEED, an electron beam with energy in the range of 10 to 100 keV is usually used which corresponds to wavelengths of 0.12 to 0.04 Å respectively. As the interplanar spacing is of the order of a few Angstrom units, the Bragg angle must have a value between 1.5° to 0.5° in order to get a diffraction pattern in the energy range mentioned. Thus, in this technique, only those crystal planes that are tilted at less than a few degrees to the surface of a specimen will diffract an electron beam at a glancing angle.

An alternative form of the eqn. (3.29) is

$$\frac{1}{d} = 2\,\frac{1}{\lambda}\,\sin\theta_{hkl} \qquad (3.30)$$

This reciprocal lattice representation is illustrated by Fig (3.11a), where $0'' P'' = \frac{1}{d}$ is the reciprocal lattice vector d^* and $1/\lambda$ is the radius of the reflection sphere. The construction of the 'sphere of reflection' commonly known as 'Ewald sphere' is a useful device for interpretating diffraction patterns.

Generally at high energies, such as 100 KeV, the reflection sphere can be approximated to a plane section through the reciprocal lattice,

and consequently the RHEED pattern observed corresponds to this plane section lying perpendicular to the direction of the incident beam. Hence P' lies very near to the diffraction spot P, Fig (3.11b).

With a small value of Bragg angle the relationship for the constructive interference can be given as follows

$$\lambda L = R_{hkl} d_{hkl} \qquad (3.31)$$

where L is the effective camera length,

R_{hkl} is the radius of the rings or spots recorded on a film.

d_{hkl} is the interplanar spacing,

λ is the wavelength used in the experiment.

This camera equation was used to obtain the interplanar spacings d_{hkl} from the observed diffraction patterns.

3.6.3 X-ray Fluorescent Analysis (XRF):

Bulk analyses of some of the samples were made (both qualitatively and quantitatively) by using a Philips PW1400 X-ray fluorescence spectrometer. A schematic diagram of the system is shown in Fig (3.12). The primary beam falling on the sample has a short wavelength and is thus sufficiently energetic to excite the characteristic X-ray spectra of each of the elements present in the sample. The secondary X-rays emerging from the sample are wavelength analysed by reflection from one of a series of analysing crystals (e.g. LiF_{220} = 1.424 Å; Penta erythrintol d_{002} = 4.371 Å). The line positions and intensities are measured either by a scintillation or a flow proportional (90% Ar + 10% CH_4) detector. Scintillation counters are usually used to detect the heavier elements, whereas the flow proportional detectors are used to detect the lighter elements. With careful choice of instrumentation the intensities of the detected radiation can be made to be proportional to the concentrations of the individual elements present in the sample, hence it is possible to quantify the results. The

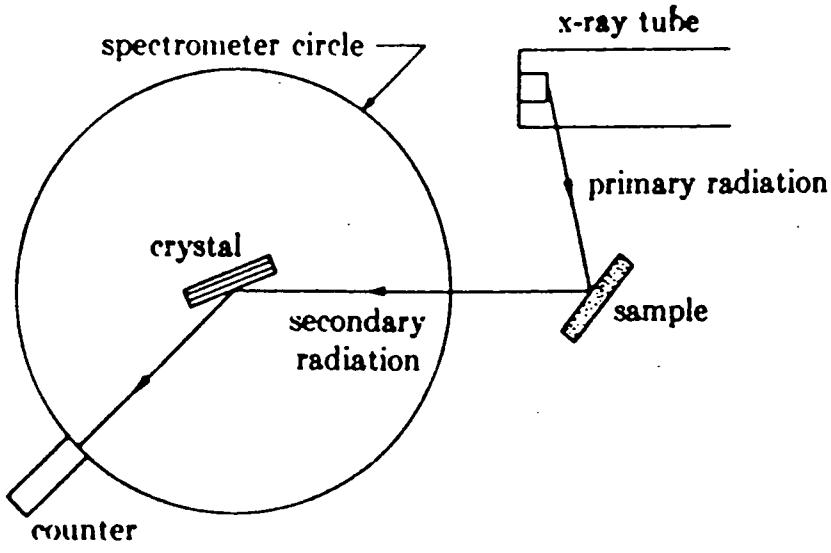

Fig. 3·12 Fluorescent x-ray spectroscopy.

measured values of the angle 2θ identify the elements present in the sample, since the emission wavelengths of all the elements are now well known to a high degree of precision.

CHAPTER THREE

REFERENCES

3.1 K.L.Chopra, Thin Film Phenomena, McGraw Hill Co (1969) p86.

3.2 W.T.Tsang, J. of Appl.Phys. 49 (1978) 1031.

3.3 H. Yonezu, I. Sakuma, K.Kobayashi, T.Kamejima, M.Ueno and Y.Nannichi., Japan. J. of Appl.Phys. 12 (1973) 1585.

3.4 W.B.Joyce and S.H.Wemple, J. of Appl.Phys. 41 (1970) 3818.

3.5 L.I.Maissel and R.Glang, Handbook of Thin Film Technology, McGraw Hill, New York, (1970).

3.6 L.J.Van der Pauw, Philips Res.Rept., 13:1 (1958).

3.7 R.Puteh, Ph.D. Thesis, University of Durham, (1984) p.10.

3.8 E.R.Gough and J.O.Isard, Proc.IEE 116 (1969) 471.

3.9 Wayne-Kerr Co.Ltd., Handbook No.B224 (1975).

3.10 A.S.T.M.(American Society of Testing and Materials) part 29, D150-65T 68 (1966).

3.11 A.H.Scott, H.L.Curtis, J. of Research of the National Bureau of Standards, 22 (1939) 747.

3.12 P.J. Harrop, Dielectrics, Butterworths, London (1972) p.122.

3.13 D.Evans and J.S.Thorp, J.Phys. E: Sci.Instrum, 20 (1987) 575.

3.14 G.A.G.Bennet, Electricity and Modern Physics, Edward Arnold Ltd, London (1971) p.193.

3.15 P.J.Harrop, Dielectrics, Butterworths, London (1972) p.54.

3.16 K.V.Rao and A.Smakula, J. of Appl.Phys. 37 (1966) 319.

3.17 The Q-Meter (in the theory and practice), Marconi Instruments Ltd, England (1961).

3.18 J.I.Goldstein (ed.) and H.Yokowitz (ed.), Practical Scanning Electron Microscopy, Plenum Press (1975).

CHAPTER FOUR

DIELECTRIC STUDIES ON ALUMINA

4.1. Single Crystal Alumina

4.1.1 Structural and Analytical Features

Aluminium oxide (Al_2O_3) has a trigonal unit cell with lattice parameters a = 4.758 Å, c = 12.991 Å [4.1]. In principle, many materials can be grown in single crystal form from the melt, provided they melt congruently, do not decompose before melting, and do not undergo a phase transformation between the melting point and room temperature [4.2]. For the growth of single crystal alumina, both Czochralski and vapour phase methods of crystal growth have been employed ; both techniques can give a high degree of crystal perfection (i.e. up to the standards required for laser operation) though the vapour phase growth method gives more control over impurity content.

Ruby (chromium doped aluminium oxide) which is well known as a laser material, can be formed in an appropriate condition by introducing a controlled amount of chromium ions in the alumina lattice, where the aluminium ion is substituted by the chromium ion. In Czochralski growth chromic oxide is used as the source of the chromium ions for doping. Doped alumina single crystals containing other transition metal ions (e.g. titanium, iron etc) can be grown in a similar way.

It is noticeable from the experimental evidence quoted in the literature [4.3-4.6] that the crystal structure, the orientation, degree of crystallinity as well as the dopant or impurity have a significant influence on the physical properties of the materials. It is evident that the estimation of dopant concentration and of impurity content (either in the form of a separate phase or by replacing the host ions) present in the system is necessary to characterise the material. In the crystals used in the present investigations, it was

known from previous studies that both the crystal perfection and purity were exceedingly high. The early X-ray perfection studies were confirmed by the present RHEED examination, which revealed sharp diffraction spots and Kikuchi lines (Fig 4.1a) and also by the clarity of the X-ray diffraction spots in the back reflection X-ray photograph reproduced in Fig 4.1b. The pure alumina single crystal had impurity contents, as determined by mass spectrometry and XRF, of less than 10 ppm (chiefly iron) and the ruby contained 0.05% chromium. They thus formed useful reference standards against which the effects of polycrystallinity or the deliberate introduction of additives could be assessed.

4.1.2 Room Temperature Results

The crystals of pure and chromium doped alumina were first examined at room temperature in the frequency range 5 x 10^2 Hz to 3 x 10^4 Hz using the Wayne Kerr Bridge method and then by the Q-meter resonant technique which extended the frequency coverage from 3 x 10^4 Hz to 1 x 10^7 Hz. The results for the frequency variations of $\epsilon' - \epsilon_\infty$ and ϵ'' for these materials are shown in (Figs 4.2 a,b). The single crystal samples were nominally cut with their surfaces either parallel or perpendicular to the C-axis. The dielectric permittivities at 1.0 KHz were found to be 9.6 for the chromium doped crystal and 11.4 for the pure single crystal alumina respectively. These are fairly close to the reported values [4.7-5.11] and are found in between 9.3 (perpendicular to C-axis) and 11.5 (parallel to C-axis); the discrepancies can be fully accounted for by errors in the exact orientation of the slices. The values of $\tan\delta$ for the pure and chromium, doped crystals were 2.0 x 10^{-4} and 4.0 x 10^{-4} respectively.

One of the noticeable features of the behaviour of ϵ' and ϵ'' for the pure and chromium doped single crystals is the frequency independence. The data has been fitted to the Jonscher "Universal Law"

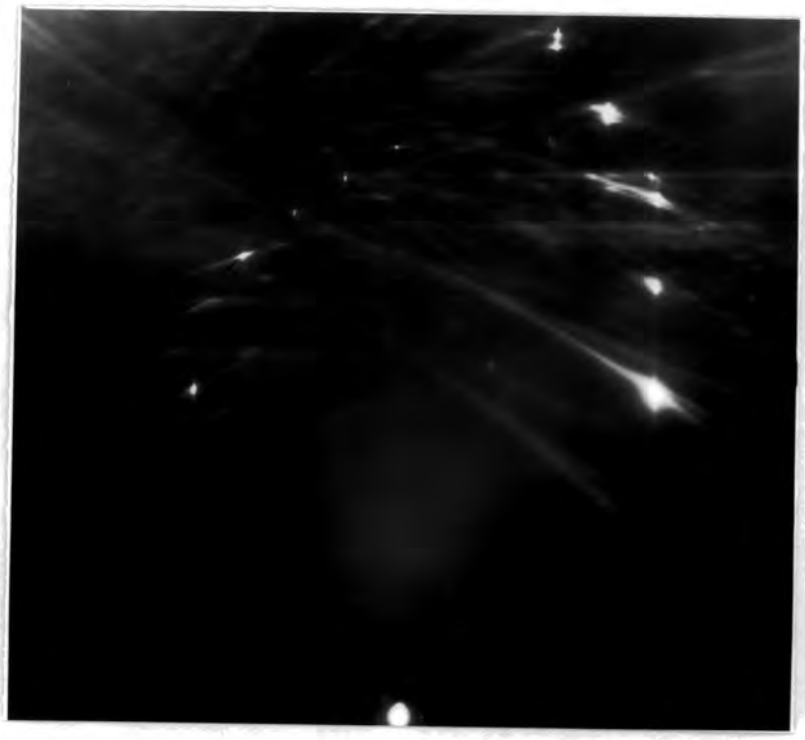

FIG 4.1(a): A typical RHEED pattern for Cr/Al_2O_3 single crystal.

FIG 4.1(b): Back reflection photograph for Cr/Al_2O_3 single crystal
$Cu\text{-}K_\alpha$ radiation ; specimen to film distance (3.0 cm)

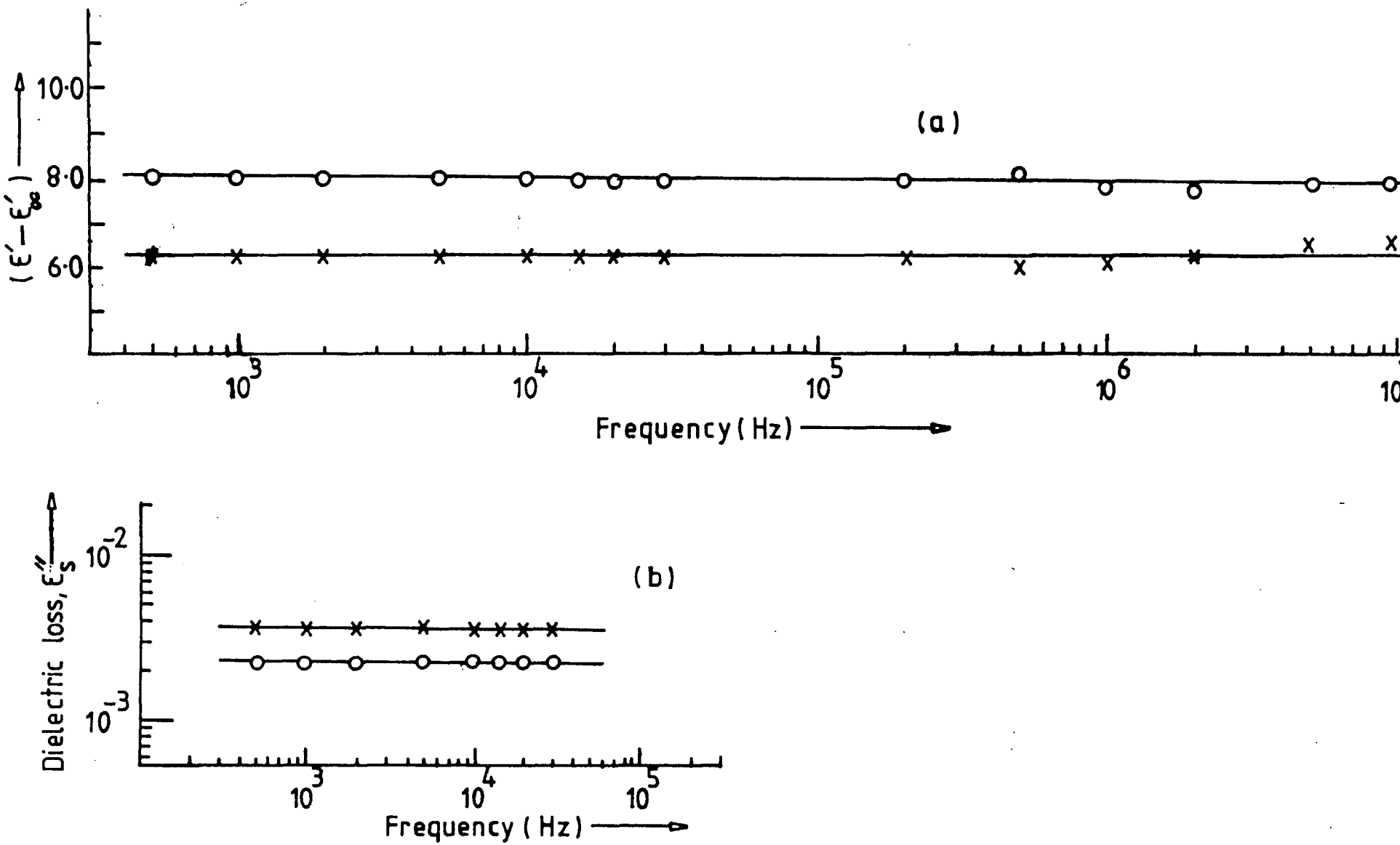

Fig. 4·2 Frequency variation of (a) $(\epsilon' - \epsilon'_\infty)$ and (b) dielectric loss for Al_2O_3 single crystal (|| to C — axis) (o) and Cr/Al_2O_3 single crystal ($\perp$ to C — axis) (x).

of dielectric response [4.12], according to which the relations between the frequency and the dielectric permittivity, ϵ' and dielectric loss, ϵ'' can be expressed in the following form

$$\left(\epsilon' - \epsilon'_{\infty}\right) \propto \omega^{n-1} \qquad (4.1)$$

and $$\epsilon'' \propto \omega^{n-1} \qquad (4.2)$$

where ϵ_{∞} is the limiting value of the dielectric permittivity at high frequency, ω is the angular frequency and the exponent n is usually close to unity. For these pure and chromium doped alumina single crystals the values of n are found to be 0.98 ± 0.02 from the ϵ' variation and $n = 0.96 \pm 0.04$ from the ϵ'' variation, where the value of ϵ_{∞} has been deduced from the optical refractive index, n ($n = \sqrt{\epsilon_{\infty}} = 1.760$). The conductivity mechanism responsible for materials where the exponent approaches unity has been suggested by Jonscher to be screened hopping [4.13]. The addition of a very small percentage (0.05 percent) of chromium ion in the alumina lattice neither distorts the lattice nor shows any appreciable change in the dielectric properties. Previous work in this group [4.14 - 4.16] on pure and doped single crystal magnesium oxide, silicon nitride and oxynitride glasses showed a similar type of behaviour. In these materials, the conduction mechanism was also believed to be hopping with n values very close to unity.

4.2 Pure Polycrystalline Alumina

4.2.1 Structural and Analytical Features

The polycrystalline alumina specimens examined were similar to

high grade commercial substrates used for high performance packaging. The specimens were clear white in appearance. The available analytical data (mainly from XRF) showed that the transition metal ion impurity levels were less than about 10 ppm. This material is made by well established ceramic technologies, which involve high temperature sintering of the green ceramic in oxygen ambients. Consequently a fairly high density product is obtained. Here the measured density was found to be 3.86 gm/c.c. as compared with the X-ray density of 3.965 gm/c.c. This gives a packing fraction of 0.97. Several samples (of nominally the same composition, prepared by the same methods) were examined by the scanning electron microscope. A typical micrograph is shown in Fig (4.3). This shows that the crystallite size was comparatively large - the mean size being about 5 μm and that the boundaries appear to be voids rather than containing a second crystalline phase. The same specimens were also examined by EDAX giving, as expected, a spectrum which revealed only an aluminium line, (Fig 4.4). As will be described in the following section signals about a centimetre high were obtained, under identical equipment operating conditions, for titanium, manganese and iron in impure alumina at levels of about 1.5%. Consequently, the lack of detectable signals implied that the impurity concentrations were certainly less than 0.2%.

4.2.2 Room Temperature Results

Measurements were made over the same frequency range as was used for the single crystal specimens. A correction was made for the measured porosity, and, on the assumption that the material contained only aluminium oxide grains and voids (air), the values of the equivalent solid permittivity and loss were determined. Thus, the experimentally measured permittivity (ϵ'_p) was converted to the

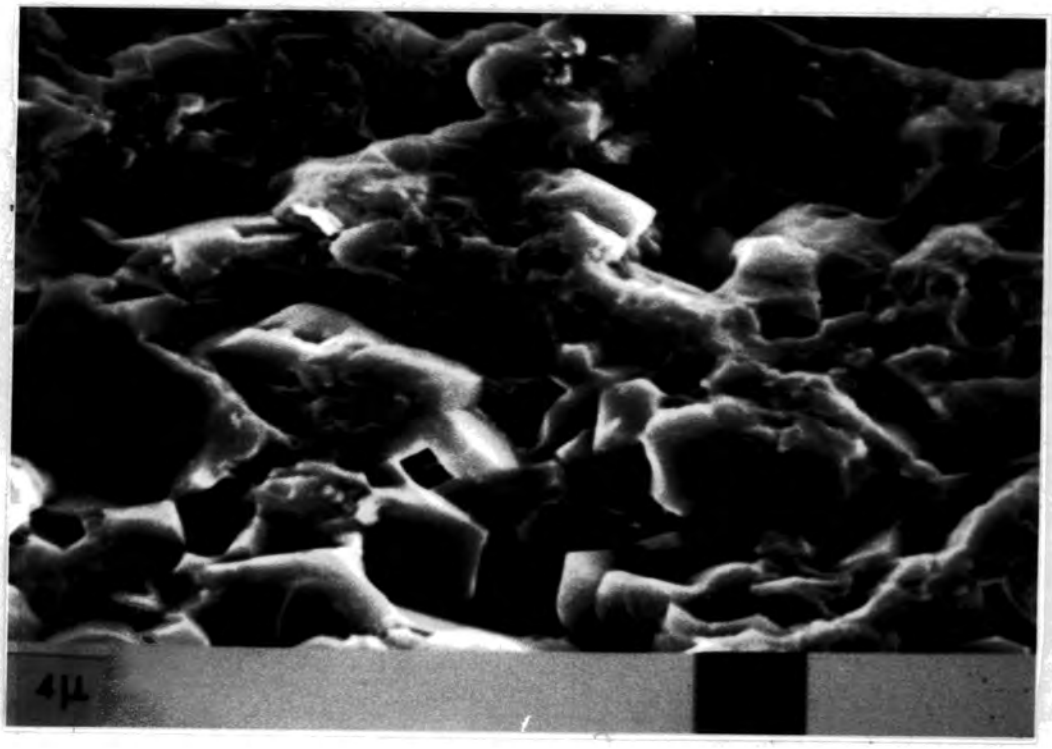

FIG 4.3 : A typical SEM micrograph for pure polycrystalline alumina

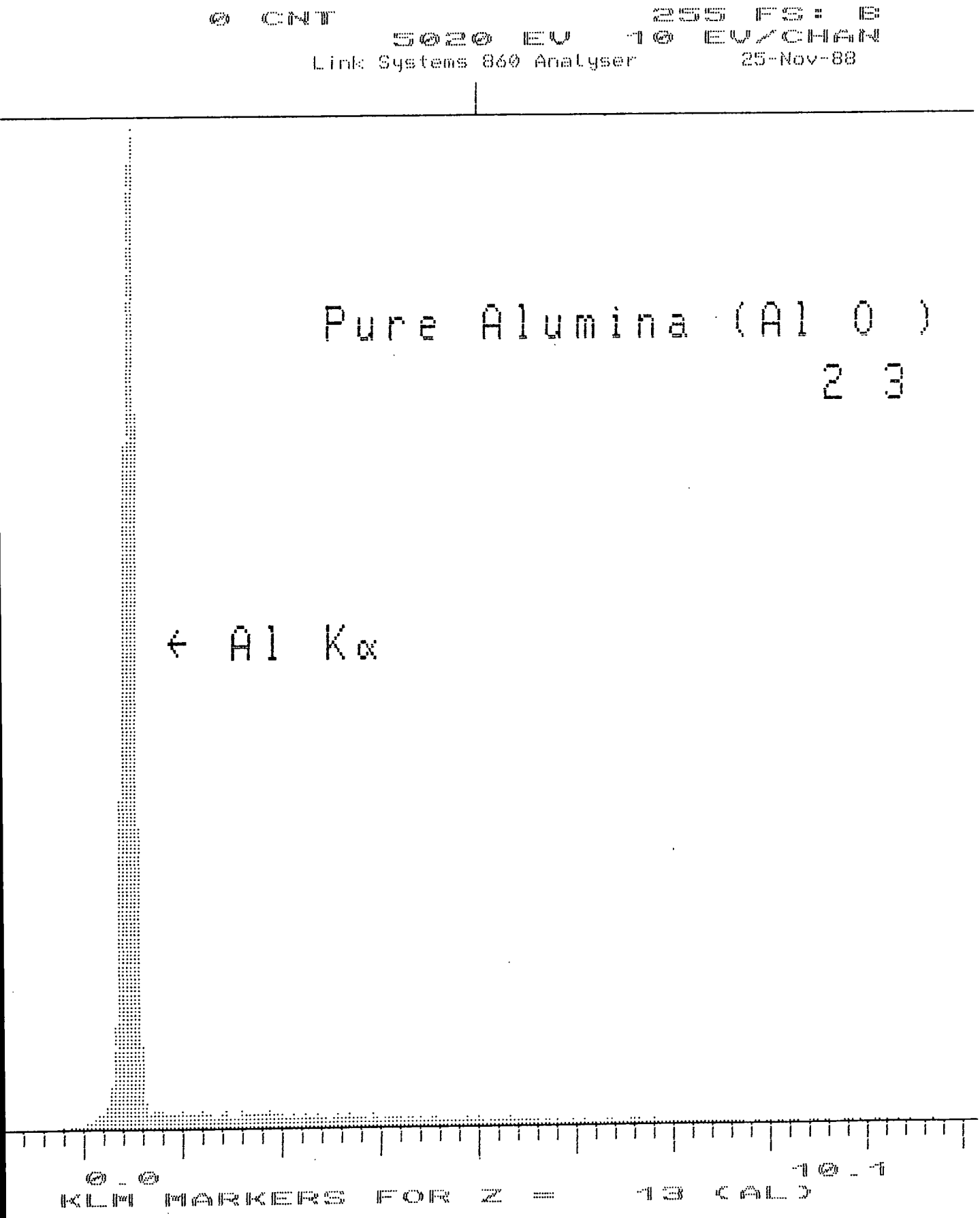

FIG. 4-4: A typical EDAX spectra for pure polycrystalline alumina

equivalent solid value (ϵ'_s) by the relation

$$\epsilon'_s = \left[\frac{\epsilon'_p - 1+\delta}{\delta} \right]^{1/3} \tag{4.3}$$

and the corresponding loss (ϵ''_p) to the equivalent solid loss (ϵ''_s) by

$$\epsilon''_s = \left(\frac{\epsilon''_p}{\delta} \right) \left(\frac{\epsilon'_s}{\epsilon'_p} \right)^{2/3} \tag{4.4}$$

where δ is the packing fraction, (see Chapter 3, Section 3.2.6)
The results are given in Fig (4.5a,b). As regards permittivity, it can be seen that again frequency independent behaviour is observed both for the ϵ'_s and the ϵ''_s variations. The n values obtained from the two plots were $n = 0.98 \pm 0.2$ and $n = 0.96 \pm 0.4$ respectively which again are in excellent agreement with each other. The magnitude of the permittivity, $\epsilon'_s = 10.185$, is between the two limits of 11.4 and 9.4 for the parallel and perpendicular orientations of the single crystal material, respectively. Assuming a completely random orientation of grains in the sintered material, the permittivity should be the arithmetic mean of the two extreme values of the single crystal, i.e. $\frac{11.4 + 9.4}{2} = 10.4$. The measured value is in good agreement with this suggesting that there is very little if any preferred orientation in the specimen. This result is confirmed by back reflection X-ray examination, (Fig 4.6), which shows continuous Debye-Sherrer rings with no evidence of arc formation.

As regards the dielectric loss the measured value of ϵ''_p of 1.4×10^{-2} is increased to the value ϵ''_s of 1.5×10^{-2} by allowing for the

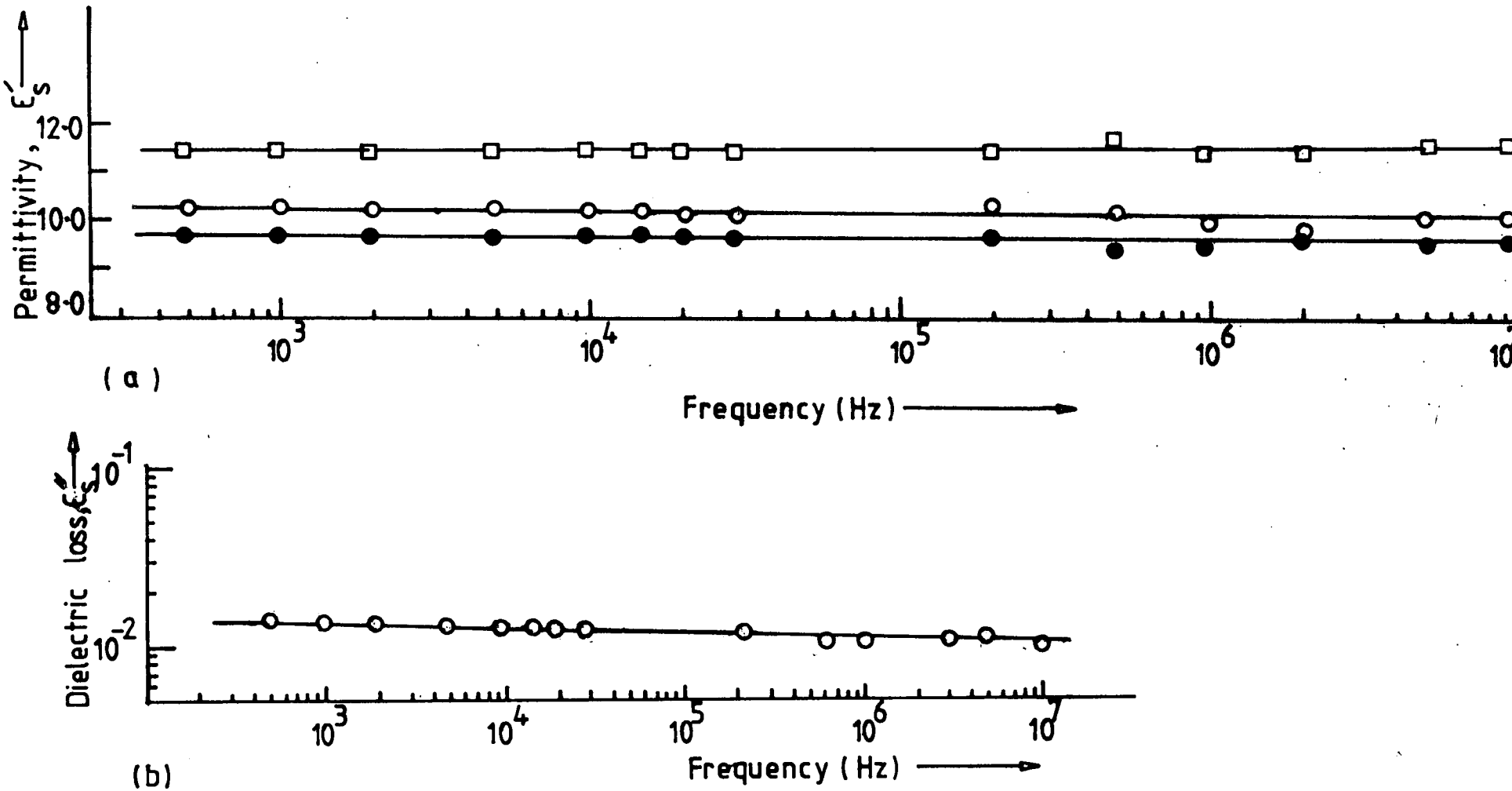

Fig. 4·5 Frequency variation of (a) permittivity and (b) dielectric loss for pure polycrystalline alumina (○) together with additional data of permittivity for Al_2O_3 single crystal (∥ to C axis) (□) and Cr/Al_2O_3 (⊥ to C—axis) (●) at 20°C.

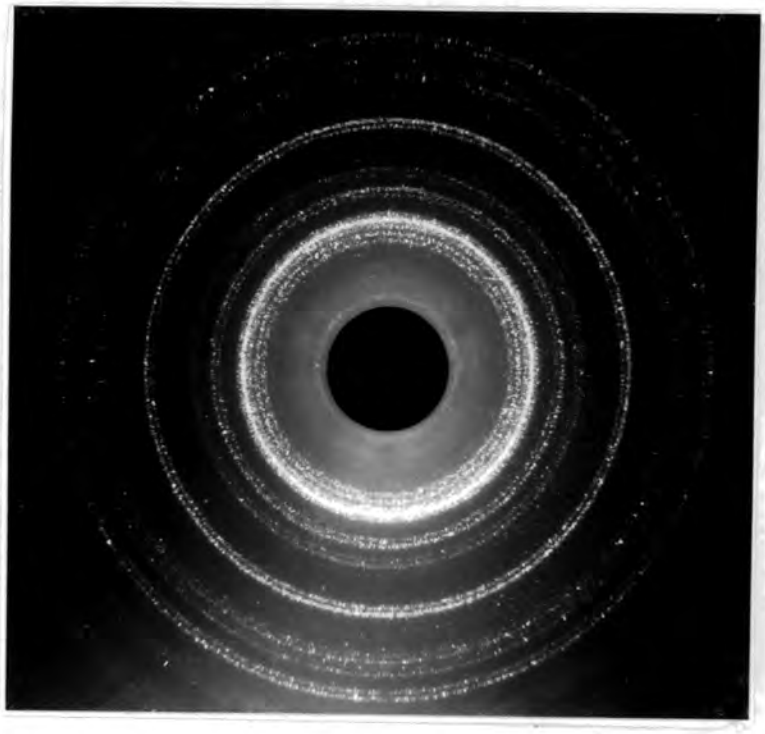

FIG 4.6 : B ack reflection photograph for pure polycrystalline alumina. Cu-K_{α} radiation ; specimen to film distance (3.0 cm)

air in the voids. The air has a lower value of loss than the grain, hence ϵ''_s should be greater than ϵ''_p as was found. Comparison of ϵ''_s for this pure polycrystalline alumina with the value of ϵ''_s for the pure single crystal material shows that the former is an order of magnitude larger than the latter; thus ϵ''_s (polycrystalline) equals 1.5×10^{-2}, whereas ϵ'' (single crystal) 3.84×10^{-3}. This can be attributed to the presence of the grain boundaries. The SEM evidence suggests a mean grain size of about 5 μm and so taking the dimensions of the sample used, calculation shows that there are about 10^8 grain-boundaries. (The volume of disc shaped sample between the electrodes has a diameter of 6mm and a thickness of 0.6 mm. With a 5 μm grain size there will be 1.2×10^3 grains across a diameter and 1×10^2 grains along the thickness. Hence in the total volume considered there will be approximately $[\pi \times (10.6 \times 10^3)^2 \times 10^2]$ i.e. 1.1×10^8 grains, each of which is assumed to contribute one grain boundary).

4.3 BLACK ALUMINA

4.3.1 Structural and Analytical Features

In some types of package there is a requirement for an optically opaque substrate in order to make the semiconductor circuits less susceptible to adverse effects caused by optical irradiation. By the addition of certain metal oxides (chiefly those of iron and manganese) the substrate can be made non-transparent and it exhibits a black colouration ; these materials are commonly termed "black alumina". Since the impedance of the input and output conductor leads to the chip are in part determined by the permittivity and loss of the substrate it is of interest to ascertain what degree of opaqueness can be achieved without causing too large a rise in $\tan\delta$. Ideally $\tan\delta$ values in the range 10^{-4} to 10^{-3} are preferred, but package designs could be made to accommodate $\tan\delta$ values lying between 10^{-3} and 10^{-2} as an upper limit.

The samples of black alumina examined were chosen as

representative of this type of commercially available ceramic and the main interest was to establish the effect of the relatively large concentrations of additive on the dielectric properties. They were examined by XRF, SEM, EDAX and RHEED techniques. The XRF analysis showed that iron, manganese and titanium were present at levels of 1.5%, 1.5% and 1.1% respectively together with other metals (i.e. Ba, Zr, Sr, Rb, Zn, Cu, Ni, V, Cr and Ga) at trace levels not exceeding 100 ppm. This was confirmed by the EDAX spectra, e.g. Fig 4.7, taken from a selection of areas of the sample, all of which showed clear peaks corresponding to iron, manganese and titanium. The SEM micrograph, (Fig 4.8), shows a relatively large grain size, >10 μm on average, together with evidence for additional phases, of much smaller size ; there appear to be segregation of the impurities to the grain boundaries. Some electron diffraction studies were made in an attempt to confirm the existence of additional phases by a comparison of the d-values observed with those expected from alumina. A typical RHEED pattern is given in Fig.4.9. It can be seen that a spotty ring pattern was obtained indicative of a large grain size. Analysis of this pattern was undertaken and Table 4.1 compares the d-values observed with those listed for α-Al_2O_3 in the ASTM card index (13-534). This shows that while many of the observed lines gave a fair fit to the alumina lines, there were a considerable number of extra lines in the electron diffraction pattern ; these extra lines are asterisked (*). It is likely that the impurities (iron, manganese and titanium) will not be present as elements, but rather as oxide because the processing of the ceramics involves heat treatment in air or oxygen. Consequently, an attempt was made to match the extra lines to those expected from α-Fe_2O_3 (Hematite), TiO_2 (Brookite) and MnO_2 (Ramsdellite). This is shown in Table 4.2. There is some correspondence, particularly with MnO_2, though much more accurate data would be needed in order to

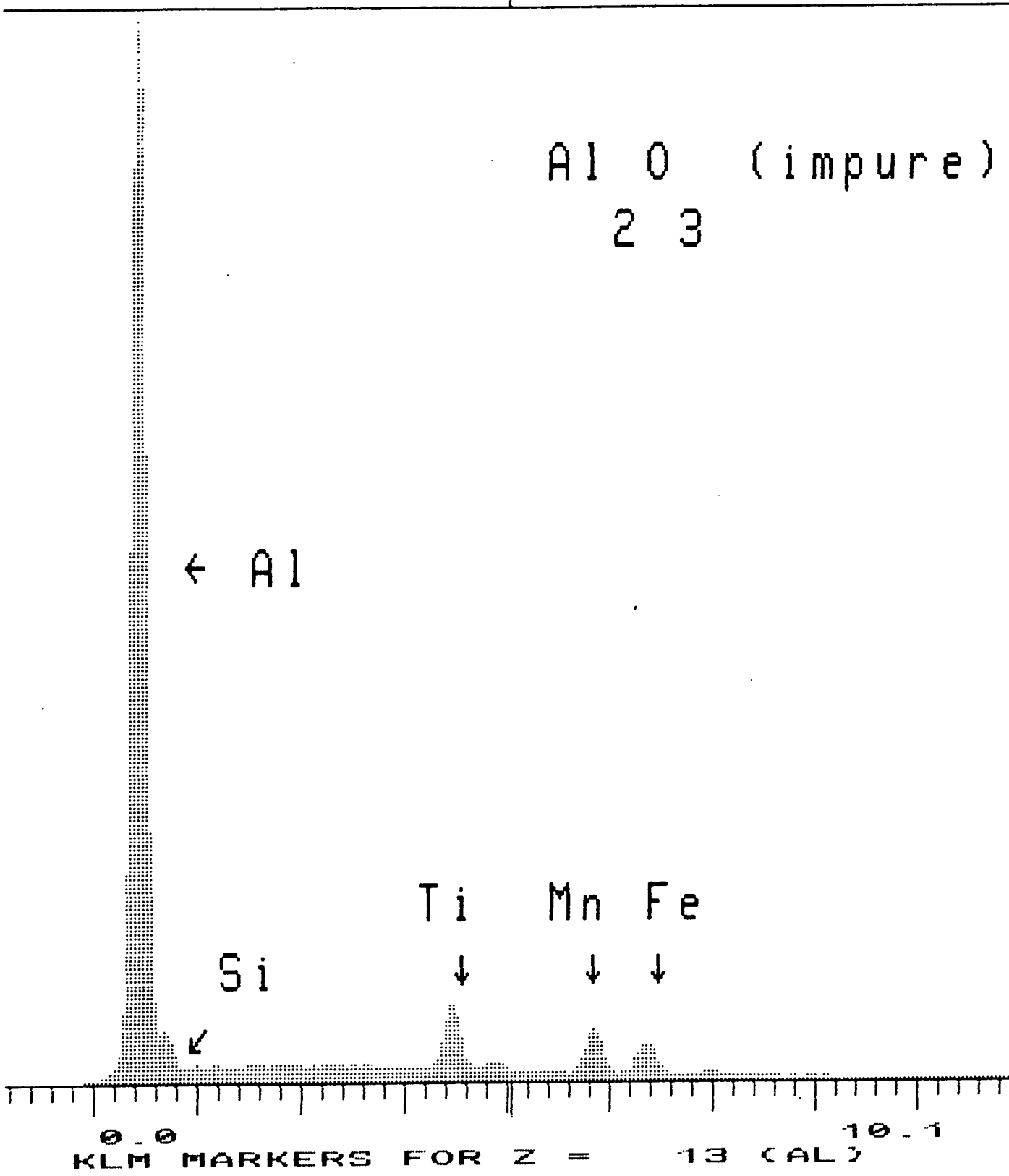

FIG 4.7: A typical EDAX spectra for black alumina

FIG 4.8: A typical SEM micrograph for black alumina

FIG 4.9: A typical RHEED pattern for black alumina

TABLE 4.1 : Comparison of 'd' values obtained from experimental electron diffraction pattern of black alumina with reference data for pure α-Al_2O_3. (13-534).

Electron diffraction		ASTM Index (13-534) (α-Al_2O_3)			Additional Lines
d_{hkl} (Å)		d_{hkl} (Å)	I/I_1	hkl	d(Å) value
4.305*	S				4.305
3.767	M	3.479	75	012	
2.87*	VS				2.87
2.564	VS	2.552	90	104	
2.41	VS	2.379	40	110	
2.23*	VS				2.23
2.15*	VS				2.15
2.04	VS	2.08	100	113	
1.88*	W				1.88
1.772	M	1.74	45	024	
1.674*	M				1.674
1.607	M	1.601	80	116	
1.506*	M				1.506
1.435*	VS				1.435
1.40	VS	1.404	30	124	
1.369	VS	1.374	50	030	
12.8*	W				1.28
1.23	W	1.239	15	1.01.10	
1.179*	W				1.179
1.159	W	1.1470	5	223	
1.137*	W				1.137
1.116	W	1.0988	7	0.2.10	
1.057*	W				1.057
1.039	W	1.6426	13	226	
0.972	W	0.9819	3	404	
0.920*	W				0.920
0.899	W	0.9076	13	324	

TABLE 4.2: Analysis of Extra Lines observed in Electron Diffraction Pattern of Impure (black) alumina. (N.B. spacing marked with one asterisk is also present in the spectrum of α-alumina).

Black alumina (electron diffraction)		ASTM index (7-222)			ASTM index (13-534)			ASTM index (16-687)		
		MnO_2			Fe_2O_3			TiO_2		
d_{hkl}(Å)		d_{hkl}(Å)	I/I_1	hkl	d_{hkl}(Å)	I/I_1	hkl	d_{hkl}(Å)	I/I_1	hkl
4.305	S	4.07	100	110						
2.87	VS							2.9	90	121
2.564*	VS	2.55	100	130	2.69	100	164	2.476	25	012
					2.51	50	110			
2.23	VS	2.19	70	121	2.201	30	113	2.44	18	022
2.15	VS							2.133	16	221
1.88	W	1.907	70	131	1.838	40	024	1.893	30	231
1.674	M	1.660	80	221	1.690	60	116	1.691	20	320
								1.662	30	241
1.506	M	1.473	80	151	1.484	35	214	1.494	10	052
1.435	VS	1.433	50	002				1.452	12	203
		1.369	80	061				1.434	10	213
1.28	W	1.272	60	170	1.310	20	1010			
							119			
1.179	W									
1.137	W				1.141	12	134	1.417	10	161
1.057	W				1.055	18	2110			
0.920	W				0.9080	25	1310			

establish precise details.

4.3.2 Room Temperature Results

As with the other alumina samples, the black alumina specimens were examined over the frequency range 5 x 10^2 Hz to 1 x 10^7 Hz. The permittivity versus frequency plot is shown in Fig 4.10a, which includes for comparison the data for the pure polycrystalline alumina. Two features are evident. In the first place, there is some frequency dependence with ϵ'_s rising at low frequencies. Above 1 x 10^4 Hz the values of ϵ'_s for black alumina are nearly the same as those for pure polycrystalline alumina but at 5 x 10^2 Hz ϵ'_s is about 19% higher than ϵ'_s for pure alumina.

The corresponding data for the dielectric loss is given in Fig 4.10b. Here it is seen also that the loss is no longer frequency independent, rising markedly at the lower frequencies, and is also much greater than for the pure polycrystalline material at all frequencies. This additional increase above the values for pure polycrystalline alumina must be attributed to the impurity additives. The values of $\tan\delta$ for the black alumina was 1.3 x 10^{-1} compared with 1.4 x 10^{-3} for the pure alumina at 5 x 10^2 Hz and 6 x 10^{-3} compared with 1.3 x 10^{-3} at 1 x 10^6 Hz. It is evident that the behaviour cannot be accounted for on the basis of the Universal Law of dielectric response. There is strong evidence that the overall dielectric properties of the black alumina are determined in a complex manner, not only by the space charge polarisation at the grain boundaries but also by the dielectric properties of the individual additives. Similar effects have been reported in the literature [4.17-4.20]. The present result is very similar to that of Rao and Smakula [4.17], where they attributed this effect to the space charge present in the sample which depends on both the purity and perfection of the material. These authors also pointed out that the influence of this space charge effect is noticeable mainly

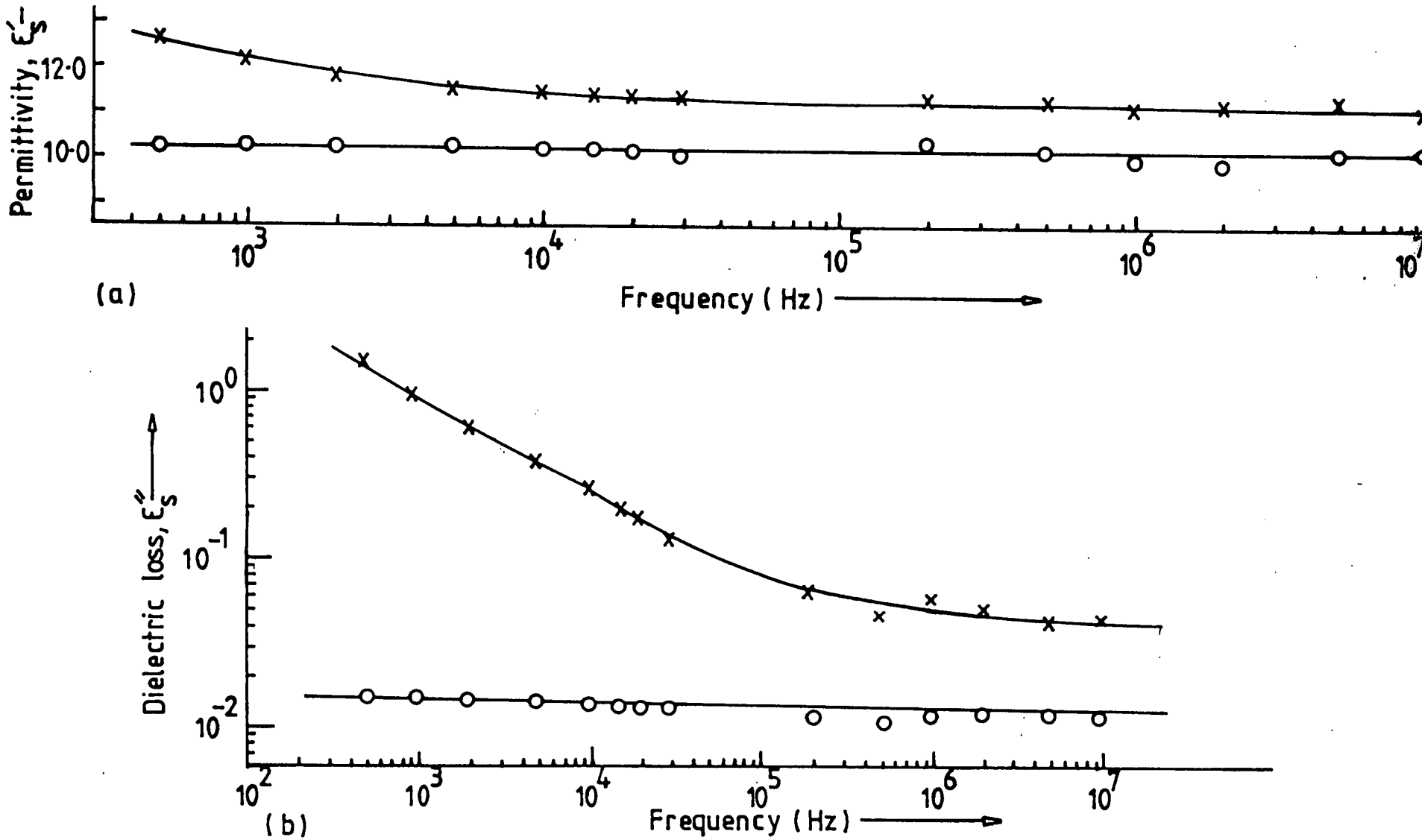

Fig. 4·10 Frequency variation of (a) permittivity and (b) dielectric loss for black alumina (x) and pure polycrystalline alumina (o).

in the low frequency regions.

4.4 THE TEMPERATURE DEPENDENCE OF DIELECTRIC PARAMETERS

4.4.1 Temperature Coefficient of Permittivity

The permittivity, (ϵ') dielectric loss, (ϵ'') and the a.c. conductivity $\sigma_{a.c.}$ for the three types of alumina sample were examined carefully in the temperature range of about 20° C to 700°C over the frequency range 5 x 10^2 Hz to 2 x 10^4 Hz. The temperature dependences of permittivity, (ϵ') for the reference single crystal Cr/Al_2O_3 over the frequency range 5 x 10^2 Hz to 2 x 10^4 Hz is shown in (Fig.4.11); the corresponding plots for the pure and impure alumina are given in the (Figs 4.12 and 4.13) respectively. In Fig.4.11 for Cr/Al_2O_3 single crystal, the permittivity versus temperature plot at each frequency shows that two distinctly dissimilar regions prevail in the response curve; (1) a linear region and (2) a non-linear region. The linear region for this particular material at 1.0 x 10^3 Hz extends up to about 270°C. It is important to note that this non-linearity commences at lower temperature for the lower frequencies and at relatively higher temperatures for the higher frequencies. Comparison of the three types of alumina sample examined in the present investigation shows that the extent of the linear region decreases with the increase in the crystalline imperfection (polycrystallinity) and almost disappears with the introduction of noticeable amounts of impurity.

Over the linear regions, the temperature coefficients of permittivity $\{(\epsilon'-1)\ (\epsilon' + 2)\}^{-1}\left(\frac{\partial \epsilon'}{\partial T}\right)_P$ for all the alumina samples were calculated by using Bosman and Havinga's formula [4.21]. The data is given in Table 4.3 which also includes values for other oxide ceramic materials. The temperature coefficient of permittivity for the chromium doped single crystal alumina was found to (7.52 x 10^{-6} K^{-1}), which is comparable to the sapphire (9.07 x 10^{-6} K^{-1}) studied at low

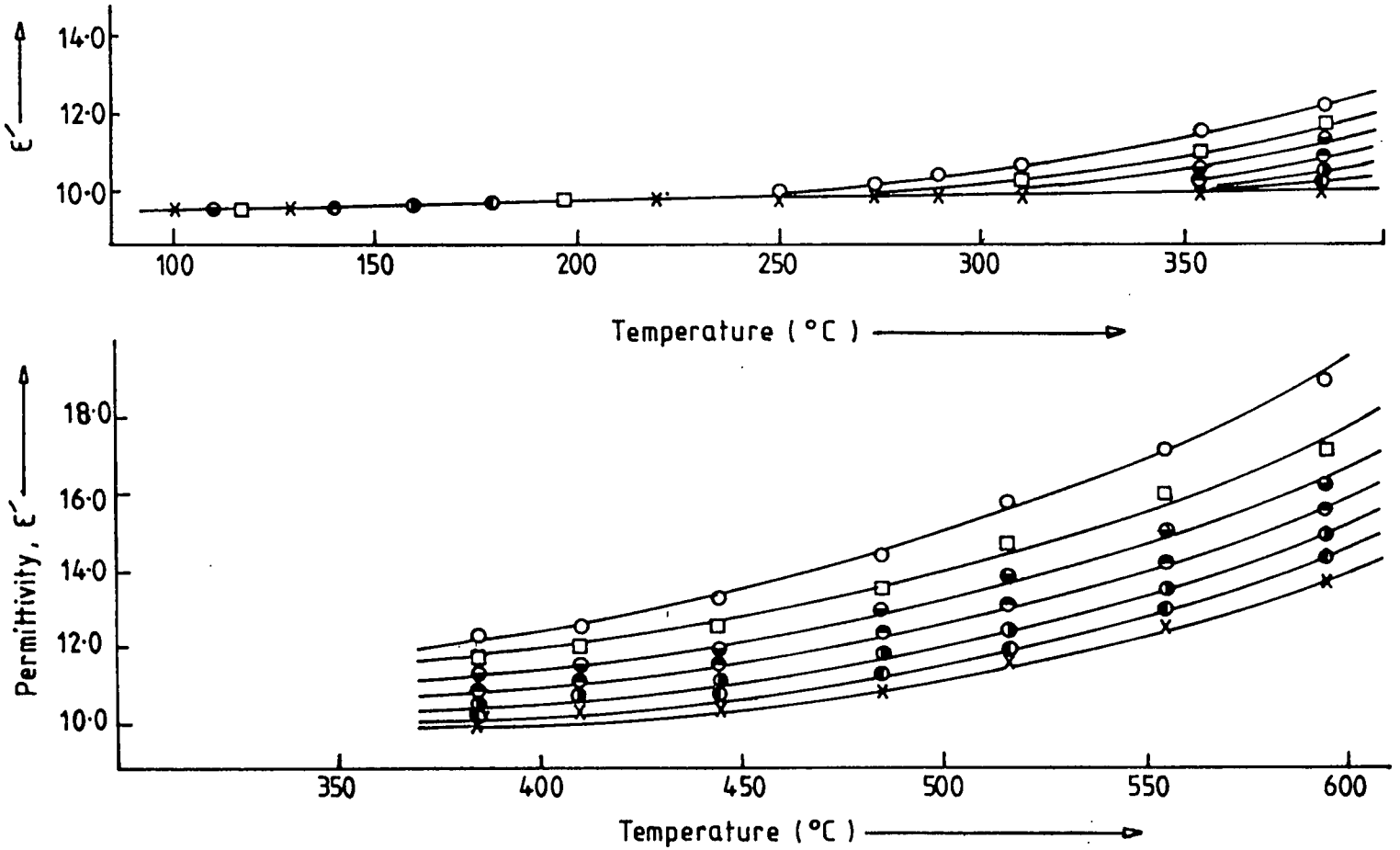

Fig. 4·11 Temperature variation of permittivity for Cr/Al_2O_3 single crystal ; high temperature range. Key : 5×10^2 Hz(○), 1×10^3 Hz (□), 2×10^3 Hz (●), 5×10^3 Hz(●), 1×10^4 Hz(●), $1{\cdot}5\times10^4$ Hz (◐) and 2×10^4 Hz(x).

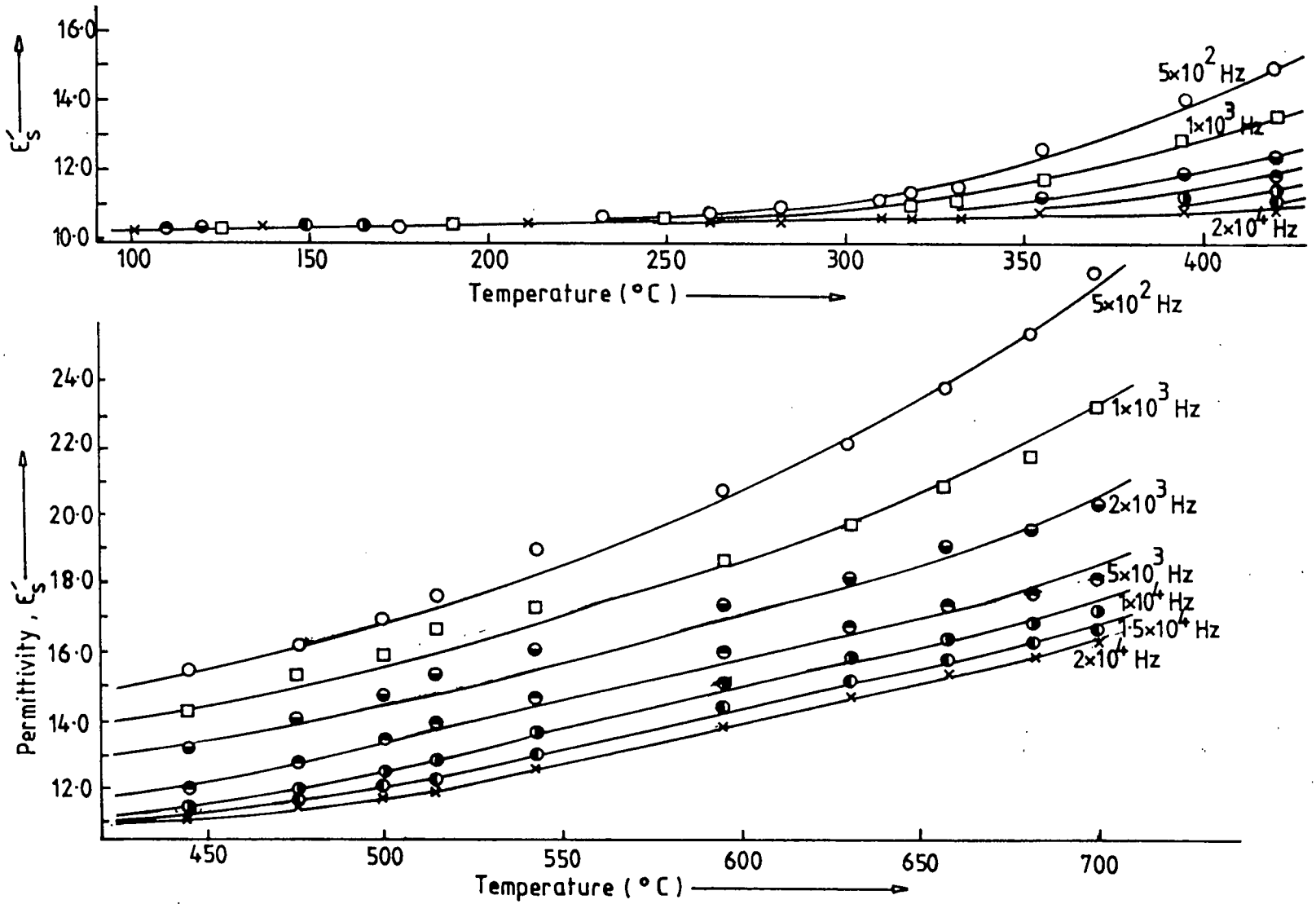

Fig. 4·12 Temperature variation of permittivity for pure polycrystalline alumina at differenr frequencies.

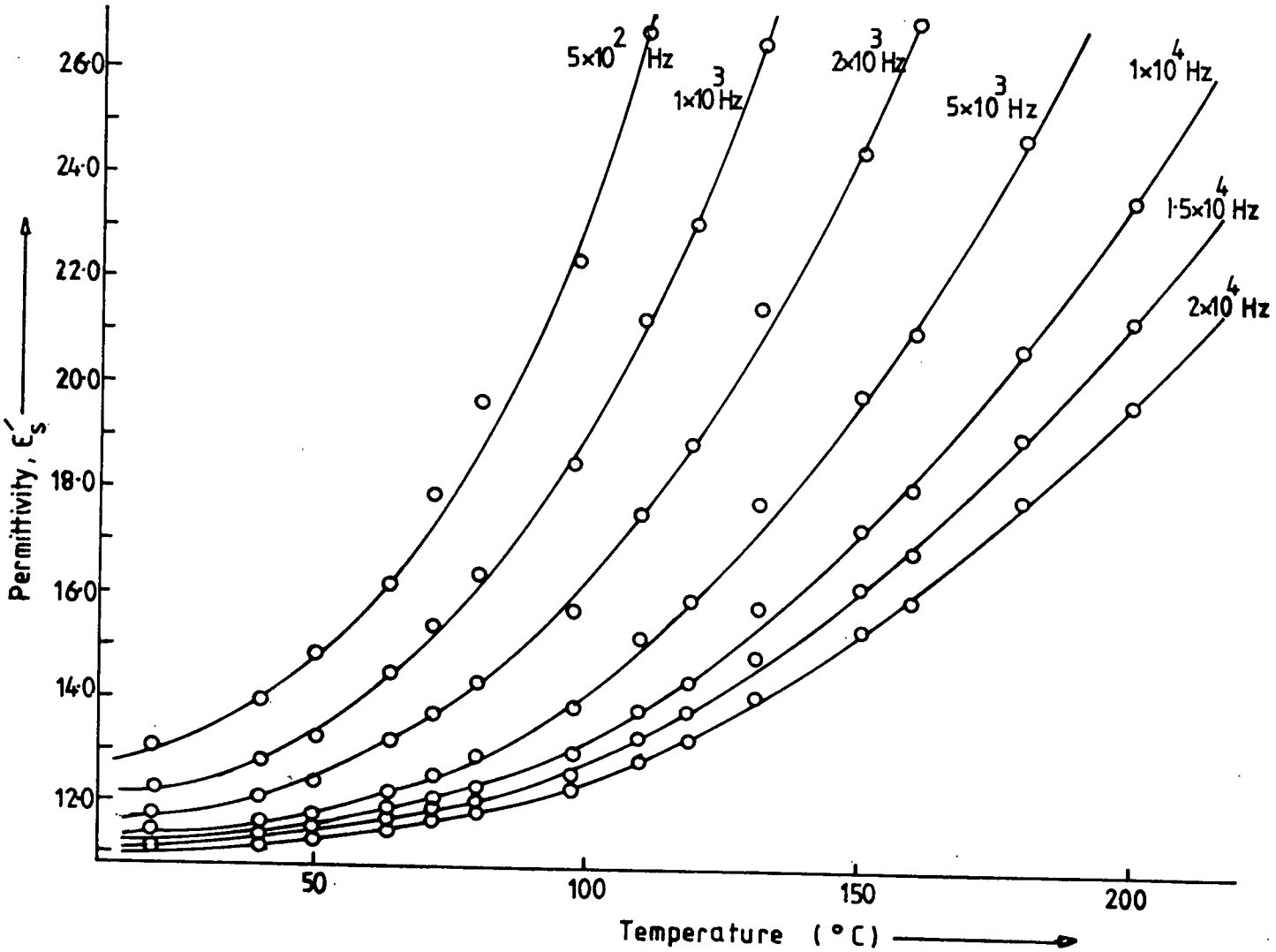

Fig. 4·13 Variation of permittivity with temperature for black alumina at different frequencies.

TABLE 4.3: Temperature Coefficients of Permittivity. $\{(\epsilon'-1)(\epsilon'+2)\}^{-1}\left(\frac{\partial\epsilon'}{\partial T}\right)_P$ of alumina compared with those of other oxide ceramics.

Samples	Freq. (KHz)	ϵ'(at rm.temp)	Temp. range.	$\{(\epsilon'-1)(\epsilon'+2)\}^{-1}\left(\frac{\partial\epsilon'}{\partial T}\right)_P$ (/K)	Refs.
Single crystal and pure polycrystalline alumina					
1.Chromium doped single crystal Cr/Al_2O_3 (perpendicular to C-axis)	1.0	9.6±0.02	20°C-270°C	7.52×10^{-6}	Present work
	1.0	9.6±0.02	85K-291K	9.1×10^{-6}	"
2.Pure poly-crystalline	1.0	10.2±0.02	20°C-260°C	9.31×10^{-6}	"
	1.0	10.2±0.02	85K-291K	9.15×10^{-6}	"
Previous published data					
(3) Sapphire (parallel to C-axis)	1.0	11.589±0.005	5.5K-380K	1.068×10^{-5}	J.Link et al
(perpendicular to C-axis)	1.0	9.395±0.005	5.5K-380K	8.895×10^{-6}	"
(4) Quartz (parallel to C-axis)	1.0	4.6368±001	5.5K-380K	2.19×10^{-6}	"
(5) Magnesium oxide, MgO	1.0	9.64±0.03	18°C -200°C	$1.02\pm0.02\times10^{-5}$	Thorp et al
(6) Impure (black) alumina	1.0	10.0±0.02	Non-linearity increases with temperature at all temperatures above 20°C (see Table 4.4)		(Present work)

temperature [4.22]. For the pure polycrystalline alumina sample this figure slightly increases and was found to (9.31×10^{-6} K^{-1}). It was impossible to calculate the temperature coefficient of permittivity for impure polycrystalline alumina on the same basis as the non-linearity started at room temperature.

However, it is clear from the shape of the variation that the values of $\{(\epsilon'-1)\ (\epsilon'+2)\}^{-1}\left(\frac{\partial \epsilon'}{\partial T}\right)_P$ over a limited temperature range will be very large and will also increase rapidly as the temperature is raised.

Measurements on chromium doped single crystal alumina, (Cr/Al_2O_3) pure and impure polycrystalline alumina were also carried out in the low temperature range from 293 K to 85 K. The results of these measurements for all the alumina samples are shown in (Figs 4.14a, b and c) for pure single crystal and polycrystalline alumina. The plots are linear; there is no measurable variation between 1.0×10^3 Hz and 2.0×10^4 Hz. Again, the temperature coefficients of permittivity, $\{(\epsilon'-1)(\epsilon'+2)\}^{-1}\left(\frac{\partial \epsilon'}{\partial T}\right)_P$ for these materials were found by using the Bosman and Havinga relationship [4.21] and are also given in Table 4.4. The values of the temperature coefficients at low temperature are seen to be in close agreement with those obtained on the same samples in the higher temperature range of about 20°C to 270°C. On the otherhand, the impure polycrystalline (black) alumina behaves in a different way.

As pointed out earlier the permittivity increases very rapidly with temperature above room temperature, Fig 4.13 and there is also a marked frequency dependence in that ϵ'_s is greater at a given temperature for a lower frequency than for a higher frequency, e.g. at 100°C ϵ' = 22 at 5×10^2 Hz and ϵ' = 11.8 at 2×10^4 Hz. On cooling below room temperature the permittivity at first still changes quite rapidly (Fig 4.14c) and there is also a residual frequency dependence of the same type as at higher temperatures, at temperatures below at

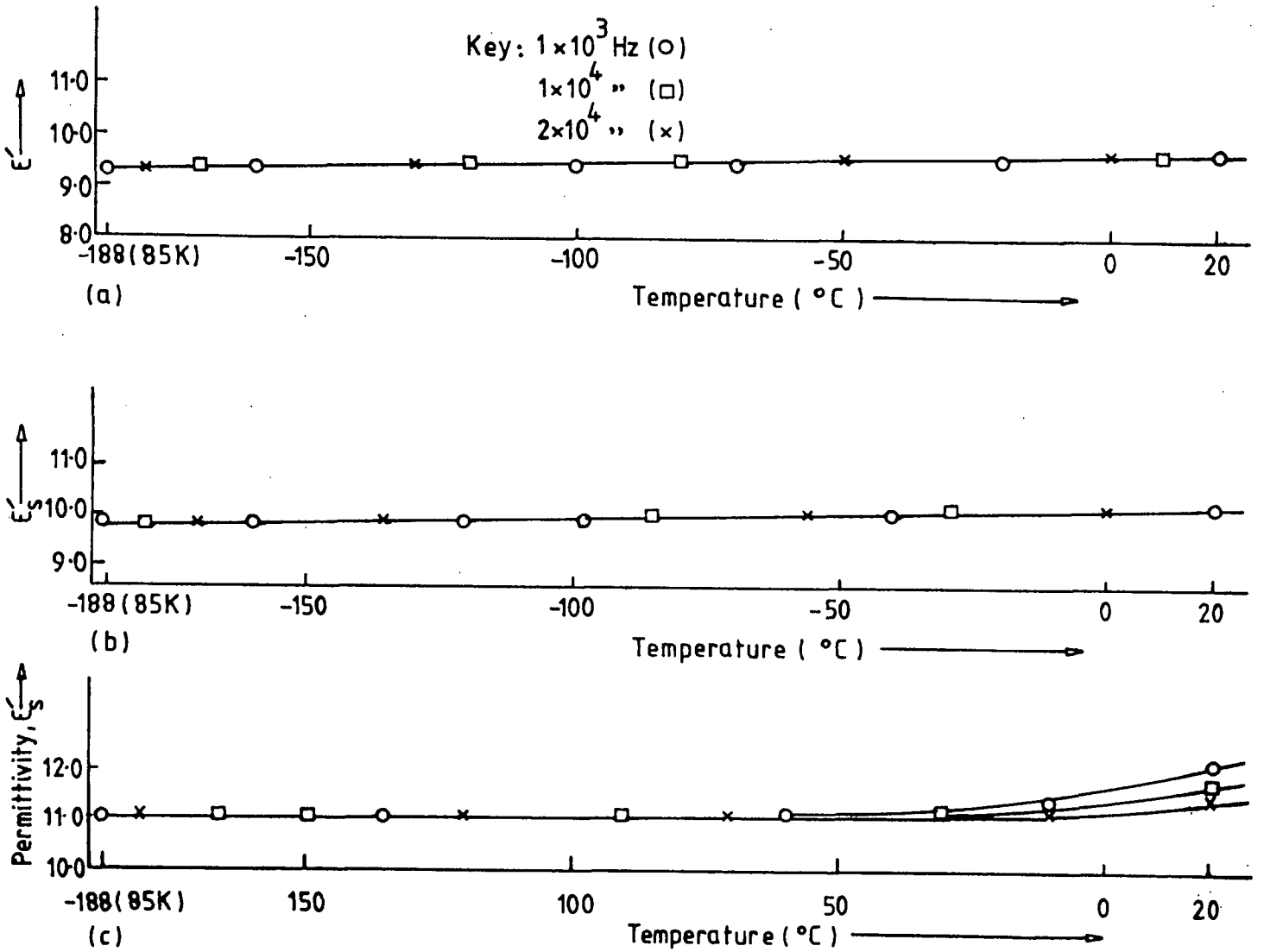

Fig. 4·14 Temperature variation of permittivity for (a) Cr/Al_2O_3 single crystal, (b) pure polycrystalline alumina and (c) black alumina ; low temperature region.

TABLE 4.4: Temperature Coefficients of Permittivity for Impure (black) Alumina compared with those for Pure Alumina.

Material	Temperature range	$\{(\epsilon'-1)(\epsilon'+2)\}^{-1}\left(\frac{\partial\epsilon'}{\partial T}\right)_p$ (/K)
(1) Cr/Al_2O_3, single crystal (perpendicular to C-axis)	-188°C to 20°C	9.10×10^{-6}
(2) Pure, poly-crystalline alumina	-188°C to 20°C	9.15×10^{-6}
(3) Impure (black) alumina	-188°C to 115°C	11.0×10^{-6}
	-115°C to 20°C	1.2×10^{-4}

-88°C, these effects are no longer noticeable and, although the permittivity varies slightly with temperature, this variation is approximately linear. In Table 4.4 the Bosman and Havinga formula has been used over limited temperature ranges in order to assess the change of $\left(\frac{\partial \epsilon'}{\partial T}\right)_p \left[\frac{(\epsilon'-1)}{(\epsilon'+2)}\right]^{-1}$, with temperature. It can be seen that in the lowest temperature range (i.e. -115°C to -185°C) the value of $\left(\frac{\partial \epsilon'}{\partial T}\right)_p \left[\frac{(\epsilon'-1)}{(\epsilon'+2)}\right]^{-1}$, is about $11.0 \times 10^{-6}\ K^{-1}$ which is very comparable to the values of $9.1 \times 10^{-6}\ K^{-1}$ and $9.15 \times 10^{-6}\ K^{-1}$ obtained for Cr/Al_2O_3 and pure polycrystalline alumina respectively. Thus it appears that at sufficiently low temperatures the contribution from impurities (and presumably also from imperfection) is negligible. It is generally accepted that at low temperattures the impurities [4.19] and imperfections [4.17] present in a dielectric material do not have any influence on the dielectric properties and the present data on impure (black) alumina supports this view. In a recent publication, Thorp et al [4.23] have reported the temperature dependence of permittivity in pure MgO and iron doped MgO single crystals. Their experimental results reveal the fact that in comparison with the undoped magnesium-oxide crystal the non-linear temperature dependence of permittivity commences at earlier temperatures with increasing percentage of iron doping. The authors also stated the possibility of the formation of some magnesio-ferrite in iron doped magnesium oxide (MgO) single crystals. To explain further the non-linearity in the temperature response, the authors considered the contribution of the quasi-conductivity [4.24] towards the significant increase in dielectric permittivity. They further added that this conductivity (quasi-conductivity) contribution was even possible in undoped MgO single crystals, which would have a significant vacancy concentration

coupled with impurities at the 5 ppm level or less [4.25]. In the Fe doped MgO crystal this effect was greatly enhanced because, using the trivalent dopant Fe^{3+}, one extra vacancy is introduced per two dopant atoms in order to achieve charge compensation. The authors concluded that this conductivity was likely to be strongly temperature dependent and, under the conditions where this type of conductivity is important, the Bosman and Havinga relationship would not be expected to apply. Fuchs [4.26] has also mentioned that the temperature has a complicated influence on the dielectric constant. Similar effects have also been reported in other oxides.

Thus in CoO, NiO and in their mixed crystals, Rao and Smakula have also found the same type of behaviour [4.17]. To explain the conductivity mechanism in Nickel oxide that existed either in non-stoichiometric or lithium doped) the authors stated that in NiO both Ni^{+3} and Ni^{+2} ions were produced to preserve the electrical neutrality. The simultaneous presence of Ni^{+3} and Ni^{+2} ions allows charge transfer from one ion to another. This charge transfer process required an activation energy similar to that in covalent semiconductors contrast to the situation in semiconductor. However, Morin [4.27], Heikes et al [4.28] and Housten [4.29] have explained the conduction process in NiO as being due to a thermally activated diffusion of holes trapped at Ni^{+3} ions rather than to a carrier production. Heikes et al assumed the activation energy required for the conduction process to consist of two parts: (i) the energy required to loosen the charge carrier from the parent atom (Ni^{+3}) i.e. the energy required for the production of charge carriers and, (ii) that necessary for the transfer of these charge carriers. Their calculation shows that when the impurity concentration is ~ 2% or more then all the charge carriers are free. At high concentration the authors connected the activation energy only with the mobility of the charge carriers.

Thus a thermally activated diffusion process leads to the increase in mobility of the charge carriers by contributing towards the conductivity. On the otherhand, Ksendzou et al [4.30] and Zhuze and Shebykh [4.31] showed for the same material (NiO) that the mobility decreases with temperature and concluded that the increase in conductivity with temperature was associated with the increase of the concentration of the charge carriers moving in a narrow band within the bandgap.

4.5 CONDUCTIVITY STUDIES

4.5.1 D.C. Conductivity

The d.c. conductivities of the three types of alumina were measured (by the two electrode techniques described in Chapter Two) over the temperature range 20°C to about 500°C. The data for single crystal Cr/Al_2O_3 is given as a plot of log $\sigma_{d.c.}$ against $\frac{1}{T}$ in Fig.4.15. There is a linear variation on the log plot up to about 500°C ; for this region the activation energy (ΔE), obtained from the expression

$$\sigma_T = \sigma_o e^{-\frac{\Delta E}{KT}} \qquad (4.5)$$

is about 0.8 eV. Above 500°C, the slope of the plot increases markedly giving a much higher value of activation energy of 2.48 eV for the second conduction process. The corresponding plot for pure polycrystalline alumina is given in Fig 4.16. Again, up to about 500°C the plot is linear, but the activation energy corresponds to 1.13 eV which is much larger than for the single crystal Cr/Al_2O_3. It is to be noted that the values of conductivity (e.g. about 3×10^{-13} Ω^{-1} cm^{-1} at 230°C) at a given temperature are very comparable for both materials. By contrast the results for the impure black alumina, Fig 4.17, show very much higher values of conductivity, e.g. 2×10^{-8} Ω^{-1} cm^{-1} at the same temperature of 230°C, an increase of some five orders of

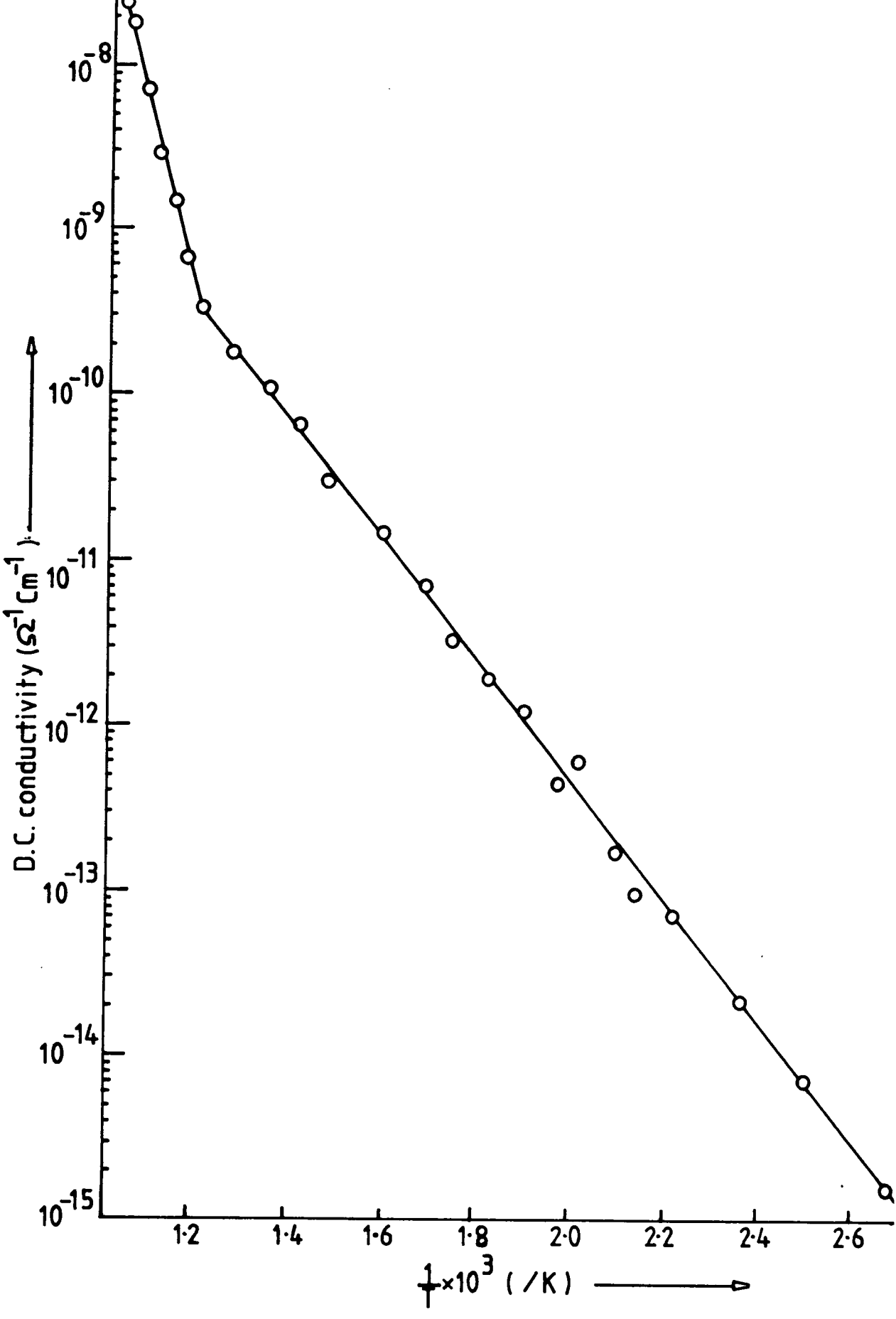

Fig. 4·15 D.C. conductivity vs. temperature data for Cr/Al_2O_3 single crystal.

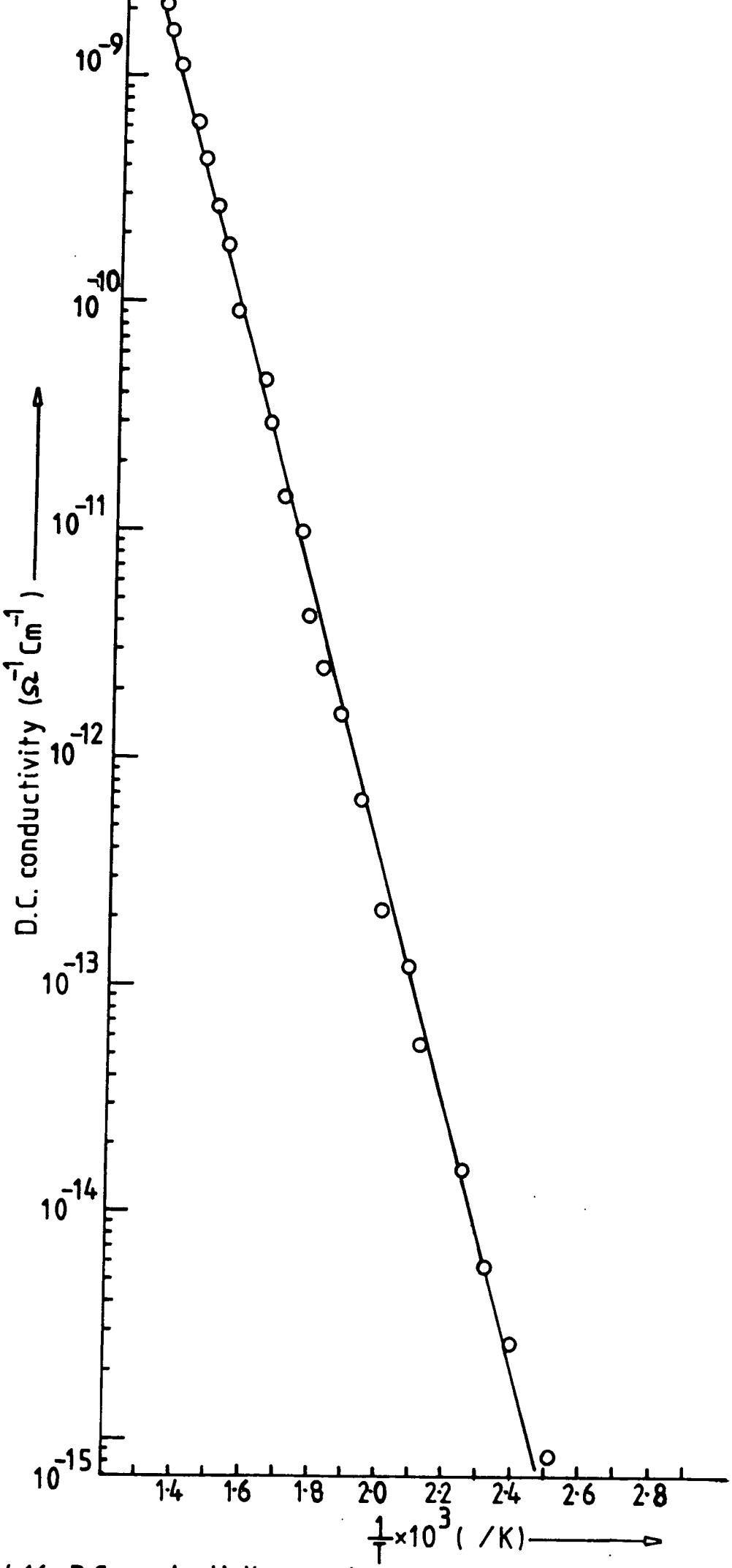

Fig. 4·16 D.C. conductivity vs. temperature data for pure polycrystalline alumina.

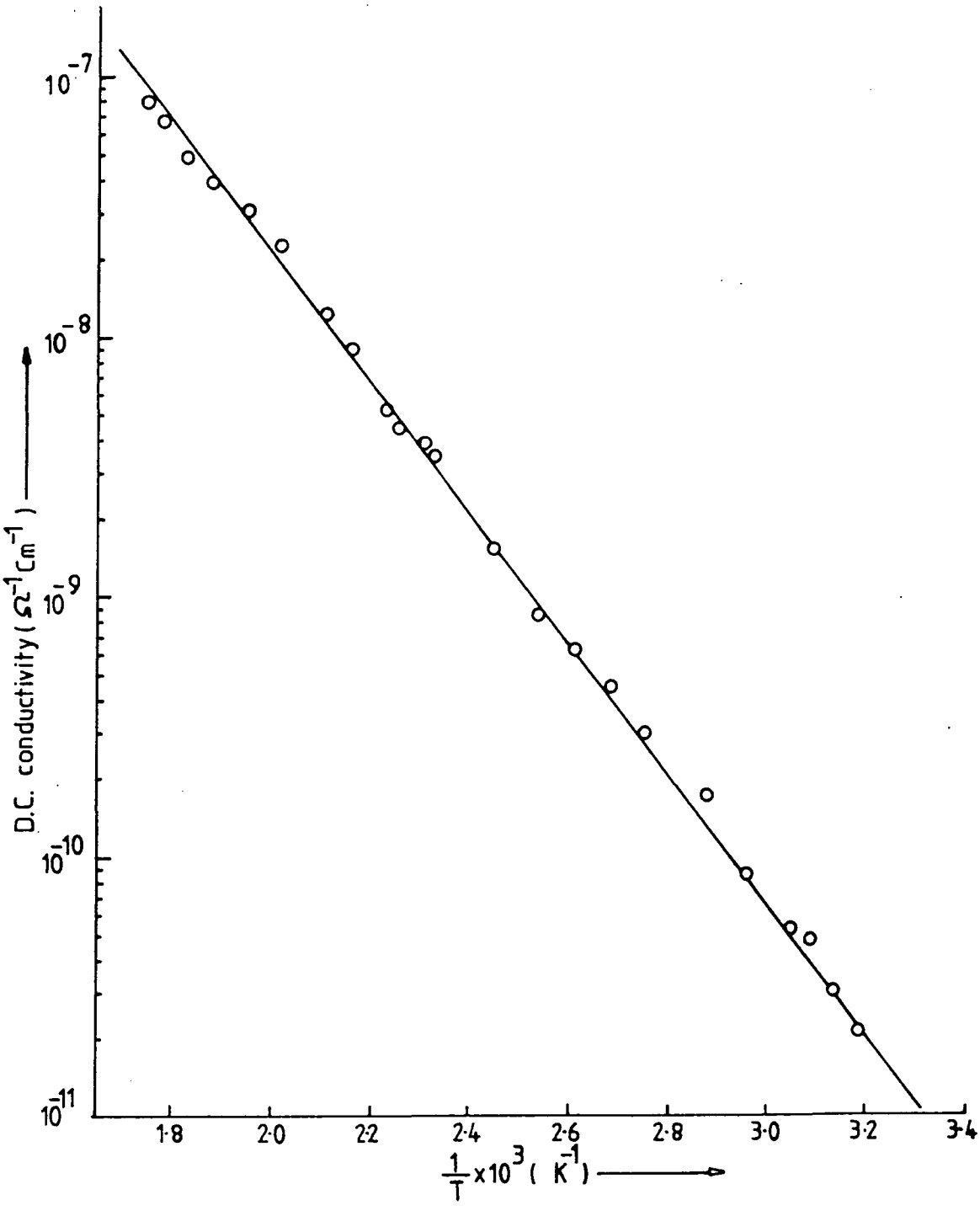

Fig. 4·17 D.C. conductivity vs. temperature data for black alumina.

magnitude. The log $\sigma_{d.c.}$ vs. $\frac{1}{T}$ plot is also linear over the temperature range examined but yields a lower activation energy of only $\Delta E = 0.50$ eV.

A recent discussion of d.c. and a.c. electrical conduction in single crystal alumina has been given by Kizilyalli and Mason [4.32]. These authors measured the conductivity in the C-direction of single crystal sapphire slices and flux grown platelets over a temperature range up to 1500°C at frequencies from 7×10^1 Hz to 5×10^6 Hz. For Czochralski grown high purity alumina the value of activation energy in the temperature range up to 500°C (deduced from Kitazawa and Coble's [4.33] data given in Fig.2 of reference (4.32) is $\Delta E = 1.17$ eV. For the flux grown platelets (Fig 1 of reference) the activation energy is rather lower, $\Delta E = 0.95$ eV. There is fairly close agreement between the present value of 1.1 eV for pure polycrystalline alumina and these literature values of between 0.95 and 1.1 eV for undoped alumina single crystals. It is noticeable that the present value for Cr/Al_2O_3 is less at 0.8 eV. The reduction in activation energy by the addition of a dopant seems to hold generally and Kizilyalli and Mason report similar reductions in activation energy for cobalt doped alumina. This trend is confirmed by the result for black alumina ; this material was known to contain impurity contents of 1% of each of iron, manganese and titanium and gave the much lower activation energy of 0.5 eV.

4.5.2 A.C. conductivity

The log $\sigma_{a.c.}$ vs $\frac{1}{T}$ plot for the Cr/Al_2O_3 single crystal is shown in Fig 4.18. At any particular frequency there is a marked curvature of the characteristics which only becomes linear for temperatures exceeding about 280°C. For temperatures above 280°C the data for different frequencies tends to converge giving activation energies of $\Delta E = 0.63$ eV at 5×10^2 Hz and $\Delta E = 0.5$ eV at 2×10^4 Hz. With pure polycrystalline alumina, Fig.4.19, the general behaviour is very

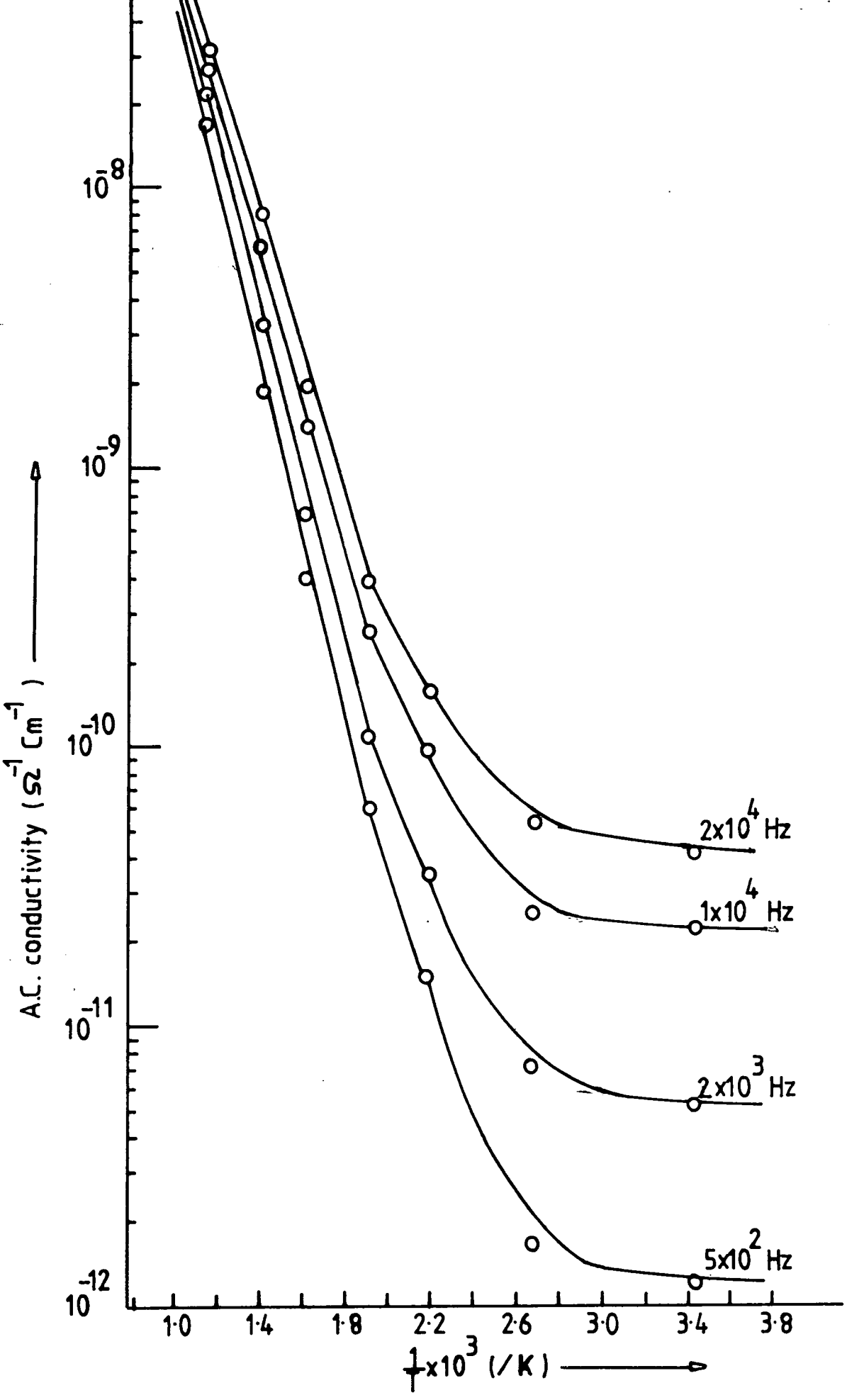

Fig. 4·18 A.C. conductivity vs. temperature data for Cr/Al_2O_3 single crystal.

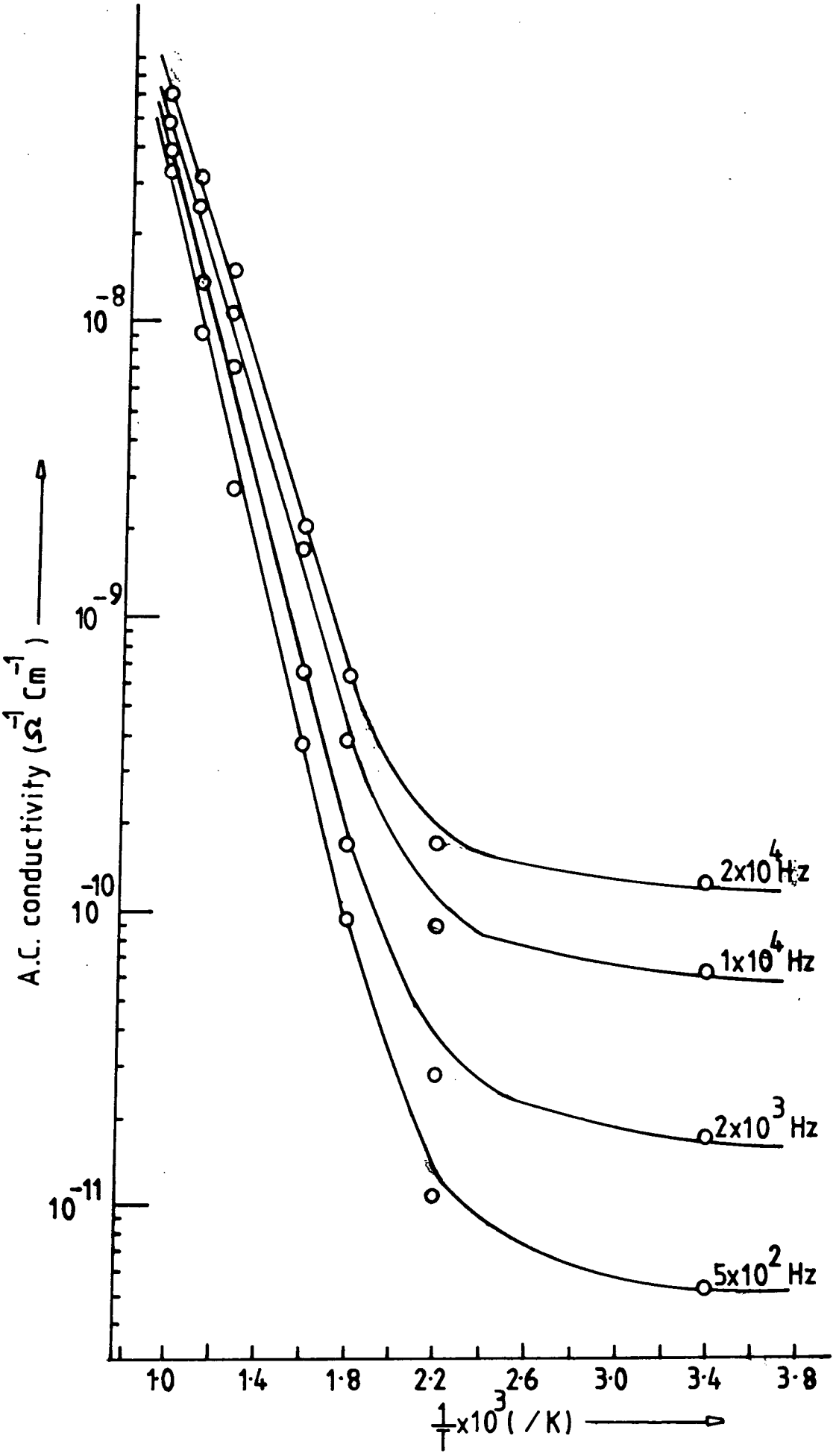

Fig. 4·19 Variation of a.c. conductivity with reciprocal temperature for pure polycrystalline alumina.

similar and this data yields values of ΔE = 0.8 eV at 5 x 10^2 Hz and ΔE = 0.75 eV at 2 x 10^4 Hz. These values may be compared with those reported by Govinda and Rao following their studies of the dielectric properties of single crystals of Al_2O_3 and Al_2O_3 doped with chromium or vanadium [4.8]. The temperature and frequency ranges, up to about 450° C and 10^7 Hz respectively, used by Govinda and RaO were very comparable to those used in the present work. For pure alumina single crystal they quoted a value of ΔE = 0.77 eV at 10^2 Hz which is very close to the value of 0.80 eV at 5 x 10^2 Hz found for pure polycrystalline alumina. Govinda and Rao also discussed the effect of the addition of a dopant on the activation energy and showed that the activation energy was reduced. Thus they reported that for Al_2O_3 containing 0.03% chromium ΔE = 0.69 eV at 10^2 Hz ; this may be compared with the value of ΔE = 0.63 eV at 5 x 10^2 Hz for the single crystal of Al_2O_3 containing 0.05 percent chromium examined here. These authors also stated that the further increase of dopant concentration caused some additional reduction in activation energy; the linear activation energy values for conduction in doped crystals were attributed to the larger charge carrier concentration in them as compared to undoped Al_2O_3.

The log $\sigma_{a.c.}$ vs $\frac{1}{T}$ plots for black alumina is shown in Fig.4.20. The absolute conductivity values are again very much larger than those for either the single crystal or the polycrystalline alumina being 6 x 10^{-8} (Ω^{-1} cm^{-1}) at 280°C and 5 x 10^2 Hz compared with 4 x 10^{-11} (Ω^{-1} cm^{-1}) for the pure materials. In the temperature range above 200°C the data for the individual frquencies again converges and gives a value of ΔE = 0.50 eV. This value is much less than those for either the pure alumina (ΔE = 0.8 eV) and the 0.05% Cr/Al_2O_3 (ΔE = 0.63 eV) as might be expected for the higher levels of impurity concentrations.

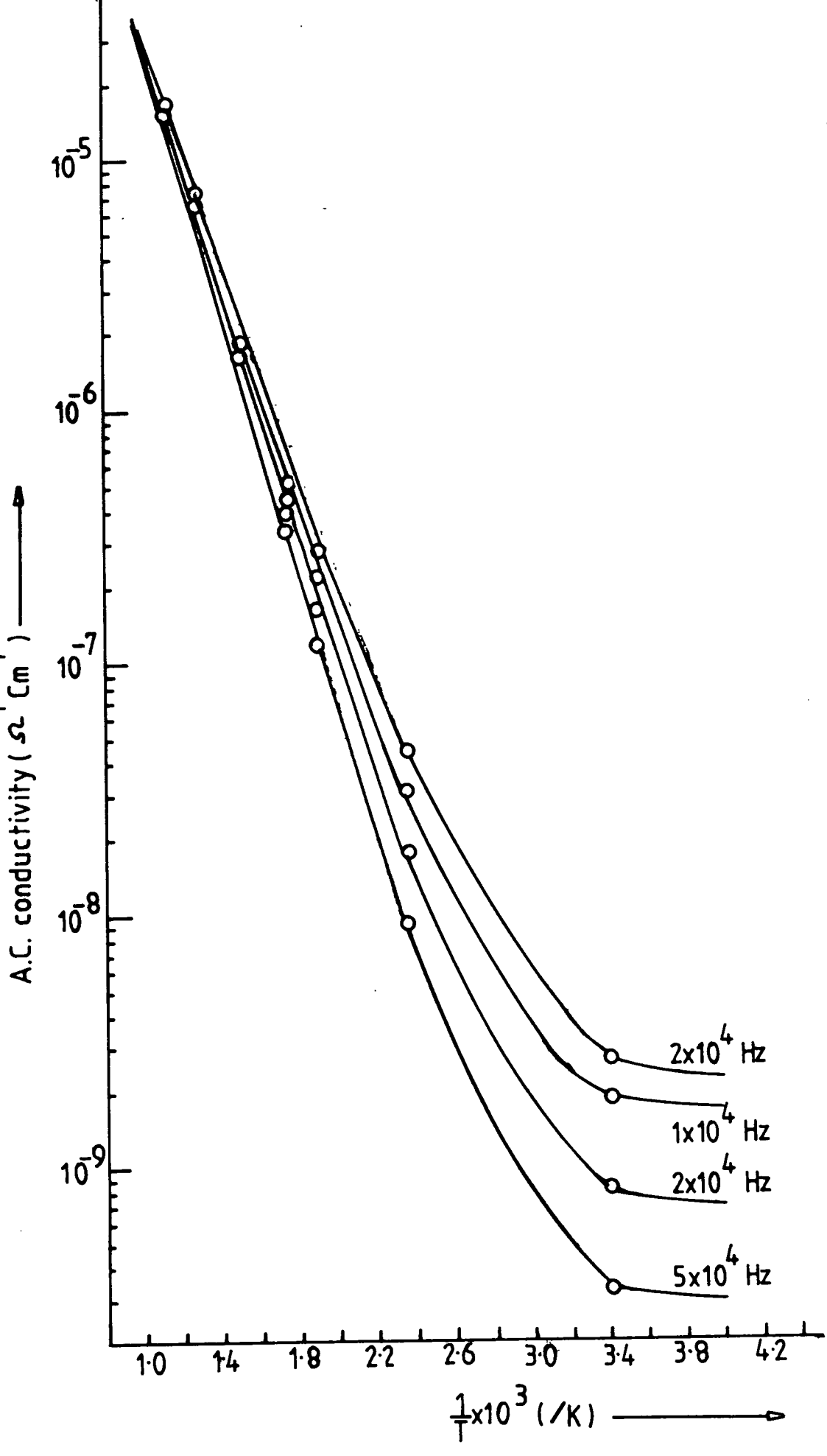

Fig. 4·20 A.C. conductivity vs. temperature data for black alumina.

CHAPTER FOUR

REFERENCES

4.1 H.Low, Phys.Rev., 105 (1957) 801.

4.2 F.Rosenberger, Fundamentals of Crystal Growth 1, Springer-Verlag, New York (1979), 395.

4.3 F.Jona, G.Shirane, Ferroelectric Crystals, Pergamon Press., London (1962), 108.

4.4 A.Von Hippel, 1954, Dielectric Materials and Applications, New York: John Wiley.

4.5 A.K.Chaudhury and K.V.Rao, Phys.Stat.Sol., 32 (1969) 731.

4.6 K.Lal and H.K.Jhans, J.Phys.C., 10 (1977) 1315.

4.7 J.Fontanella, C.Andeen and D.Schuele, J.of Appl.Phys., 45 (1974) 2852.

4.8 S.Govinda and K.V.Rao, Phys.Stat.Sol.(a), 27 (1975) 639.

4.9 E.V.Loewenstein, D.R.Smith, and R.L.Morgan, Appl.Opt.12 (1973) 398.

4.10 E.E.Russell and E.E.Bell., J.Opt.Soc.Am.57 (1967) 341.

4.11 S.Roberts and D.D.Coon, J.Opt.Soc.Am. 52 (1962) 1023.

4.12 A.K.Jonscher, Nature, 267 (1977) 673.

4.13 A.K.Jonscher, Nature, 253 (1975) 717.

4.14 J.S.Thorp and N.E.Rad, J.Mat.Sci., 16 (1981) 255.

4.15 J.S.Thorp, A.B.Ahmad, B.L.J.Kulesza, T.G.Bushell, J.Mat.Sci., 19 (1984) 3680.

4.16 S.V.J.Kenmuir, J.S.Thorp and B.L.J.Kulesza, J.Mat.Sci., 18 (1983) 1725.

4.17 K.V.Rao and A.Smakula, J.of Appl.Phys., 36 (1965) 2031.

4.18 F.L.Weichman, Can.J.Phys., 51 (1973) 680.

4.19 C. Noguet, 1969, These,Universite de Strasbourg, Strasbourg, France.

4.20 R.S.Bever and Robert L.Sproull, Phys.Rev., 83 (1951) 801.

4.21 A.J.Bosman and E.E.Havinga, Phys.Rev., 129 (1963) 1593.

4.22 J.Link, Mary C.Wintersgill, J.J.Fontanella, V.E.Bean, C.G.Andeen, J.of Appl.Phys., 52 (1981) 936.

4.23 J.Thorp, N.E.Rad, D.Evans, C.D.H.Williams, J.of Mat.Sci., 21 (1986) 3091.

4.24 A.K.Jonscher, "Dielectric Relaxation in Solids" (Chelsea Dielectric Press, London (1983)).

4.25 L.A.Dissado and R.M.Hill, Faraday Trans., 2 (80) (1984) 291.

4.26 R.Fuchs, Tech.Rept.167, Lab.Ins.Res.MIT (Nov.1961).

4.27 F.J.Morin, Phys.Rev., 93 (1954) 1199.

4.28 R.R.Heikes and W.D.Johnston, J.Chem.Phys., 26 (1957) 582.

4.29 S.Van Housten, J.Phys.Chem.Solids, 17 (1960), 7.

4.30 Ya.M.Kzendzov, L.N.Ansel'm, L.L.Vasil'eva, and V.M.Latysheva, Soviet Phys., Solid State, 5 (1963) 1537.

4.31 V.P.Zhuze and A.I.Shebjkh, Soviet Phys., Solid State, 5 (1963), 1756.

4.32 H.M.Kizilyalli and P.R.Mason, Phys.Stat.Sol.(a) 36 (1976) 499.

4.33 K.Kitazawa and R.L.Coble, J.Amer.Ceram.Soc. 57 (1974) 246.

CHAPTER FIVE

DIELECTRIC STUDIES ON ALUMINIUM NITRIDE

The samples examined in this work were all obtained from outside sources as commercially available substrate grade material. One was from a Japanese manufacturer (Tokoyama, SODA.Co) whose material appeared white and was provided as thin sheets of polycrystalline texture. This will be referred to as material "W". The other came from a European manufacturer (Heraeus). The primary use of their material was for crucibles for handling molten metals and consequently the purity of the material had not been specifically controlled for substrate application ; the samples appeared black in colour and were also provided as thin polycrystalline sheets. These will be referred to as material "B".

5.1 STRUCTURAL AND CHEMICAL CHARACTERIZATION

The samples were first examined by SEM in order to ascertain the general features and grain size of the two materials. The results are shown in Fig 5.1a and 5.1b. For the white material the grain size is between 4 μm and 6 μm and there appeared to be some much smaller grains (about 1/4 μm in diameter) randomly dispersed throughout the material. By contrast the black material, Fig 5.1b reveals a much coarser texture, many grains being as large as about 12 μm. In addition there is evidence for quite large (2 μm to 10 μm) flakes of different material but there is a markedly smaller density of the small grains present in Fig 5.1a. Corresponding RHEED patterns were also obtained and these are shown in Fig 5.2a and 5.2b which refer to white and black aluminium nitride respectively. The large grain-size of both materials is emphasised by the very spotty nature of the diffraction rings, a fact which made analysis of the photographs difficult. This analysis for d-values was, however, attempted and the results are tabulated in Table 5.1. The d-values obtained for both the samples

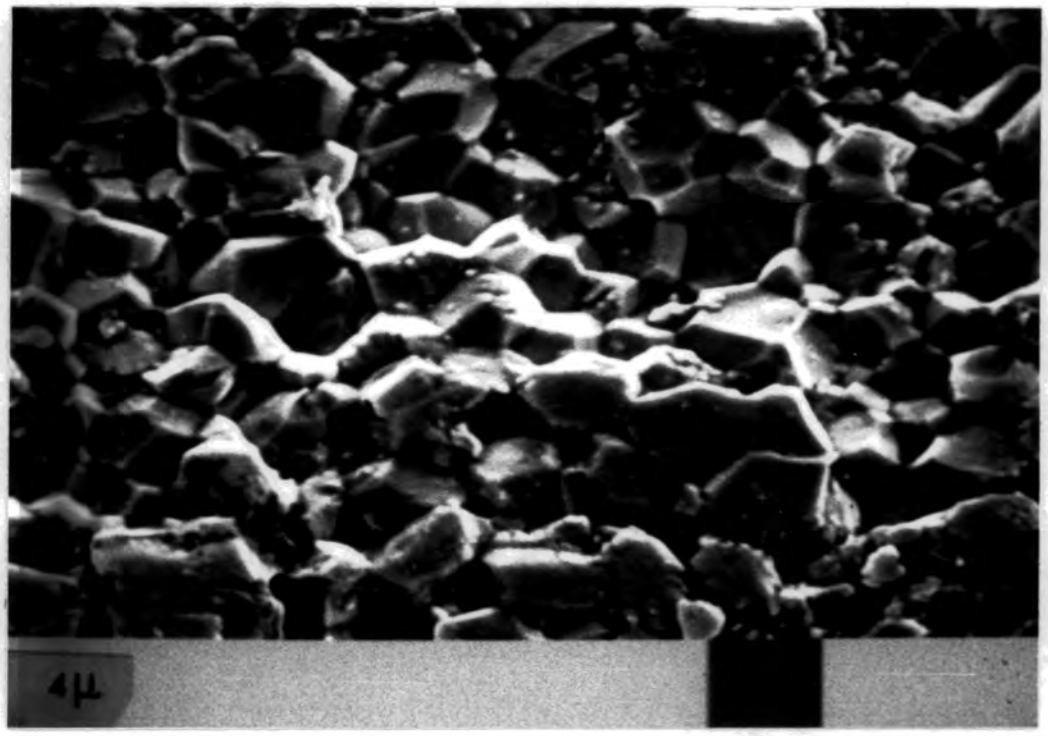

FIG 5.1(a): A typical SEM micrograph for pure polycrystalline aluminium nitride (W)

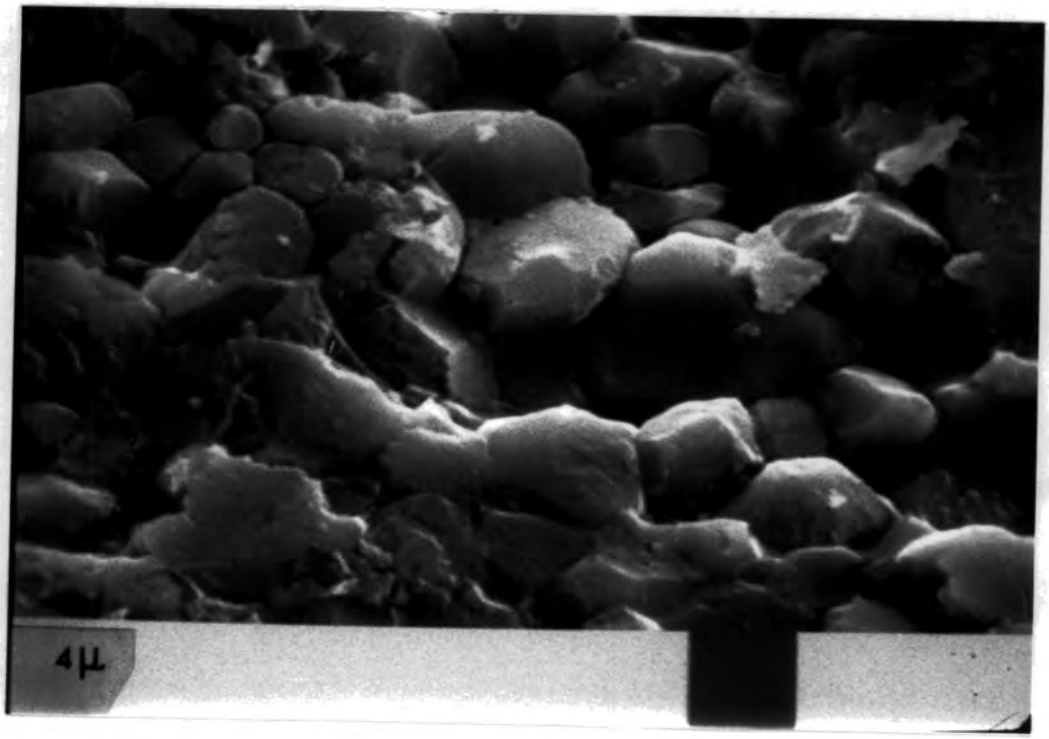

FIG 5.1(b): A typical SEM micrograph for black aluminium nitride (B)

TABLE 5.1: Comparison of d-values for White and Black Aluminium Nitride obtained from Experimental Electron Diffraction Pattern with Reference Data for Aluminium Nitride (8-262).

ASTM index (8-262) for AlN			Experimental value obtained from RHEED for pure AlN	Experimental value obtained from RHEED for impure AlN	
					Extra lines observed
d (Å)	I/I_1	hkl	d_{hkl} (Å)	d_{hkl} (Å)	(Å)
2.70	100	100	2.829	3.01	
2.49	60	002	2.51	2.565	
2.372	70	101	2.064	2.274	
					2.078
1.829	21	102	1.93	1.722	
1.557	30	110	1.62	1.607	
					1.452
1.414	21	103	1.395	1.435	
1.348	5	200		1.385	
1.320	17	112	1.339	1.31	
1.301	7	201		2.269	
1.248	1-2		1.23	1.23	
1.186	4	202	1.09	1.18	
					1.137
1.047	6	203	1.057	1.076	
1.019	3	210	1.039	1.039	
0.9984	5	211	0.972	0.988	
0.9345	5	105	0.927	0.913	
0.8684	6	213	0.873	0.89	

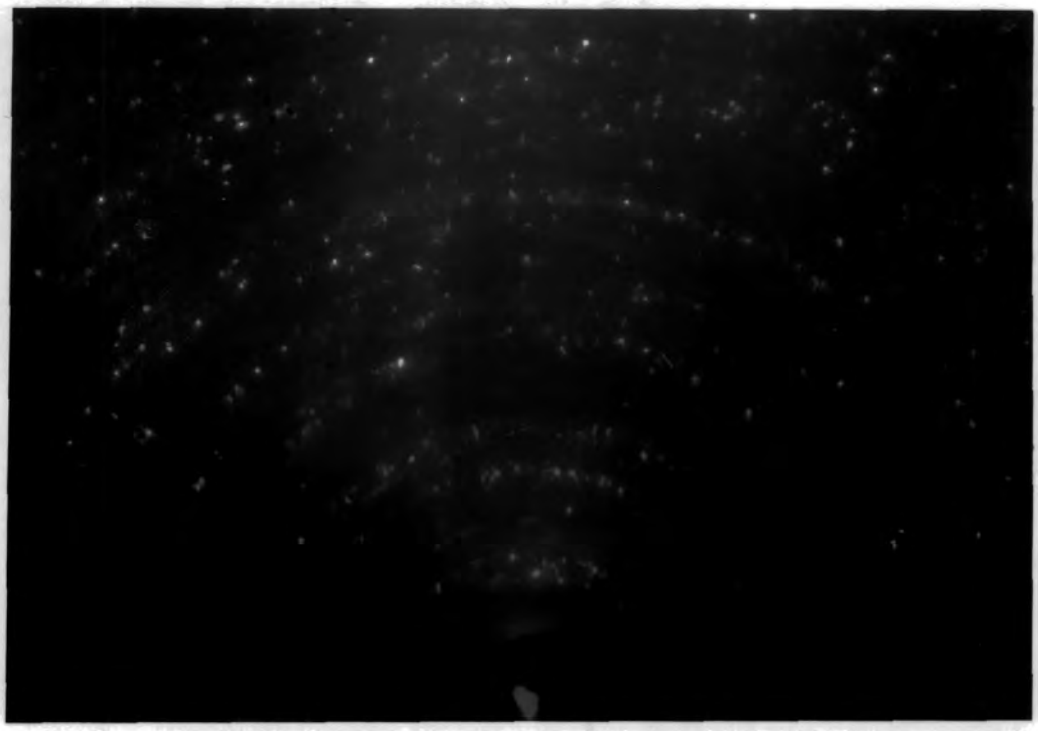

FIG 5.2(a): A typical RHEED pattern for pure polycrystalline aluminium nitride (W)

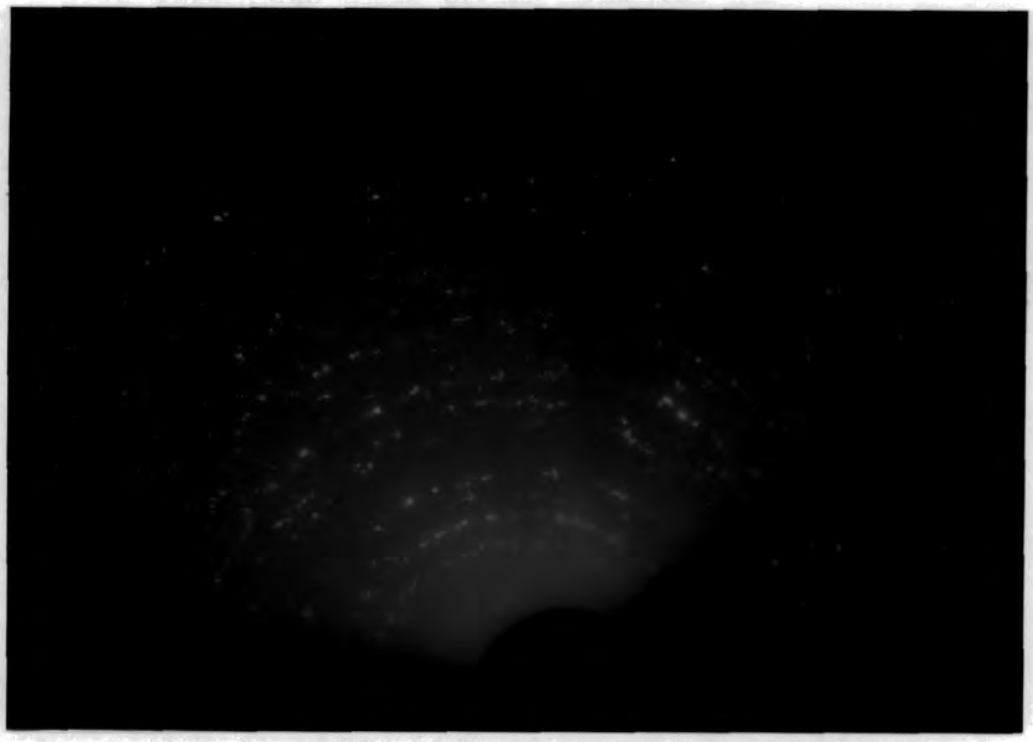

FIG 5.2(b): A typical RHEED pattern for black aluminium nitride (B)

show a fair fit with the reference data for aluminium nitride (ASTM index 8-262). For pure aluminium nitride, all the lines observed can be accounted for by the lines in ASTM listing. However in the impure aluminium nitride sample extra lines were observed at d-values of 2.078, 1.452 and 1.137 A. However, the analysis is not sufficiently exact to provide conclusive evidence for the nature of the impurity in black aluminium nitride. Hence, further measures were evidently needed in order to establish the nature of the impurity. So that its likely influence on the dielectric behaviour could be assessed.

Some complementary appraisal studies have been reported by M.Al-Naief [5.1] some of whose results are quoted here. X-ray diffractometer analysis of the same two samples was undertaken and the data is shown in Table 5.2. Again it can be seen that for the pure material (AlN (W)) all the lines observed agree in d-value quite closely with the ASTM data and that there is no evidence for extra lines. Thus it is reasonably certain both from electron diffraction and X-ray diffraction data that the white aluminium nitride sample is pure. By contrast the XRD data for the black sample (AlN (B)) does show four clearly identifiable additional lines in the diffractometer spectrum ; these occur at d-values of 1.241, 0.970, 0.912, 0.896 Å respectively. This sample was the starting powder from which the substrate material AlN(B) was made. X-ray fluorescent analysis was also undertaken and these results are given in Table 5.3. Here the samples labelled $AlN(B_2)$ and $AlN(B_3)$ are two specimens of polycrystalline sintered substrate material made from the same starting powder $AlN(B_1)$, which was itself a dark-grey powder. The results show that the major impurities are iron, titanium and chromium. Al-Naief also attempted an independent identification of the impurities by utilizing magnetic methods for measuring the magnetic susceptibility and the Curie temperature of the black aluminium nitride. The

A.S.T.M. data*		AlN(W		AlN(B1)	
dA^0	hkl	dA^0	hkl	dA^0	hkl
2.70	100	2.693	100	2.685	100
2.49	002	2.483	002	2.475	100
2.372	101	2.366	101	2.354	101
1.829	102	1.827	102	1.826	102
1.557	110	1.552	110	1.553	110
1.414	103	1.413	103	1.411	103
1.348	200	1.342	200	1.343	200
1.320	112	1.319	112	1.318	112
1.301	201	1.301	201	1.298	201
-	-	-	-	1.2410	impurity
1.186	202	1.183	202	1.181	202
1.047	203	1.044	203	1.046	203
1.019	210	1.018	210	1.016	210
0.997	211	0.997	211	0.997	211
-	-	-	-	0.970	impurity
0.941	212	0.9414	212	0.9414	212
0.934	105	0.932	105	0.930	105
-	-	-	-	0.9128	impurity
-	-	-	-	0.8969	impurity
0.868	213	0.888	213	0.887	213

TABLE 5.2: **X-ray diffractometer analysis of AlN samples**

**American Society for Testing Material*

Impurity	AlN(W.	AlN(B2)	AlN(B3)	AlN(B1)
Fe	30	2600	1400	2000
Si	–	210	40	600
Cr	200	79	107	–
Zn	–	600	–	140
Ti	600	330	200	–
Ca	300	–	–	–

TABLE 5.3: **X-ray fluorescent analysis of AlN samples (in ppm)**

measurements were made by using modified Gouy balance techniques. The variation of force with the square of the magnetic field is reproduced in Fig 5.3. It is to be noted that if the material were a true paramagnetic the plot should be linear ; however the plot observed is distinctly non-linear, i.e. it displays the characteristics to be expected from a ferro-magnetic material, whose magnetization is approaching saturation at high values of magnetic field. A determination of the Curie temperature was also made by observing the change in magnetic force as the temperature of the sample was raised ; this is shown in Fig 5.4. Extrapolation from the region of maximum slope gives a Curie temperature of (780 $\pm$ 10°C) which is in very close agreement with the value of 770°C reported by Bozorth [5.2].

A comparison of the d-values of the additional lines observed in both the electron diffraction and x-ray diffraction photographs of the black aluminium nitride was made with the ASTM data for α-iron, α-Fe_2O_3 and FeO. This is shown in Table 5.4. It can be seen that there is fair agreement between the additional lines and those of both α-iron and α-Fe_2O_3. The diffraction data by itself is insufficient to resolve identification further, but the Curie temperature information makes α-iron more likely. Because both samples were in the form of sintered ceramics it was necessary to be able to estimate their porosity. This was done by measuring the density of samples of known shape and volume and the porosities were derived as the ratio of the measured density to the theoretical density, taken as 3.26 gm/c.c. The packing fractions were 0.94 for AlN (W) and 0.93 for AlN (B).

5.2 ROOM TEMPERATURE DATA

The room temperature variations of permittivity and dielectric loss with frequency are shown in Figs 5.5 and 5.6 respectively. Over the frequency range 5 x 10^2 to 10^7Hz, the permittivities are almost entirely frequency independent. Comparison first between pure AlN and

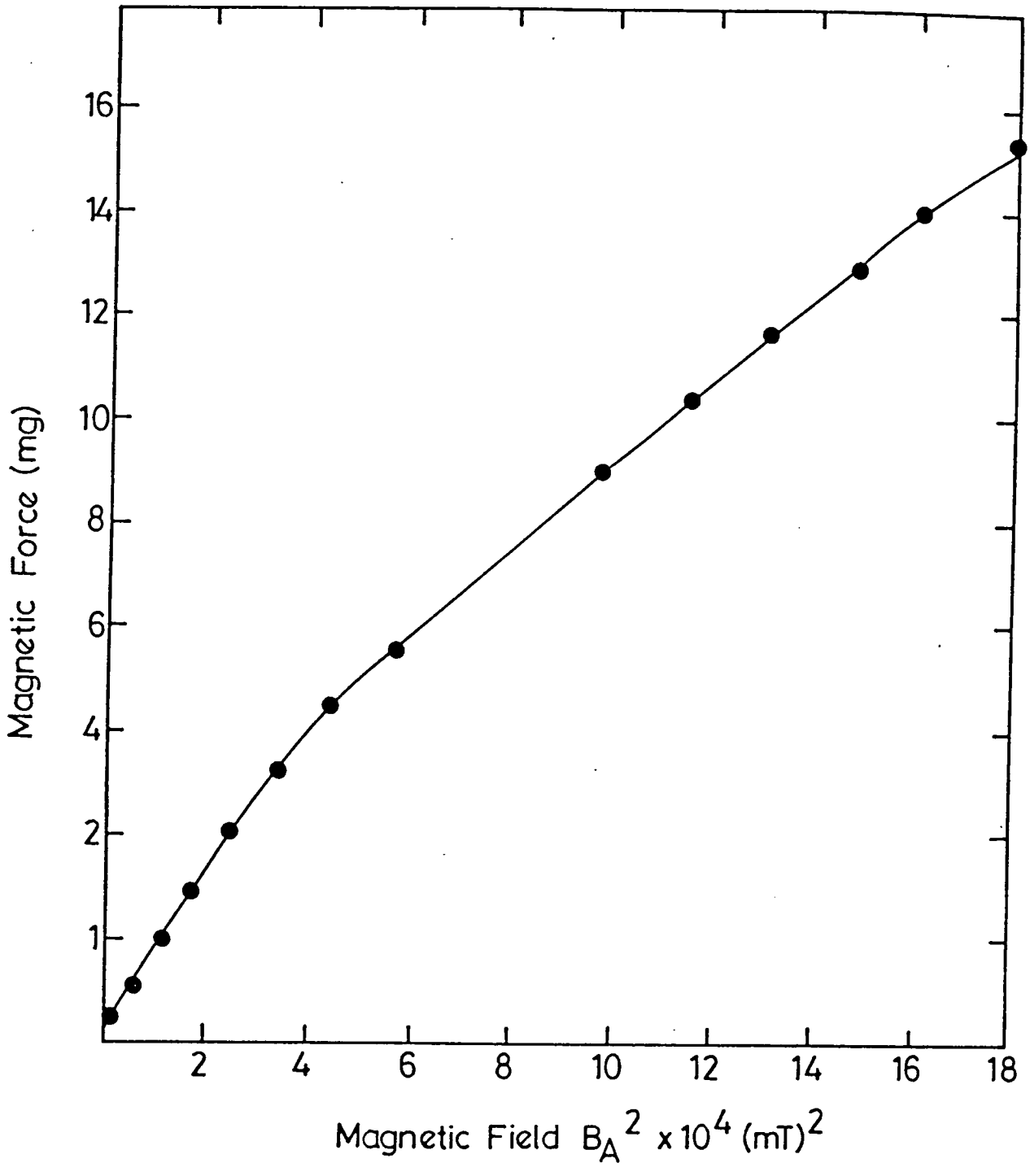

Fig. 5.3: , Force-(Magnetic Field)^2 variation for AlN (B1)

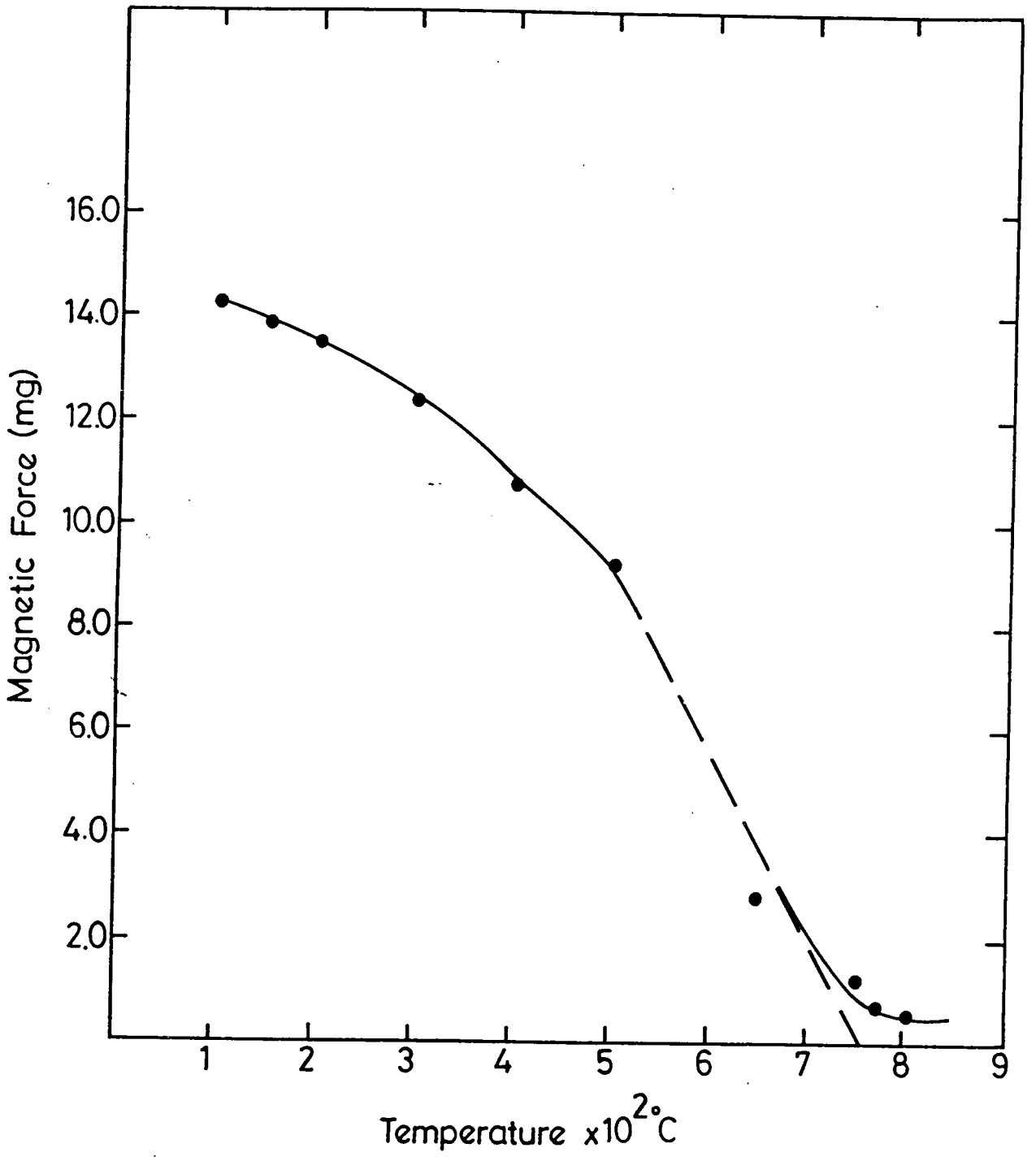

Fig. 5.4: Force-temperature variation for AlN (B1) Sample.

Additional lines	Hematite α-Fe_2O_3 (13-534).			Kamatite Iron(-phase) (6-0696)			Wustite Iron(11),FeO (6-0615)		
	d Å	I/I_1	hkl	d Å	I/I_1	hkl	d Å	I/I_1	hkl
2.57*	2.69) 2.51)	100 50	104 110				2.486	80	111
2.078	2.070	2	202	2.0268	100	110	2.153	100	200
1.452	1.452	35	300	1.4322	20	200	1.523	60	220
1.241	1.258) 1.226)	8) 2)	220) 036)	1.1702	30	211	1.299) 1.243)	25) 15)	311) 222)
1.137	1.141	12	134				1.077	15	400
0.97	0.9715	2	229	1.0134	10	220	0.988) 0.9631)	10) 15)	331) 420)
0.91) 0.896)	0.9080	25	1310	0.9064 0.8275	12 6	310 222			

TABLE 5.4: Comparison of d-values of additional lines in black AlN spectrum with ASTM data; (* 2.57 Å line is also common to AlN spectrum)

pure Al_2O_3, Fig 5.5a shows that $\epsilon'_s = 9.2$ at 1×10^3 Hz which is rather smaller than the value of $\epsilon'_s = 10.2$ at 1×10^3 Hz for the pure Al_2O_3. Next, comparing the pure and black AlN, Fig 5.5b shows that the permittivity of the black material is higher than that of the pure material, the difference being noticeably larger at the low frequency end of the range than the higher end; as will be mentioned later this behaviour would be consistent with the presence of high permittivity impurities such as iron. As regards the dielectric loss it is also found, Fig 5.6a that the log plot of ϵ''_s against frequency is linear for the pure polycrystalline AlN just as had previously been found for pure polycrystalline Al_2O_3, the loss is almost independent of frequency, though it is rather higher $\epsilon''_s = 2.0 \times 10^{-2}$ at 1×10^3 Hz than the corresponding value of $\epsilon''_s = 1.5 \times 10^{-2}$ for pure polycrystalline alumina. Thus for the pure AlN the tanδ value is about 2.17×10^{-3} over this frequency range which compares quite favourably with the value of 1.47×10^{-3} for pure polycrystalline alumina. The effect of the impurities present in the black aluminium nitride is much more evident in the ϵ''_s vs frequency variation, Fig 5.6b which shows a progressive and large rise in loss as the frequency is reduced below about 10^5 Hz. Above 10^5 Hz ϵ''_s for the black AlN is about 4×10^{-2} which is about two times greater than the value of 1.8×10^{-2} for pure AlN. Below 10^5 Hz the ratio ϵ"black/ϵ" pure increases rapidly to 3.4 at 10^4 Hz, 9 at 10^3 Hz and as much as 13.5 at 5×10^2 Hz. This is typical of increased polarization due to defects which is most pronounced at low frequencies.

For the pure AlN, it is reasonable to take the frequency independence of both ϵ'_s and ϵ''_s as indicative of the applicability of the Universal law. Fitting this data to the expression

$$(\epsilon'_s - \epsilon_\infty) \propto \omega^{n-1}$$

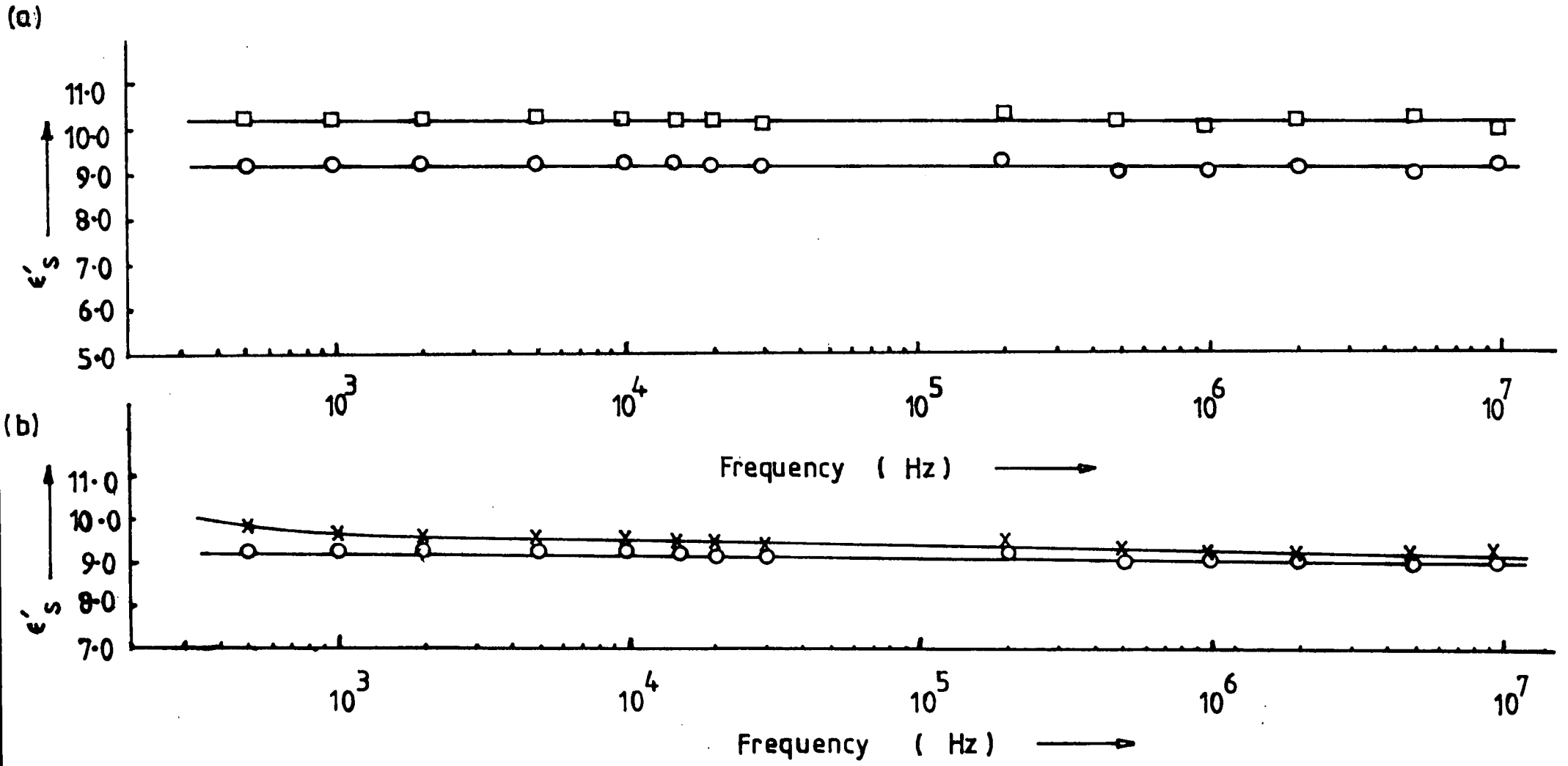

Fig. 5·5 Comparison of permittivity vs. frequency variations for (a) pure polycrystalline AlN (○) and pure polycrystalline Al_2O_3 (□), and (b) pure polycrystalline AlN (○) and black polycrystalline AlN (x).

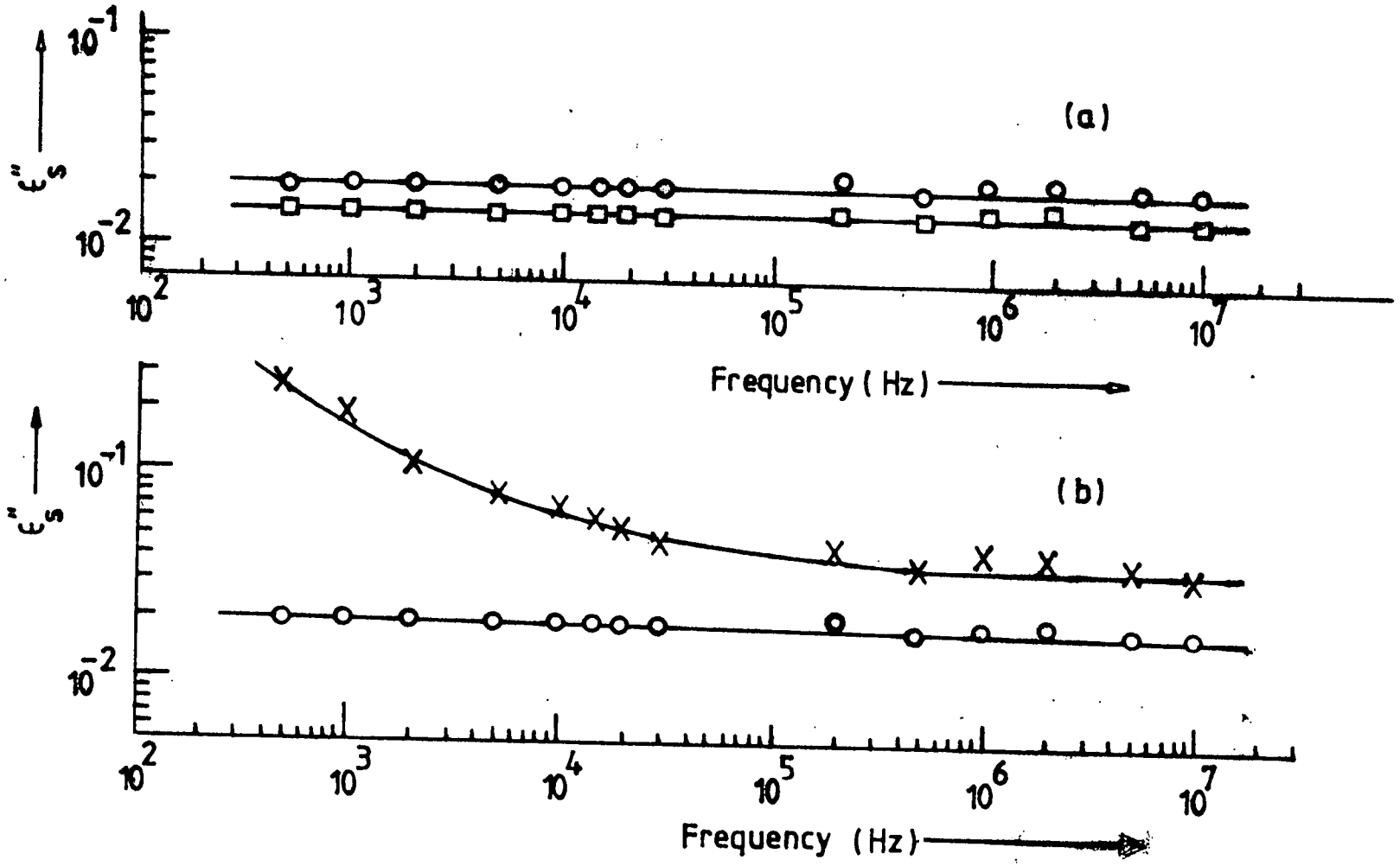

Fig. 5·6 Comparison of dielectric loss vs. frequency variations for (a) pure polycrystalline AlN (o) and pure polycrystalline Al_2O_3 (□) and (b) pure polycrystalline AlN (o) and black polycrystalline AlN (x).

and $\epsilon''_s \propto \omega^{n-1}$

gives values of the exponent n of 0.97 ± 0.03 (for pure AlN) from the permittivity-frequency variation and 0.96 ± 0.04 from the dielectric loss-frequency variation. These two numbers are equal within experimental error as would be expected if the law applied. Thus the present dielectric data indicates that pure AlN can also be regarded as a hopping conductor with dielectric properties very similar to those of alumina.

There are some reports in the literature of the dielectric properties of both single crystal and thin film aluminium nitride. Single crystals of aluminium nitride have been grown for some years by methods which mostly involve subliming AlN in pure nitrogen atmosphere at temperature approaching 2,000°C [5.3-5.4]. These crystals have been sufficiently large and well formed to enable the habit and crystallographic characteristics, including the lattice parameters [5.5] to be determined but since they mostly had dimensions not exceeding a few millimeters were not suitable for conventional, a.c. bridge dielectric measurement techniques. However, Collins, Lightowlers and Dean [5.6] observed the lattice vibration spectra of single crystal aluminium nitride by recording the optical reflectivity and transmission spectra in the wavelength range 2 to 30 μm. From these measurements they found that the optical refractive index was 2.2 and quoted a value of ϵ' (assuming the high frequency permittivity ϵ_∞ to be the square of the refractive index measured in the visible) of $\epsilon_\infty = 4.84$. They deduced a value of the low frequency permittivity of $\epsilon' = 9.14$, which agreed well their value of 9.1 calculated from the optical reflectivity data. As can be seen from the Fig 5.5, the low frequency value found from the bridge measurement was $\epsilon'_s = 9.2$ which is in very close agreement with the optical data. A comparison with data on aluminium nitride film can also be made using one of the recent

papers published by Chu and Kelm [5.7]. These authors measured the dielectric properties of aluminium nitride films by making capacitance measurement using a bridge operating at frequencies up to 5 x 10^5 Hz. For films prepared at temperatures between 800°C and 1,000°C ϵ' was found to be 11.5, whereas for films prepared at the higher temperature of 1,100°C the permittivity was considerably lower being about 8.1; Chu and Kelm also reported that ϵ' was independent of frequencies up to 5 x 10^5 Hz but gave no data on dielectric loss.

There is little information in the published literature about the value of permittivity and dielectric loss at higher frequencies, in particular in the microwave region. The low frequency data presented here suggests fairly convincingly that the Universal law applies. On this basis, the log ($\epsilon'_s - \epsilon_\infty$) versus frequency plot can be extrapolated and this yields a predicted value of 8.8 $\pm$ 0.1 at 10^{10} Hz for pure polycrystalline aluminium nitride. This agrees well with that obtained by Taylor and Lenie, who reported that for hot-pressed aluminium nitride which was about 96% pure and whose density was 98% of theoretical ϵ' = 8.5 also at the frequency of 10^{10} Hz. This agreement suggests that the Universal law behaviour does hold for frequencies up to the microwave region. If, however, the extrapolation were to be taken further the predicted value at optical frequencies would be about 8.5 which is clearly very much in excess of the figure of 4.84 deduced from the optical refractive index ; it appears therefore that there are likely to be some electronic resonances between the microwave and optical regions.

5.3 THE TEMPERATURE DEPENDENCE OF PERMITTIVITY

Measurements of permittivity as a function of temperature were made in two regions, the first using a furnace covering the temperature range 20°C to 350°C and the second a cryostat operating between -188°C to 20°C. The results are shown in Figures 5.7, 5.8 and 5.9. The data

for pure aluminium nitride in the upper temperature region, is given in Fig 5.7. Between room temperature and about 150°C, there is a small linear increase of ϵ'_s with temperature and it is noticeable that the data for all the different frequencies, i.e. 5×10^2 Hz to 2×10^4 Hz fall within very close limit. Above 150°C, ϵ'_s begins to increase rapidly giving very non-linear behaviour ; it is noticeable that the rate of change, $\left(\frac{\partial \epsilon'}{\partial T}\right)_p$ increases progressively as temperature increases and that at a given temperature $\left(\frac{\partial \epsilon'}{\partial T}\right)_p$ is greater for the lower frequency than for higher ones. It is also noticeable that the point at which the change from linear to non-linear behaviour occurs varies with frequency ; thus for 5×10^2 Hz the changeover occurs near 160°C whereas at 2×10^4 Hz, the plot remains linear until nearly 230°C. The corresponding data for the black aluminium nitride is shown in Fig 5.8. This displays the same general features, but it is clear that the linear regions (if this indeed exists at all) are much reduced in extent, certainly corresponding to temperature 120°C. The manner in which $\left(\frac{\partial \epsilon'}{\partial T}\right)_p$ depends on frequency is the same as for the pure aluminium nitride, i.e. it is greatest for the lowest frequency. The low temperature data which covers the range from room temperature down to -188°C is shown in Fig 5.9 which gives the results for pure and impure specimens. The graphs show that both variations are now sensibly linear and that there is no frequency dependence.

Analysis of the data in the linear range, i.e. for temperatures ranging from -188°C to about 180°C has been undertaken on the basis of the Bosman and Havinga's model [5.8]. The values of the coefficient $\{(\epsilon'-1)(\epsilon'+2)\}^{-1} \left(\frac{\partial \epsilon'}{\partial T}\right)_p$ so derived are given in Table 5.5, which also includes some data deduced from Xinjao et al published results on thin film aluminium nitride. For the pure aluminium nitride the average value of the coefficient over the temperature -188°C to + 180°C is about $1.05 \times 10^{-5}\ k^{-1}$. For the impure sample the value below room

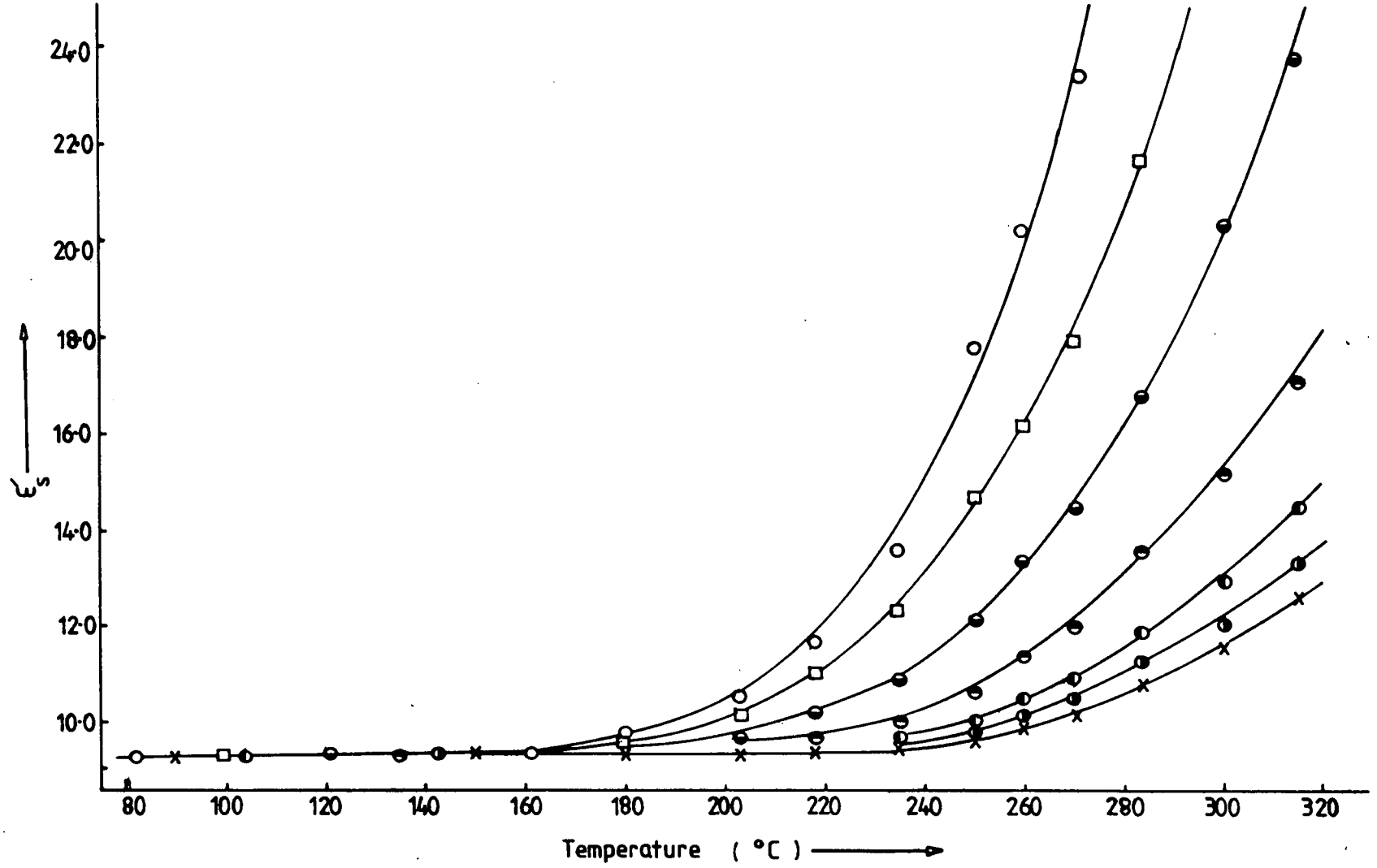

Fig. 5·7 Temperature variation of ε'_s for pure polycrystalline AlN ; high temperature range. Key: 5×10^{2} Hz(○), 1×10^{3} Hz(□), 2×10^{3} Hz(⊖), 5×10^{3} Hz(●), 1×10^{4} Hz(◐), $1{\cdot}5\times10^{4}$ Hz(◑), 2×10^{4} Hz (x).

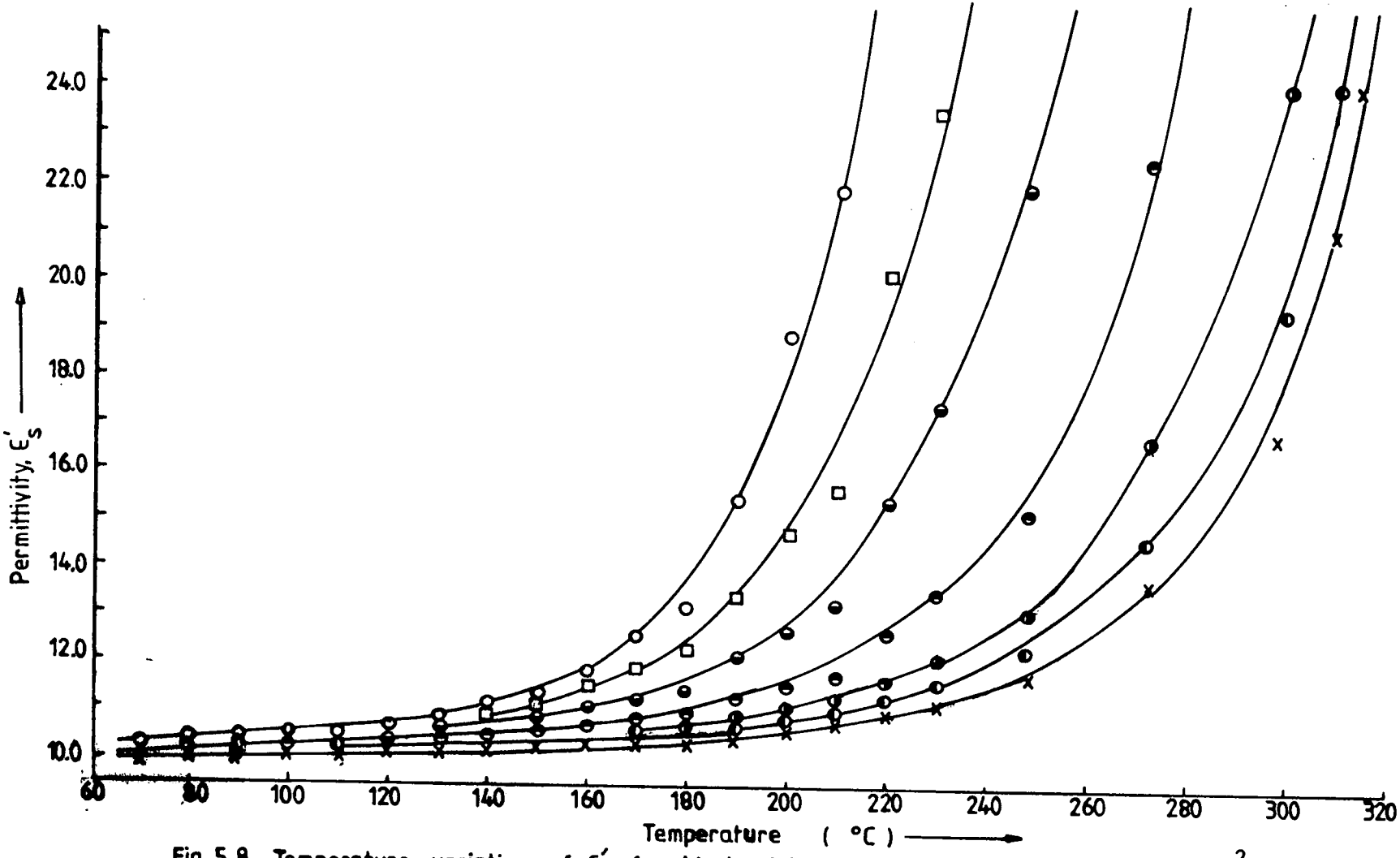

Fig. 5.8 Temperature variation of ϵ'_s for black AlN; high temperature range. Key: 5×10^2 Hz (○), 1×10^3 Hz (□), 2×10^3 Hz (●), 5×10^3 Hz (●), 1×10^4 Hz (●), 1.5×10^4 Hz (●), 2×10^4 Hz (x).

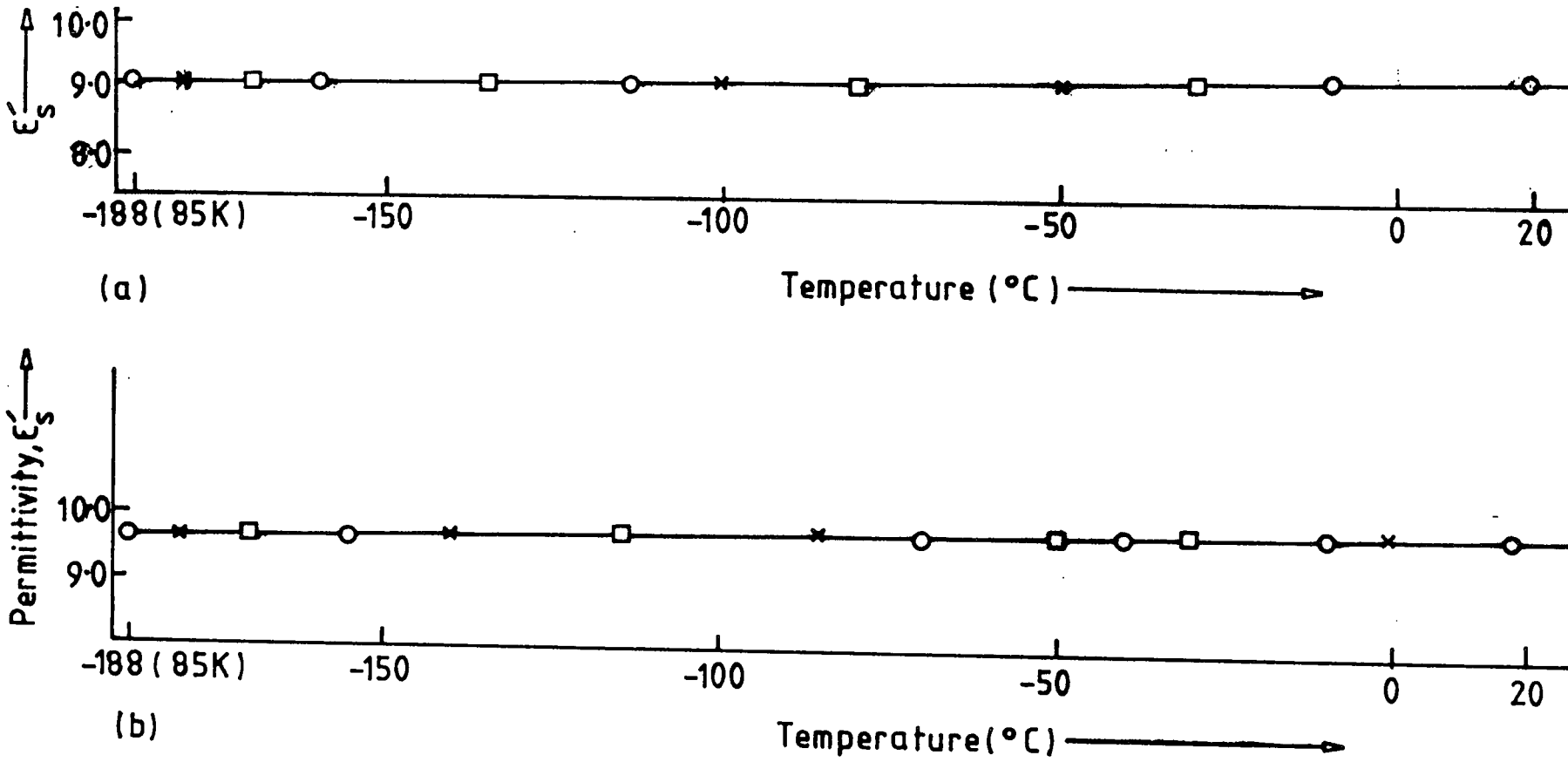

Fig. 5·9 Temperature variation of permittivity for (a) pure polycrystalline aluminium-nitride and (b) black aluminium nitride ; low temperature region. Key : 1×10^3 Hz(o 1×10^4 Hz (□) and 2×10^4 Hz (×).

TABLE 5.5: Temperature Coefficients of Permittivity for Aluminium Nitride.

Temperature dependencies of the permittivity of Al_2O_3 and AlN ceramics at constant pressure (at high temperature region).

Sample	Frequency (in KHz)	ϵ' at room temp.	Temp.range (°C)	$\frac{1}{(\epsilon'-1)(\epsilon'+2)}\left(\frac{\partial\epsilon'}{\partial T}\right)_p$ (/K)	Refs.
AlN (white)	1.0	9.2	20-180	1.1×10^{-5}	Present work
			-188-20	2.057×10^{-5}	
AlN (black)	1.0	9.8	20-140	2.057×10^{-5}	Present work
			-188-20	2.057×10^{-5}	
AlN thin film	2MHz	Oriented 11.0	20-85	1.2×10^{-5}	Xinjiao et al
		Non-oriented 7.0	20-85	1.4×10^{-5}	

temperature is also 1.0×10^{-5} K^{-1}, but between 20°C to 120°C taking the variation as linear gives a value of 2.06×10^{-5} K^{-1} which suggests that only in the lower temperature range is the variation strictly linear. These values of temperature coefficient are frequency independent at least up to 2×10^{4} Hz. It is interesting to note also that the orders of magnitude of $\{(\epsilon'-1)(\epsilon'+2)\}^{-1}\left(\frac{\partial \epsilon'}{\partial T}\right)_p$ found for the bulk samples of substrate grade AlN are very similar to those obtained by analysis of the thin film aluminium nitride data given by Xinjiao et al.

From the point of view of utilizing aluminium nitride as a substrate material for microelectric packaging applications, it is important to make a comparison of its properties with those of its chief competitor, aluminium oxide. This is made in Table 5.6. which includes the alumina data given earlier in Table 4.3. It can be seen from this that both the actual values of permittivity and the values for the temperature coefficient are quite similar; the only noticeable difference is that $[(\epsilon'-1)(\epsilon'+2)]^{-1}\left(\frac{\partial \epsilon'}{\partial T}\right)_p$ remains constant to a somewhat higher tempeature for alumina than for aluminium nitride (260°C cf.180°C). Over the range of temperature over which the permittivity versus temperature is linear, both materials give a frequency independent value of temperature coefficient.

5.4 CONDUCTIVITY STUDIES

The d.c. conductivities of the two types of aluminium nitride were also measured over the temperature range 20°C to about 300°C at frequencies between 5×10^{2} Hz to 2×10^{4} Hz. The plot of $\log\sigma_{d.c.}$ against $\frac{1}{T}$ for the pure polycrystalline aluminium nitride is given in Fig 5.10. Between room temperature and about 200°C the graph is non-linear, but above 200°C the log plot becomes linear giving an activation energy of $\Delta E = 1.2$ eV.

The corresponding results for a.c. conductivity are given in Fig

TABLE 5.6: Comparison of Dielectric Data for Aluminium Nitride and Aluminium Oxide.

Sample	Frequency (in KHz)	ϵ' at room temp.	Temp. range	$\frac{1}{(\epsilon'-1)(\epsilon'+2)}\left(\frac{\partial \epsilon'}{\partial T}\right)_p$ (/K)
Pure AlN (substrate)		9.2	20°C-180°C	1.05×10^{-5}
Al_2O_3 pure polys. (substrate)		10.2	20°C-260°C	9.3×10^{-6}
Sapphire (parallel to C-axis)		11.5	5.5K-380K	1.07×10^{-5}
Single crystal (perpendicular to C-axis)		9.4	5.5-380K	8.89×10^{-6}

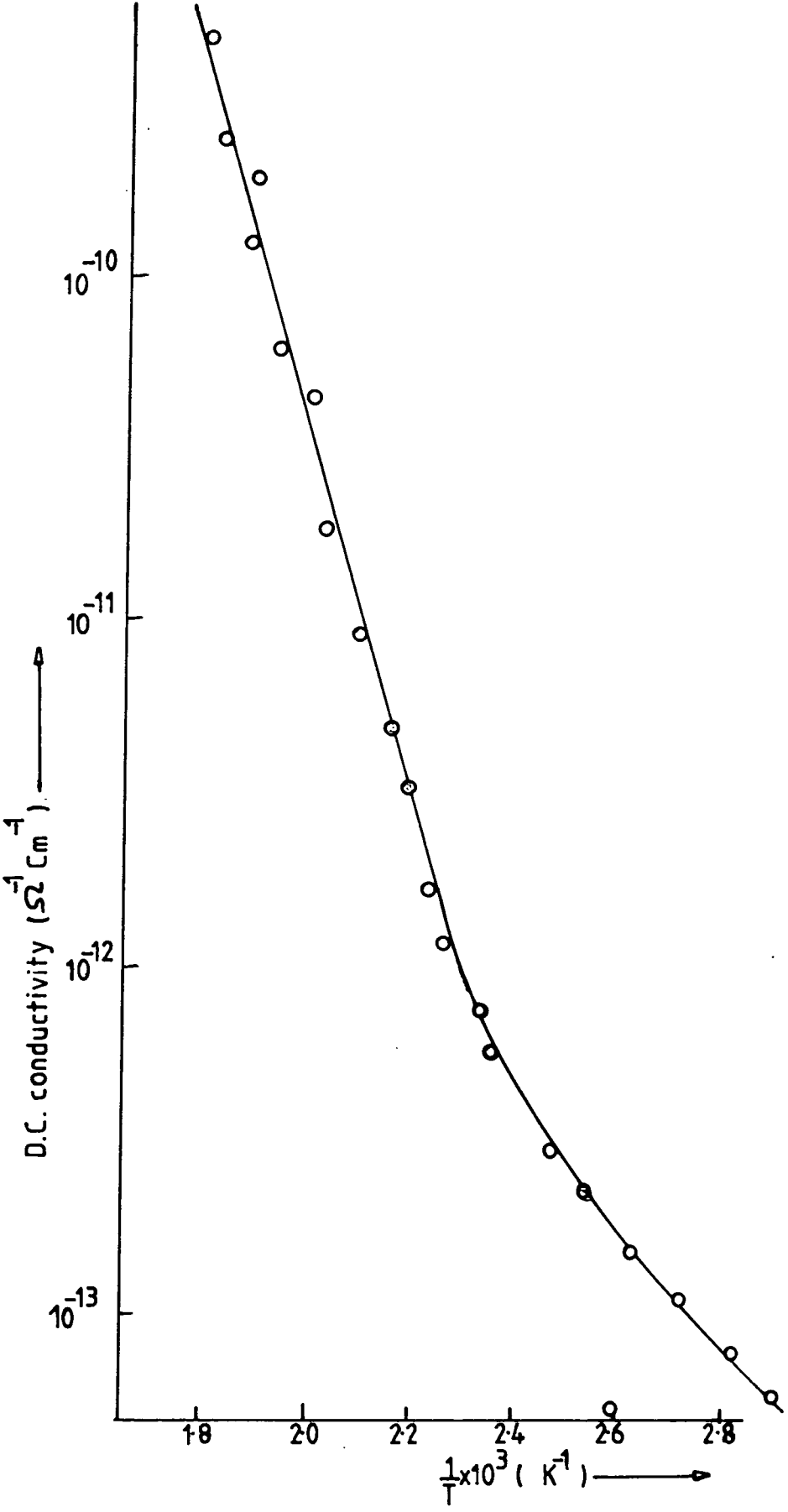

Fig. 5·10 D.C. conductivity vs. temperature data for pure polycrystalline AlN.

5.11. Near room temperature there is considerable frequency dispersion and up to about 180°C the individual plots for each frequency are non-linear. Above about 200°C the data for all frequencies converges to give a linear log plot with an activation energy of about $\Delta E = 0.86$ eV.

There do not appear to be any reports of the conductivity behaviour of pure bulk aluminium nitride in the literature to date. However, it is interesting to compare the present results with recent data, published by Xinjiao et al [5.9], on thin AlN films grown by low temperature reactive r.f. sputtering. The activation energies quoted by these authors and derived from their d.c. conductivity vs. temperature data were 0.84 eV below 85°C and 1.6 eV above 85°C. The latter figure is of a similar magnitude to that found for the bulk material.

It is also useful to compare the data with that given in Chapter 4 for aluminium oxide. For the pure polycrystalline aluminium nitride it was found that $\Delta E = 1.2$ eV compared with $\Delta E = 1.13$ eV for pure polycrystalline aluminium oxide using the d.c. conductivity data and also that $\Delta E = 0.86$ eV and $\Delta E = 0.8$ eV respectively from the A.C. conductivity data. While it is not necessarily expected that these numbers should be exactly the same for the two materials, it is interesting to note that they are quite close which may reflect the similarity of crystal structure and conduction mechanism in the two cases. Preliminary measurements on the black aluminium nitride showed that its activation energy (in the temperature range 160°C) was around 0.7 eV. This is considerably less than the value for pure material and suggests that the addition of dopants or impurities causes a reduction in activation energy in a similar manner to that found in aluminium oxide (see Chapter 4, Section 4.5).

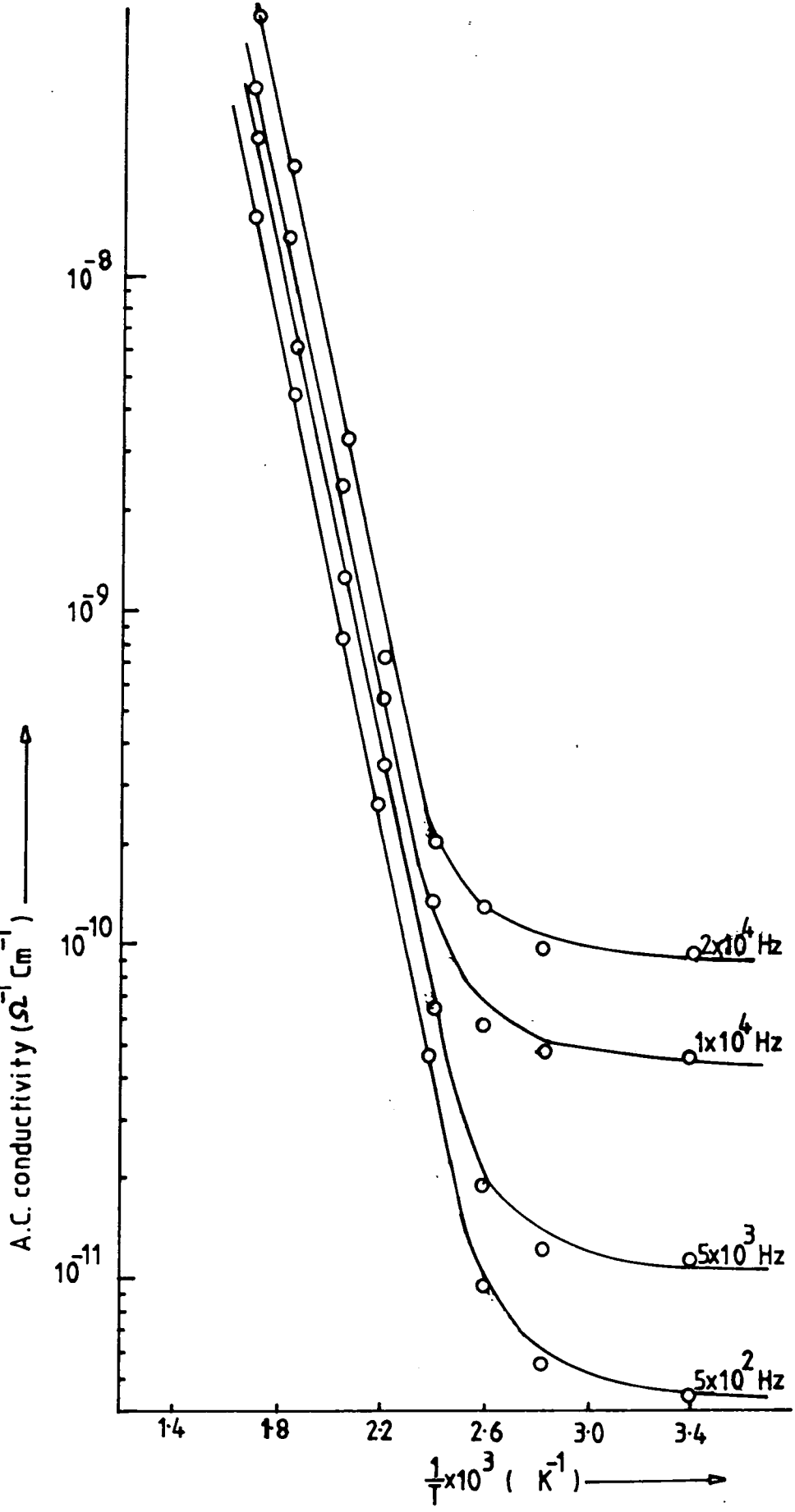

Fig. 5·11 Variation of a.c. conductivity with reciprocal temperature for pure polycrystalline AlN.

CHAPTER FIVE

REFERENCES

5.1 M.Al-Naief, Ph.D.Thesis, University of Durham, 1988.

5.2 R.M.Bozorth, "Ferromagnetism", D.Van Nostrand Co.Inc., London (1951).

5.3 H.D.Witzke, Phys.Stat.Solidi, 2 (1962) 1109.

5.4 J.Pastrnak and L. Roskovcova, Phys.Stat.Solidi, 7 (1964) 331.

5.5 K.M.Taylor and Camille Lenie, J.Electrochem.Soc., 107 (1960) 308.

5.6 A.T.Collins, E.C.Lightowlers and P.J.Dean, Phys. Rev., 158 (1967) 833.

5.7 T.L.Chu and R.W.Kelm, Jr., J.Electrochem.Soc., 122 (1975) 995.

5.8 A.J.Bosman and E.E.Havinga, Phys.Rev., 129 (1963) 1593.

5.9 Li Xinjiao, Xu Zechuan, He Ziyou, Cao Huazhe, Su Wuda, Chen Zhongcai, Zhou Feng and Wang Enguang, Thin Solid Films, 139 (1986) 271.

CHAPTER SIX

STUDIES OF GLASS ON METAL SUBSTRATES FOR MICROELECTRONIC PACKAGING

6.1 INTRODUCTION

As silicon microelectronic devices become more complex and are required to operate at higher frequencies, the type of package used to house the silicon chip increasingly affects the performance of the device. With these large high speed devices one of the major problems encountered is that of heat dissipation. Conventional ceramic packages generally have poor thermal performance in this respect. Several solutions have been suggested, such as the use of AlN substrates (described in Chapter 5) or copper-tungsten inserts, but although these materials have adequately high thermal conductivities they seem unlikely to provide a cheap easily produced alternative to alumina. As a result there is still a requirement for a substate which can combine high electrical and thermal performance with relatively low cost and conventional processing routes. Glass-on-metal and glass-ceramic on metal substrates appear to be ideal for filling these needs. In the present studies a number of glass and glass-ceramic-on-metal substrates were obtained from the Physics Department, University of Warwick (courtesy of Dr.E.A.Logan). These have been made by screen printing techniques and the glass or ceramic layer had been assessed by scanning electron microscopy and x-ray diffraction. All the glasses were based on a cordierite composition ($MgO\text{-}Al_2O_3\text{-}SiO_2$).

6.2 DIELECTRIC MEASUREMENT TECHNIQUES

The measurements were made using adaptations of the a.c. bridge techniques described in detail in Chapter 3. The major difference arose from the specimen geometry. The substrates as supplied were normally in the form of 5.0 cm x 5.0 cm squares of molybdenum with the tape cast glass layer covering on the surface. The early measurement

methods were developed for bulk single crystal specimens and used evaporated gold electrodes on each side of a thin disc-shaped sample to define the electric field region. Here, however one side of the dielectric is bonded to an extended metal base and consequently it was necessary to gold-evaporate not only a central electrode but also a circular guard ring on the glass surface to achieve good definition of the field configuration; this had the additional advantage of reducing edge field effect. The molybdenum base then served as the second electrode. Given such a sample the conductance and capacitance could then be measured directly with an a.c. bridge. The permittivity ϵ' is obtained from

$$\epsilon' = \frac{C}{C_o} \tag{6.1}$$

where C is the measured capacitance with the specimen in position and C_o is the capacitance at the same jig electrode spacing without the specimen. The conductance G of the specimen is given by

$$G = \sigma \frac{A}{d} \tag{6.2}$$

where A is the electrode area, d is the thickness of the glass and σ is the a.c. conductivity. The dielectric loss (ϵ'') is obtained from σ since

$$\sigma = \omega_o \epsilon_o \epsilon'' \tag{6.3}$$

and $\tan\delta$ is given as usual by the ratio

$$\tan\delta = \frac{\epsilon''}{\epsilon'} \tag{6.4}$$

In these measurements the main source of error lay in the uncertainty of glass layer thickness and in some cases of some non-uniformity of thickness across the specimen diameter. The accuracy of the permittivity measurement was estimated to be $\pm$ 5% and of the dielectric loss measurement $\pm$ 10%.

6.3 ROOM TEMPERATURE PERMITTIVITY AND DIELECTRIC LOSS

Data for substrates having thickness of glass in the 100 μm to 130 μm range is presented in Fig.6.1(a) and (b) which also shows for comparison the results obtained over the same frequency range ($5x10^2$Hz to $5x10^6$Hz) for a 0.46 mm thick sample of pure bulk cordierite glass. It can be seen that both ϵ' and ϵ'' are substantially independent of frequency over this range. For the glass-on-metal the average value obtained for the permittivity was $\epsilon' = 6.5$ at 1×10^3 Hz which compares well with that of $\epsilon' = 6.8$ for bulk cordierite glass, bearing in mind the difficulties of obtaining precise values for glass thickness. It is noticeable that whereas the ϵ' values of the two substrates are very similar,there is a more noticeable difference in their losses. However, the average loss of about $\epsilon'' \sim 7 \times 10^{-2}$ is not much greater than that of the bulk cordierite glass giving tanδ values in the region of 8×10^{-3} as compared with 3×10^{-3} for the bulk glass.

Measurements were also made on a series of substrates having successively thicker glass coatings. These substrates were made by repeated printing under identical furnace processing conditions, a procedure which should therefore give increasing thicknesses of the same composition of glass. The number of successive prints ranged from one to six, corresponding to glass thicknesses of 14 μm to 128 μm. The actual layer thicknesses were measured directly using a precision micrometer and taking the average of values obtained at many different points over the whole sample. The variation of thickness with the number of prints is shown in Fig 6.2, the linearity of which indicates the reliability of the over-printing technique. The permittivity values were fairly consistent averaging at $\epsilon' \sim 6.3$; they are detailed in Table 6.1 which also includes for comparison data taken from previous studies of bulk samples of both cordierite glass and magnesium sialon glass of similar composition [6.1]. There was however a much

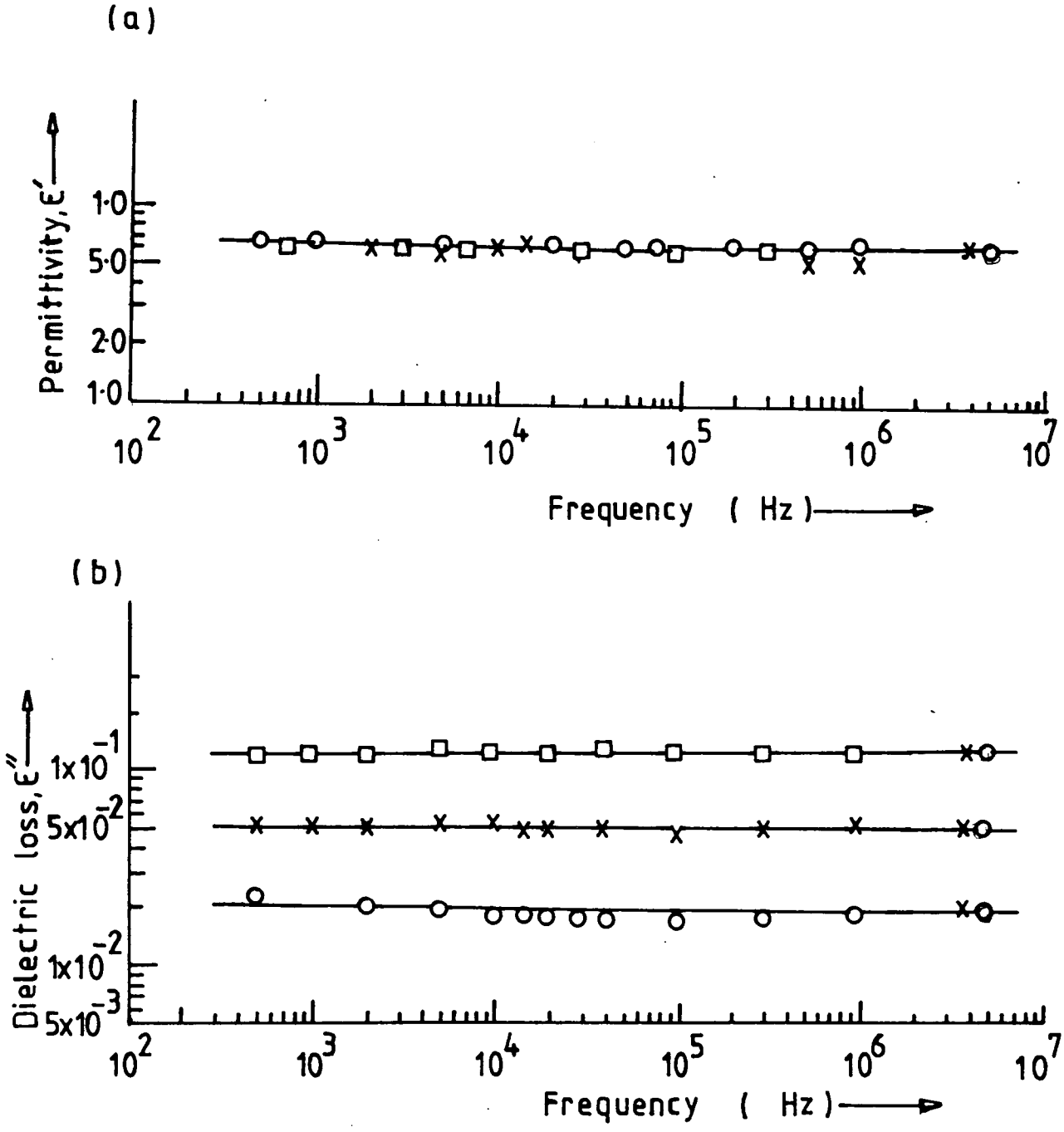

Fig. 6·1 Frequency dependencies of (a) permittivity and (b) dielectric loss for glass-on-molybdenum substrates; key: (x) 100 μm thick glass/Mo, (□) 128 μm thick glass/Mo, (○) bulk cordierite glass.

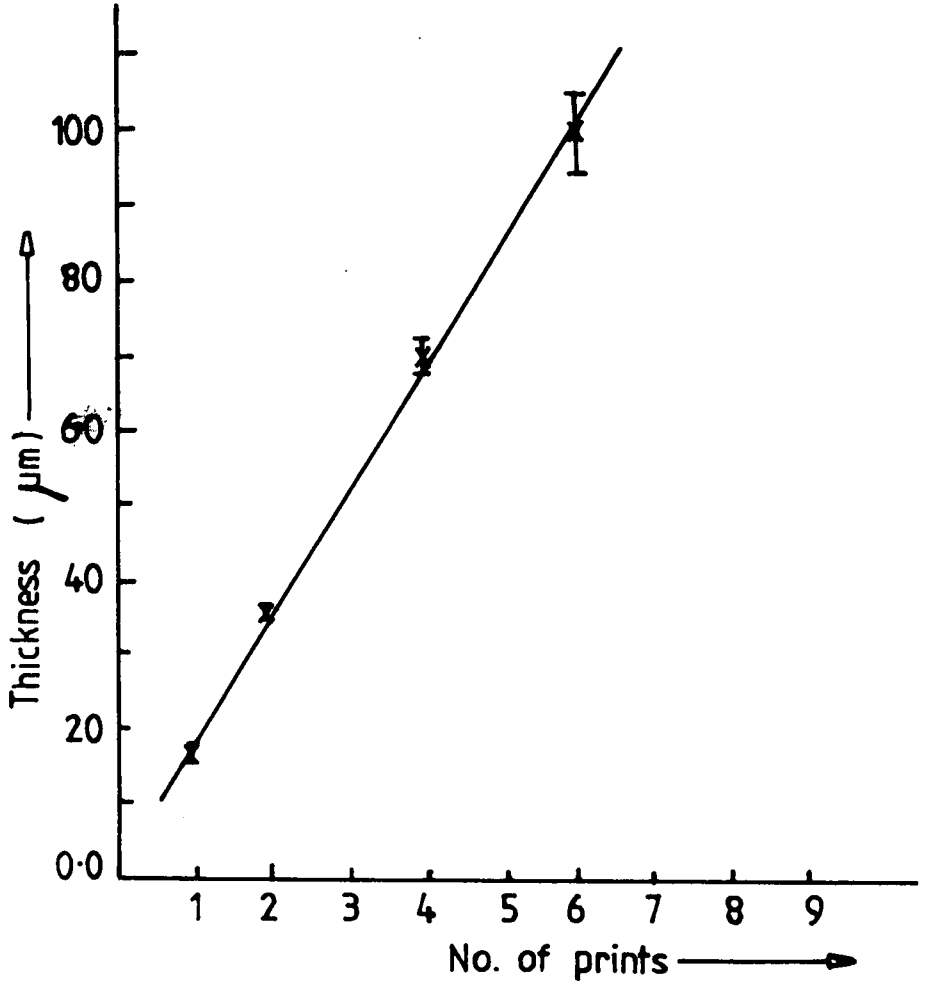

Fig. 6·2 Variation of thickness of printed glass on molybdenum substrates.

TABLE 6.1: Permittivity values at 1 x 10^3 Hz obtained for specimens with different glass thicknesses.

Glass-on-metal

Thickness (μm)	14	52	60	100	128
Permittivity	6.7	5.9	6.0	5.8	7.3

Glass detached from metal base

Thickness (μm)	74	82
Permittivity	7.2	7.3

Bulk cordierite glass ($MgO.Al_2O_3.SiO_2$, 20:20:60 wt%)

Thickness (mm)	0.46
Permittivity	6.5

Bulk Magnesium sialon glass, Mg-Si-Al-O-N (0% N, ref. 6.1 and 6.2)

Thickness (mm)	0.33
Permittivity	6.7

more marked variation of dielectric loss with glass thickness. This is illustrated by Figures 6.3 and 6.4 which show the frequency variations of ϵ' and ϵ'' for substrates having thicknesses of 60 μm and 14 μm respectively. The main feature is the non-linearity of the ϵ'' versus frequency characteristics; this is reflected, though to a very greater extent, in the variation of ϵ'' versus frequency where in each case there is a small reduction in ϵ' as frequency increases. The tanδ values are quite high for the thinner layers at low frequencies being for example 7.14×10^{-1} at 5×10^{2} Hz for the thinnest (14 μm) layer and 1.2×10^{-1} (also at 5×10^{2} Hz) for the 60 μm thick layer as compared with the frequency independent value of tan$\delta = 8 \times 10^{-3}$ obtained for the thickest layer (i.e. 128 μm thick). It is likely that the reason for both the curvature of the ϵ'' versus frequency plots for the thinner layers and these high values of tanδ is that there is some contamination by metal or metal oxide very near the glass/metal interface.

Returning to consider the data obtained for the thicker samples the frequency independence of both ϵ' and ϵ'' (Fig 6.1) suggests that the Universal law of dielectric response applies. Taking numerical data from the plots and assuming a value of $\epsilon' = 2.46$ [6.1], which was obtained from the optical refractive index, gives a value of the exponent n in the relation

$$(\epsilon' - \epsilon_{\infty}) \propto \omega^{n-1} \qquad (6.5)$$

of $n = 0.98 \pm 0.02$; the corresponding value obtained from the ϵ'' versus frequency plot assuming

$$\epsilon'' \propto \omega^{n-1} \qquad (6.6)$$

gives $n = 0.98 \pm 0.02$.

The close agreement between these two values shows that the Universal law can be applied with some confidence. This general behaviour agrees very well with that reported by Kenmuir et al [6.1,

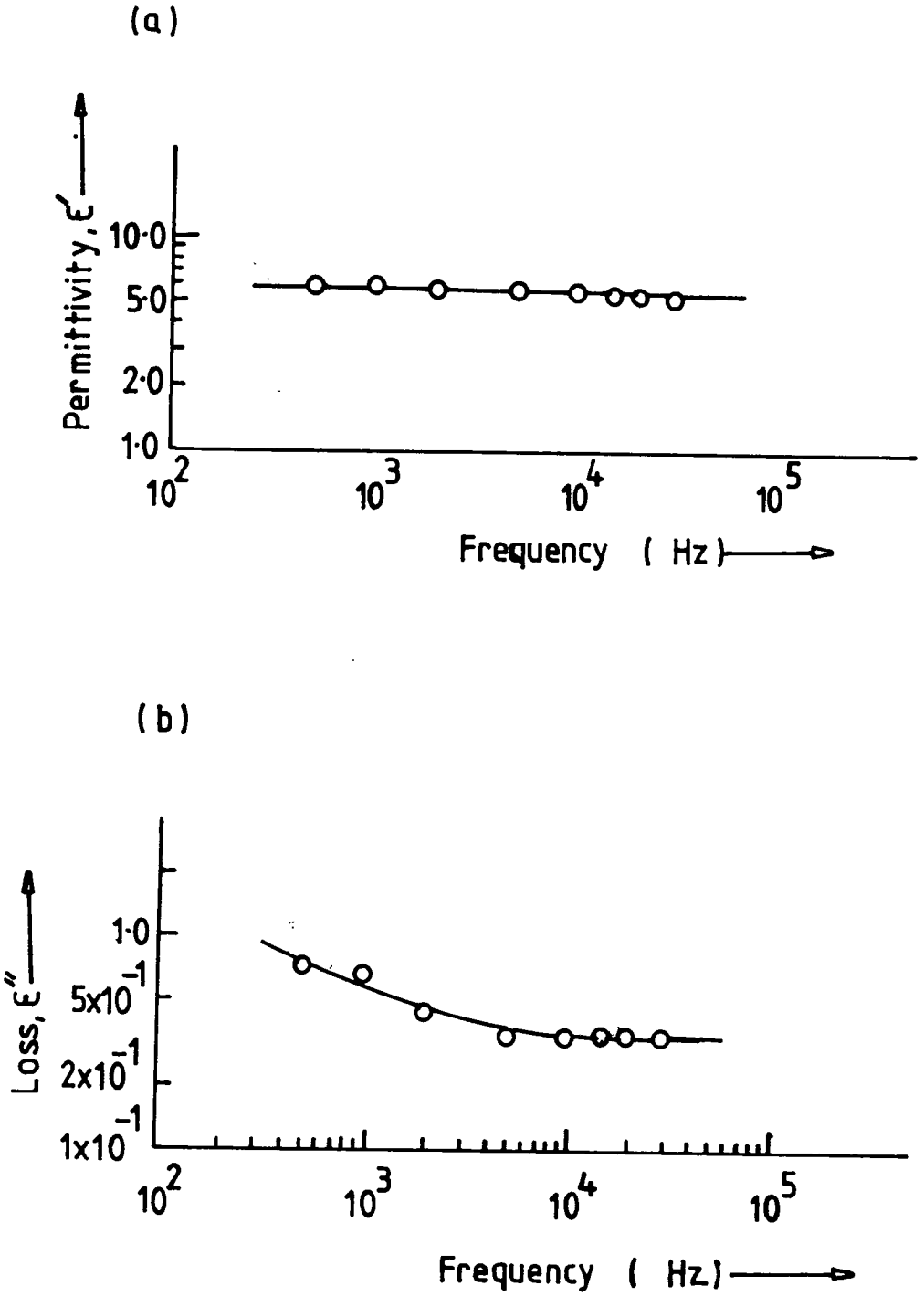

Fig. 6·3 (a) Permittivity vs. frequency and (b) loss vs. frequency for 60 μm glass thickness.

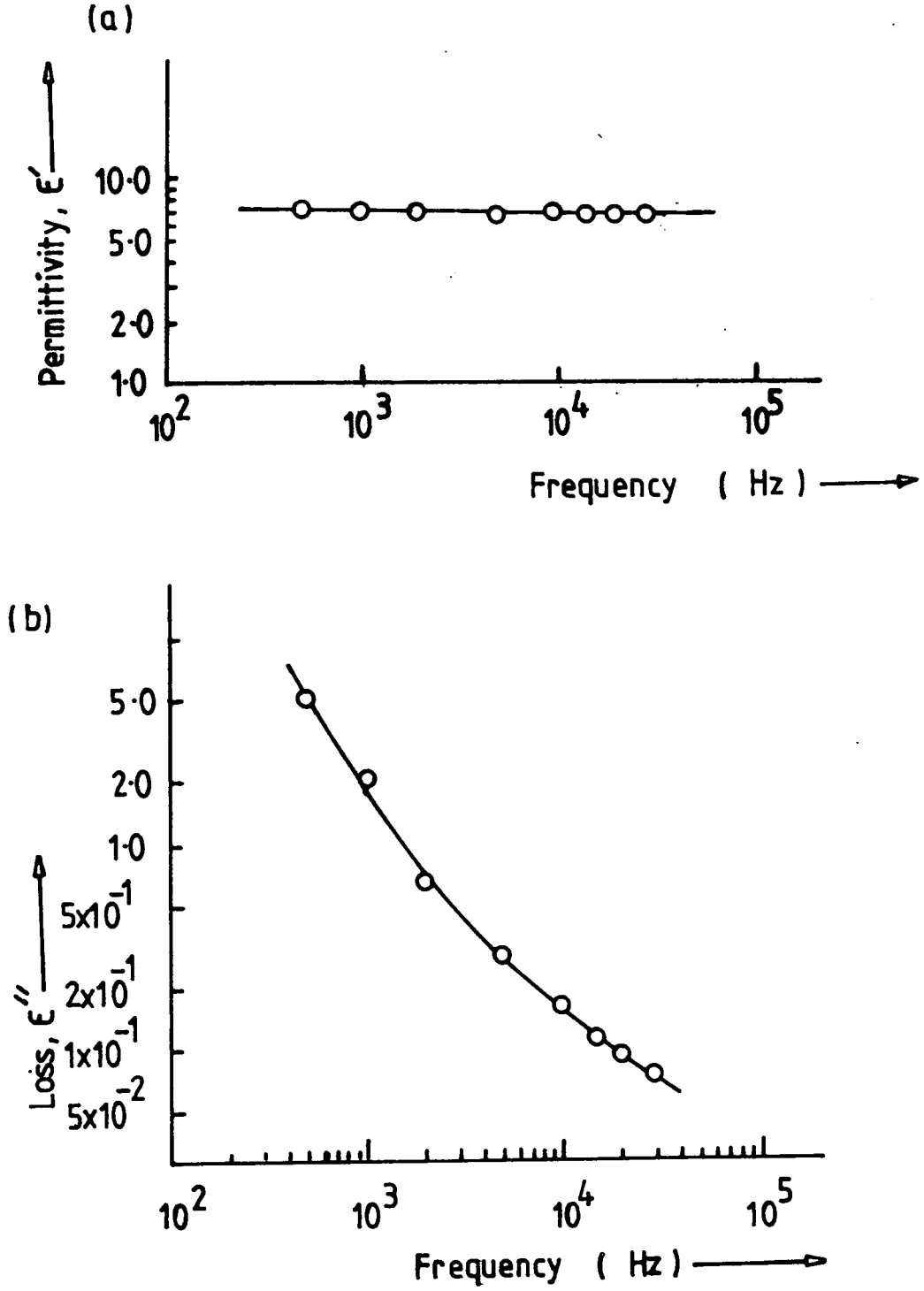

Fig. 6·4 (a) Permittivity vs. frequency and (b) loss vs. frequency plots for 14 μm glass thickness.

6.2] who studied the dielectric behaviour of magnesium-aluminium-silicon, calcium-aluminium-silicon, yttrium-aluminium-silicon and Neodymium-aluminium-silicon oxynitride glasses over a similar frequency range at room temperature. In these measurements bulk specimens were used whose dimensions were typically 1.0 cm diameter and 0.05 cm thickness. For the pure oxide magnesium-aluminium-silicon glass, which had a composition very near to that of the cordierite glass used here for the glass-on-molbydenum substrate, Kenmuir et al found that ϵ' = 6.8 and that both ϵ' and ϵ'' were frequency independent giving from both the permittivity and loss variations the value $n = 1.0 \pm 0.1$. They also state that the value found for $\tan\delta$ for the oxide magnesium-aluminium-glass was $\tan\delta = 2 \times 10^{-3}$. All these values are in fairly close agreement with the data reported here for the glass-on-molybdenum substrates.

6.4 TEMPERATURE COEFFICIENT OF PERMITTIVITY

The temperature variation of permittivity was measured over a temperature range of 20°C to 300°C by suspending the specimen in an (air-ambient) furnace; a platinum paste/platinum wire arrangement was used to make the contact to the glass face. The plot of ϵ' against temperature for a 101 μm thick glass layer on molybdenum is given in Fig 6.5. At each frequency the variation is linear up to about 120°C and over this region the temperature coefficients of permittivity,

$$[(\epsilon'-1)\ (\epsilon'+2)]^{-1} \left(\frac{\partial \epsilon'}{\partial T}\right)_p$$ were derived [6.3].

Even in this low temperature region the actual value of permittivity and the temperature coefficient do show significant differences at different frequencies. The actual values for the temperature coefficients vary from $1.73 \times 10^{-5}\ K^{-1}$ at 5×10^{2} Hz to $1.0 \times 10^{-5}\ K^{-1}$ at 2×10^{4} Hz giving an average (since the variation with frequency is relatively small) of about $1.36 \times 10^{-5}\ K^{-1}$. This is

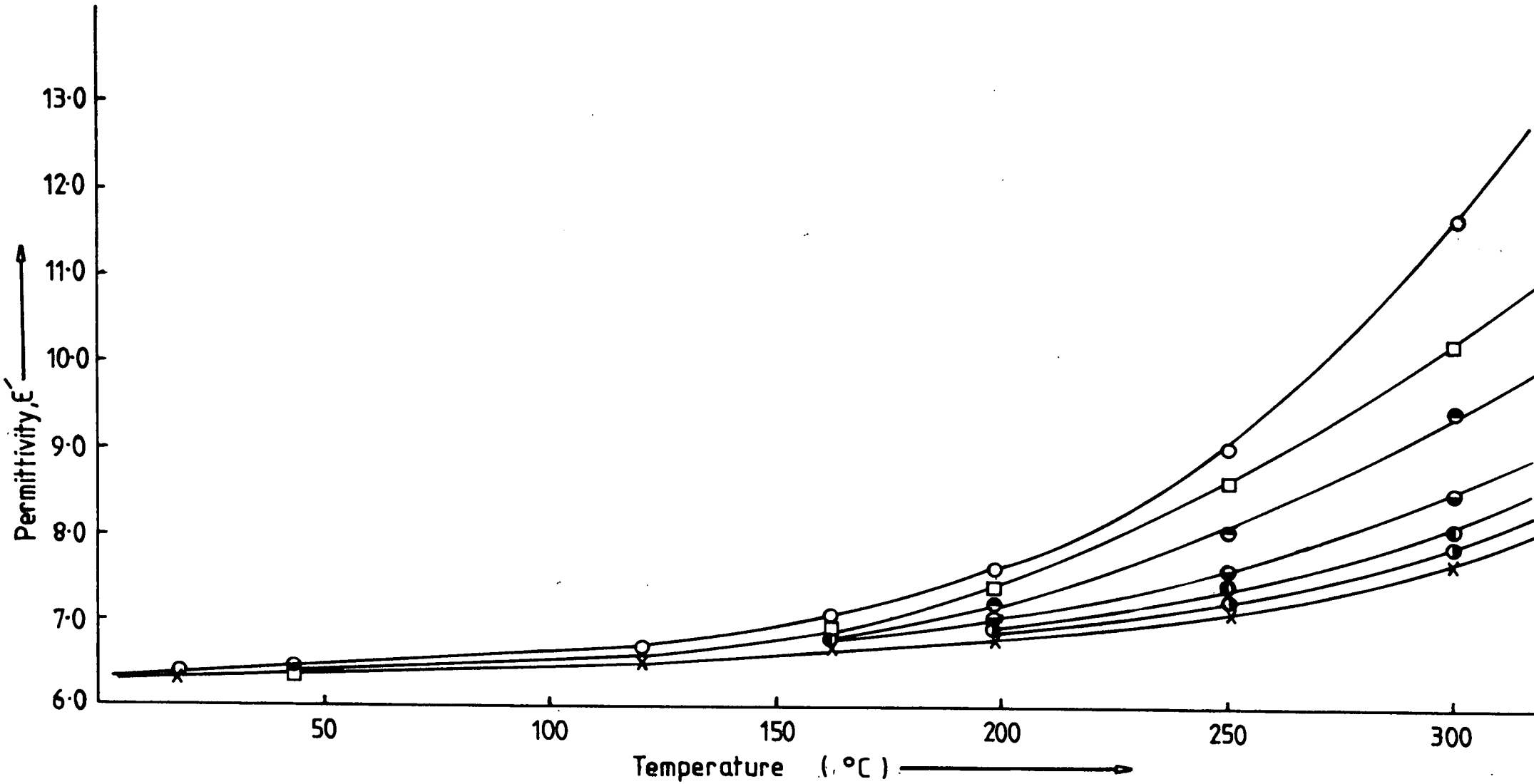

Fig. 6·5 Variation of permittivity with temperature for glass-on-molybdenum substrate (101 μm thick); Key: 5×10^{2} Hz(○), 1×10^{3} Hz(□), 2×10^{3} Hz(◒), 5×10^{3} Hz(◒), 1×10^{4} Hz(◐), $1{\cdot}5\times10^{4}$ Hz(◑), 2×10^{4} Hz(x).

rather higher than the values of 1.05×10^{-5} K^{-1} for aluminium nitride and also of 9.3×10^{-6} K^{-1} for aluminium oxide. Above 120°C the value of $\{(\epsilon'-1)(\epsilon'+2)\}^{-1}\left(\frac{\partial \epsilon'}{\partial T}\right)_p$ for each individual frequency increases with increasing temperature much more rapidly than would be expected from the Bosman and Havinga formula. Taking the averages over small temperature intervals for each frequency gives the data tabulated in Table 6.2. From Table 6.2 it can be seen for example that whereas near room temperature the low frequency and high frequency values of the temperature coefficients vary by a factor of only about 1.7, above 250°C this factor increases to over 3.0 times. The experimental results shown in Fig 6.5 can be replotted to show the variation of permittivity with frequency at different temperatures, Fig 6.6. This form of display emphasises the reduction in the variation of permittivity for a given temperature difference as the frequency increases. This form of behaviour has been observed in other materials. In a study of the temperature dependence of permittivity in magnesium oxide (MgO) and Fe-MgO single crystals, Thorp et al made measurements over the temperature range 20° C to 650° C for frequencies between 5×10^2 Hz and 5×10^4 Hz, a range of temperature and frequency very similar to those used in the present work. They found that from 25°C to about 200°C the temperature dependence of ϵ' fitted well with Bosman and Havinga's formula and quoted the value of $[(\epsilon'-1)\ (\epsilon' + 2)]^{-1}\left(\frac{\partial \epsilon'}{\partial T}\right)_p = 1.02 \times 10^{-5}$ K^{-1} for undoped MgO; they also found that this increased considerably with the addition of iron, rising to 2.85×10^{-5} K^{-1} for MgO single crystals doped with 12900 p.p.m iron. For MgO above 200°C the permittivity also changes much more rapidly than the Bosman formula predicts and the results in the high temperature region were discussed in terms of a contribution to the

TABLE 6.2: Variation of temperature coefficient with mean temperature for different frequenices.

Frequency (Hz)	$\left[(\epsilon'-1)(\epsilon'+2)\right]^{-1}\left(\frac{\partial\epsilon'}{\partial T}\right)_p$ (K^{-1})				
	Temperature Range (°C)				
	20-120	120-162	162-198	198-250	250-301
5×10^2	1.73×10^{-5}	2.61×10^{-5}	3.18×10^{-5}	6.65×10^{-5}	9.34×10^{-5}
2×10^3	1.52×10^{-5}	1.70×10^{-5}	2.10×10^{-5}	4.43×10^{-5}	6.16×10^{-5}
5×10^3	1.38×10^{-5}	1.39×10^{-5}	1.54×10^{-5}	3.21×10^{-5}	4.30×10^{-5}
2×10^4	1.0×10^{-5}	1.11×10^{-5}	1.17×10^{-5}	2.05×10^{-5}	2.88×10^{-5}

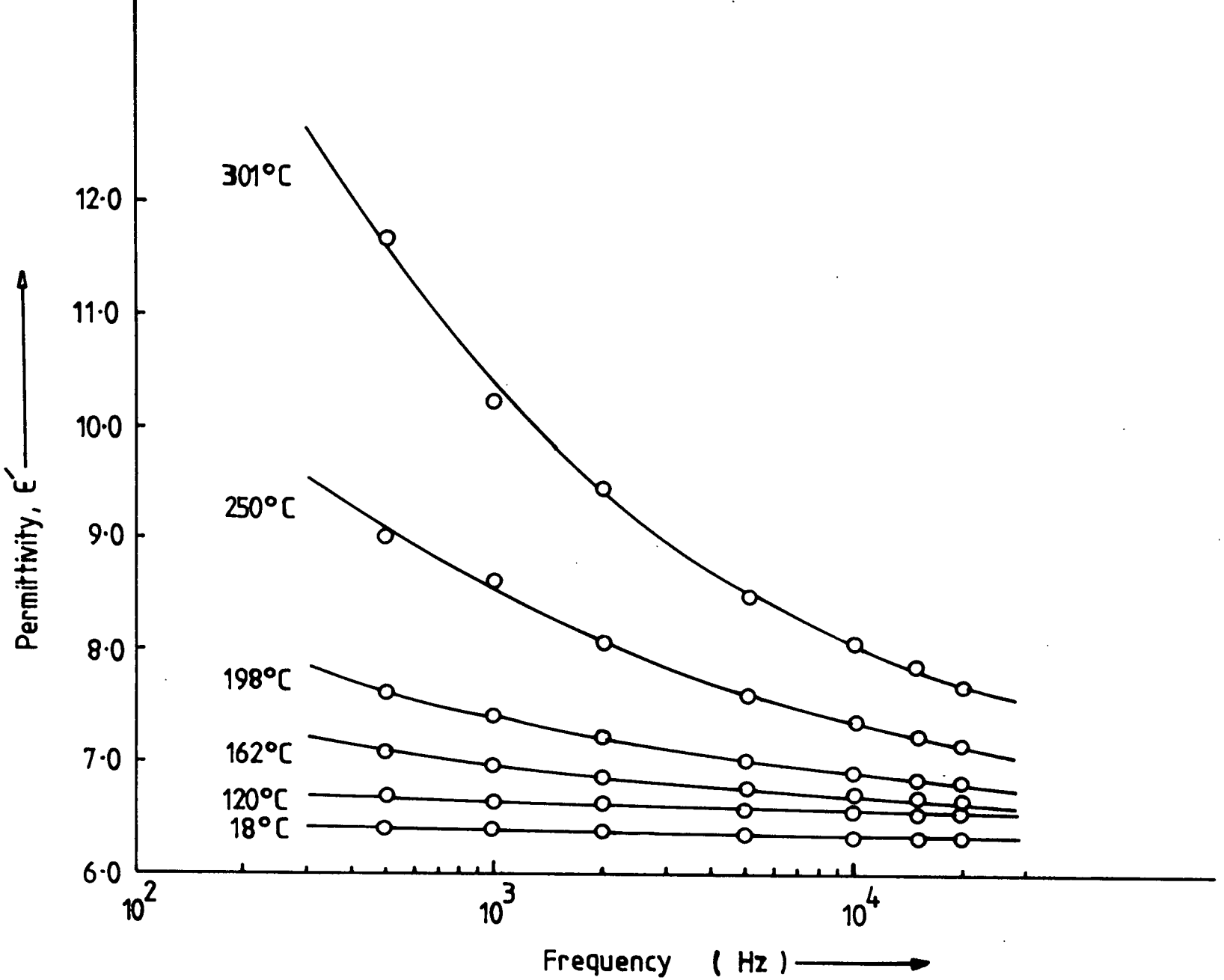

Fig. 6·6 Variation of permittivity with frequency for different temperatures ; glass-on-molybdenum substrate (101 μm thick).

measured permittivity arising from temperature enhanced conductivity. Here the high temperature data from the Figures 6.5 and 6.6 has been replotted as a $\log\epsilon'$ vs.temperature plot for three separate frequencies. This is shown in Fig 6.7. Each plot is linear which shows that over this temperature range a good fit is obtained to single exponential behaviour indicating that a single (rather a double or more complex) process is involved.

6.5 CONDUCTIVITY STUDIES

Preliminary examinations of both the d.c. and a.c. conductivities were made over the temperature range 20°C to 440°C. The d.c. conductivity variation with reciprocal temperature is shown in Fig 6.8. The data fits extremely well to a linear-log plot over the whole temperature range and yields an activation energy for d.c. conduction of $\Delta E = 0.76$ eV. The a.c. conductivity data is shown in Fig 6.9. From room tempeature to about 160°C the variation is very non-linear. This applies for each of the frequencies. Above about 160°C each plot becomes linear; at 5×10^2 Hz the activation energy above 160°C is 0.39 eV and the corresponding figure at 2×10^4 Hz is 0.35 eV. These values for the glass-on-metal are much lower than the corresponding activation energies for a.c. conductivity, measured over similar ranges and frequencies, of 0.8 eV for pure polycrystalline alumina and 0.86 eV for pure polycrystalline aluminium nitride.

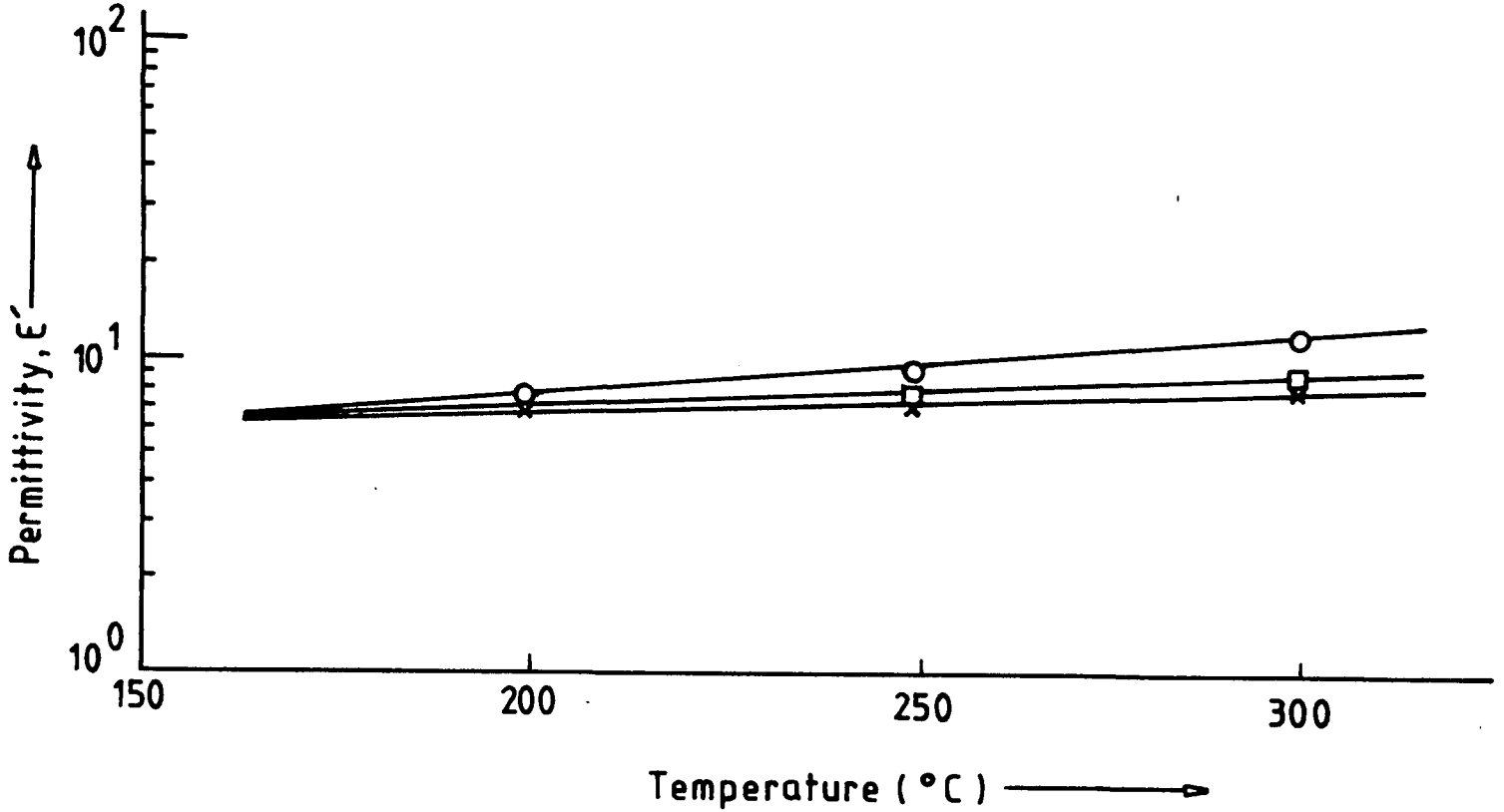

Fig. 6·7 Log ε′ vs. temperature plot for glass—on—molybdenum.
Key: 5×10^2 Hz(○), 5×10^3 Hz (□) and 2×10^4 Hz(x).

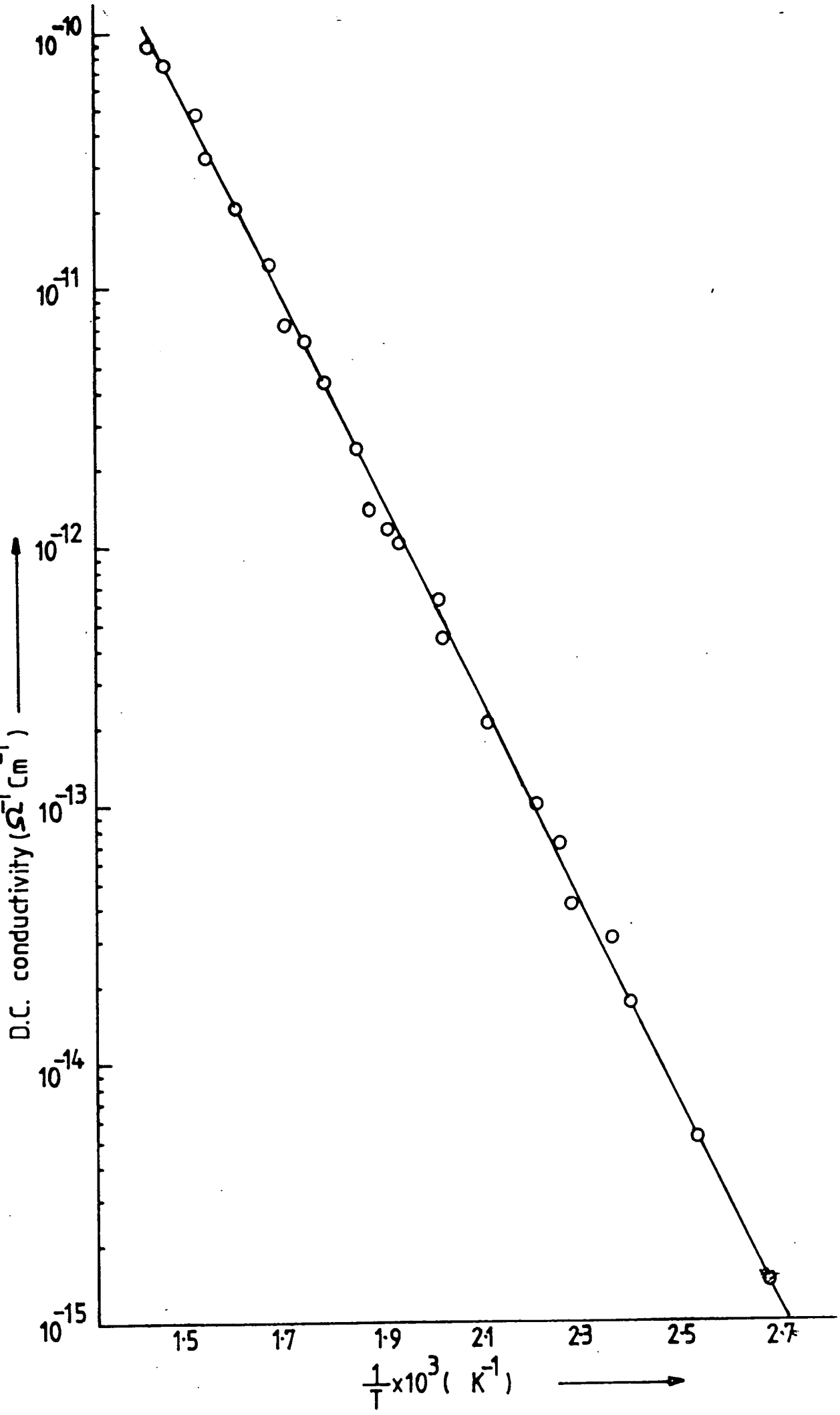

Fig. 6·8 D.C. conductivity vs. temperature data for glass-on-molybdenum substrate (101 μm thick).

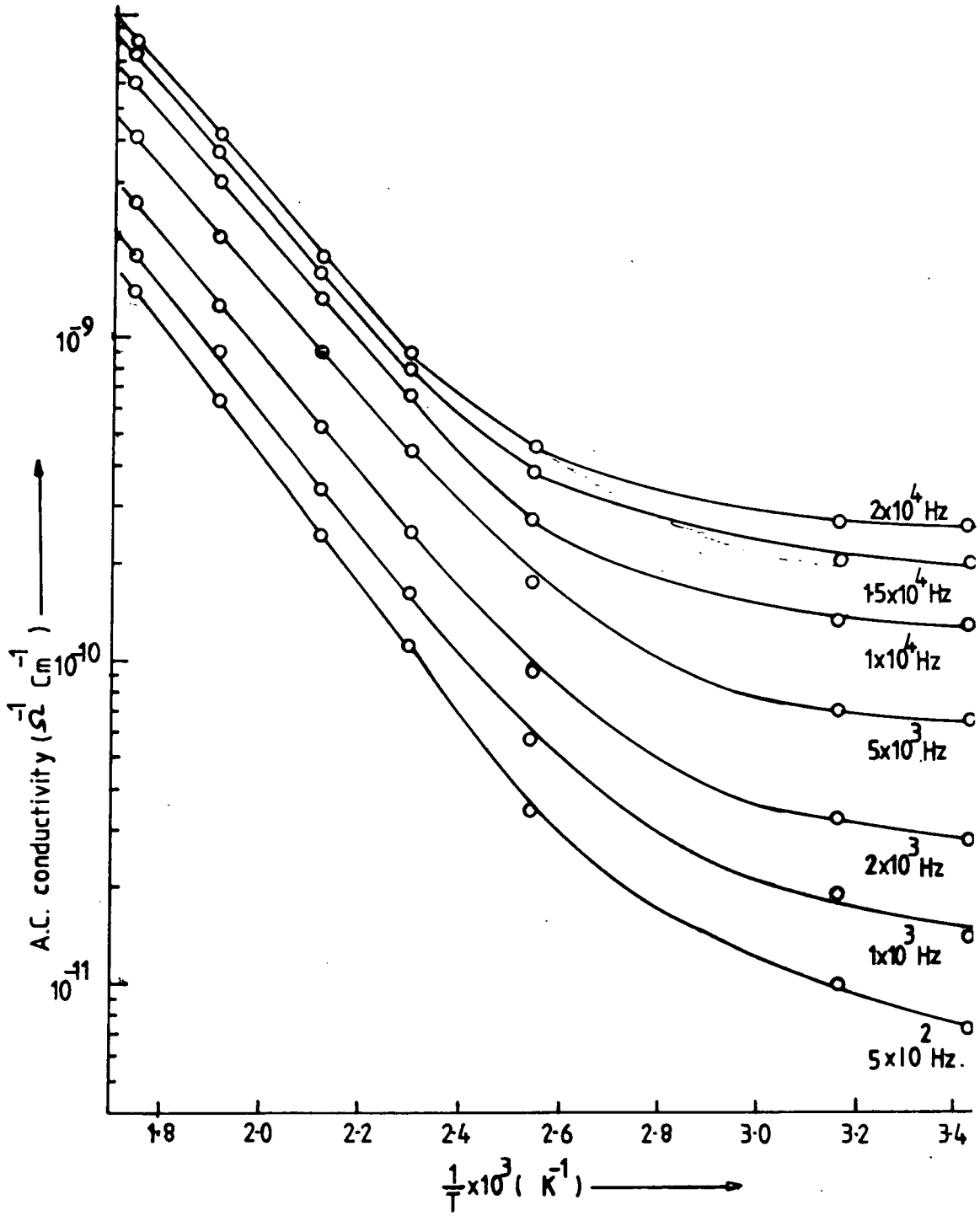

Fig. 6·9 Variation of a.c. conductivity with reciprocal temperature for glass-on-molybdenum substrate (101 μm thick layer).

CHAPTER SIX

REFERENCES

6.1 S.V.J.Kenmuir, J.S.Thorp and B.L.J.Kulesza, J.of Mat.Sci., 18 (1983) 1725.

6.2 J.S.Thorp and S.V.J.Kenmuir, J.of Mat.Sci. 16 (1981) 1407.

6.3 A.J.Bosman and E.E.Havinga, Phy.Rev., 129 (1963) 1593.

6.4 J.S.Thorp, N.E.Rad, D.Evans, C.D.H.Williams, J.of Mat.Sci., 21 (1986) 3091.

CHAPTER SEVEN

PERMITTIVITY STUDIES OF POWDERS

7.1 INTRODUCTION

It is generally accepted [7.1] that the permittivity of solids at room temperature depends on the combination of the electronic, ionic, dipolar and space-charge polarization mechanisms which may be operative. The manner in which the permittivity varies with frequency indicates which contributions are present. The electronic, ionic and dipolar effects are related to the inherent nature of the material but space-charge polarization, which originates because of grain boundaries, depends on the microstructure of the material. Thus the contribution, due to space charge polarization, depends on the purity and perfection of materials [7.2] and its influence is noticeable mainly in the low frequency region; it ceases to be important above ~ 10^5 Hz.

Careful growth and preparation of single crystals can give samples having high degrees of perfection and purity and in these there is practically no contribution from space charge polarization. In such crystals only the electronic, ionic and dipolar polarization mechanisms are active and, for the materials examined here, a good fit with the Universal law of dielectric response was found, i.e. the permittivity was independent of frequency. On the otherhand, in powder dielectrics, there are a very large number of grain boundaries present and these cause space-charge polarization. The contribution of this space-charge polarization at room temperature and low frequency is so dominant that the contributions from the other mechanisms become negligible. A survey of the literature shows that most of the powder samples which have been characterized have been measured at high frequencies, e.g. the r.f. permittivity and dielectric loss of calcium, iron and magnesium silicides [7.3]. In the present studies on powder

dielectrics a new approach has been introduced in order to be able to obtain data at low frequencies. This was to make measurements at low temperature, 77K being used here. To some extent this follows the procedure used by Weichman [7.4] who encountered space charge difficulties when examining solid polycrystalline copper-oxide. For the correlation between the powder value obtained directly from the experiment and the equivalent solid value characterizing each powder grain, the widely accepted Looyenga formulae have been used. These formulae are [7.5]

$$\epsilon'_s = \left[\frac{\epsilon'^{1/3}_p - 1 + \delta}{\delta} \right]^3 \qquad (7.1)$$

$$\epsilon''_s = \left(\frac{\epsilon''_p}{\delta} \right) \left(\frac{\epsilon'_s}{\epsilon'_p} \right)^{2/3} \qquad (7.2)$$

where ϵ'_s and ϵ''_s are the equivalent solid permittivity and dielectric loss respectively; ϵ'_p and ϵ''_p are the powder permittivity and dielectric loss respectively and δ is the packing fraction. A wide range of materials have been examined partly to test the validity of the method and also to enable measurements to be made on materials only available in powder form. Most of the samples characterized had packing fractions of about 0.5. In all cases the co-axial holder technique (described in Chapter 3, Section 3.2.3) was used.

7.2 Al_2O_3, Fe/Al_2O_3 and AlN POWDERS

The equivalent solid permittivities (ϵ'_s) for the Al_2O_3 (purity 99.99%) and AlN (purity 97%) powders, each of which was measured at both 20° C and 77K are shown in Fig 7.1a and 7.1b respectively. At 20° C both materials show strong frequency dispersion in the low frequency range (1.0×10^3 Hz to 3.0×10^4 Hz), as had been expected.

The frequency dispersion of ϵ'_s decreases rapidly at frequencies approaching frequency 10^5 Hz. At 20°C the ϵ'_s values for the powders are some 10 to 20 times greater than the values at the corresponding frequencies of the bulk polycrystalline materials which clearly indicates the presence of space-charge polarization and its dominant role at low frequencies. At 77K, however, the ϵ'_s vs. frequency plots for both sample are quite flat ; this indicates the absence of space-charge polarization and gives a result fitting well with the Universal law of dielectric response [7.6] found to be applicable for the bulk samples. The numerical values obtained from the 77K data given in Fig 7.1b (for both Al_2O_3 and AlN) give good agreement both with the data given for bulk materials in Chapter 4 and Chapter 5 and with the values quoted in the literaturte (7.7 - 7.8).

Since iron is often present as an impurity in many commercial grade powders an attempt was made to estimate its influence by examining a mixed Fe/Al_2O_3 powder containing 90 wt% Al_2O_3 powder and 10 wt% iron as iron powder. The results for this mixed powder are also shown in Fig 7.1. The room temperature plot again shows strong space-charge polarization which is removed completely by cooling to 77K. The permittivity of the mixed powder, $\epsilon'_s = 12.5$ at 77K independent of frequency, is higher than for the pure alumina powder ($\epsilon'_s = 10.2$), an increase attributable to the presence of the high permittivity iron. An estimate can be made of the increase of magnitude expected by the application of the logarithmic mixing rule [7.9], which gives the resultant permittivity ϵ'_T of a two component mixture as

$$\log \epsilon'_T = V_A \log \epsilon'_A + V_B \log \epsilon'_B \qquad (7.3)$$

where V_A and V_B are the volume fractions of the component having

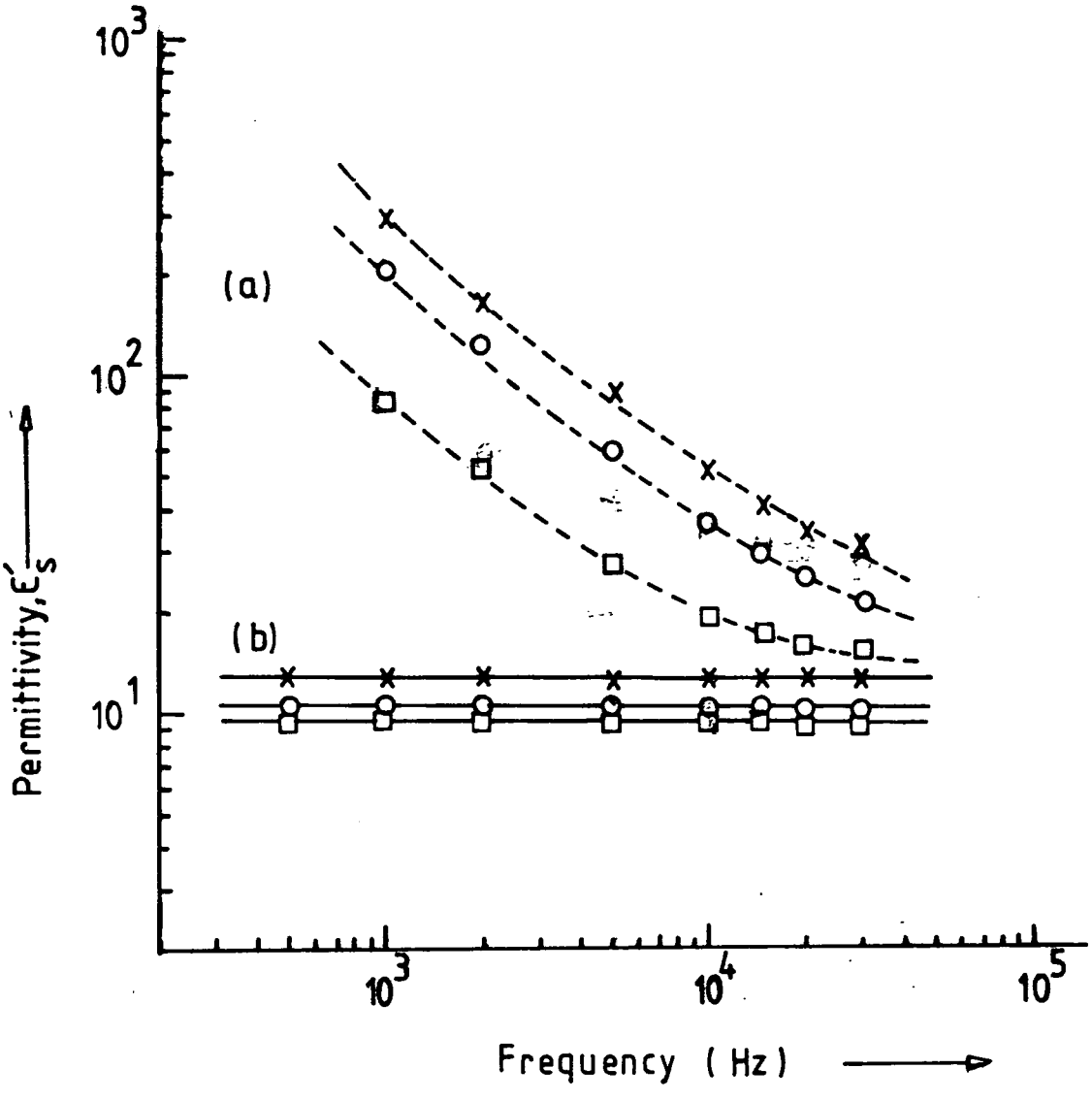

Fig. 7·1 Permittivity vs. frequency variation for Al_2O_3 (○), Fe/Al_2O_3 (x) and AlN (□) powders ; (a) 20 °C (---) and (b) 77K (——).

permittivities ϵ'_A and ϵ'_B respectively.

In the calculation made here the values of permitivity of metallic iron [7.10] and Al_2O_3 have been taken as $\epsilon'_{Fe} = 10^5$ and $\epsilon'_{Al_2O_3} = 10.2$ respectively. The sample contained 10 wt% iron and 90 wt% alumina. Converting these, taking the densities of iron and alumina as 7.86 gm/c.c. and 3.97 gm/c.c. respectively, to volumes gives 1.27 c.c. of iron and 22.67 c.c. of alumina. Expressed as volume fractions this gives $V_{Fe} = 0.053$ and $V_{Al_2O_3} = 0.947$. Inserting these values into equation 7.3 gives the predicted magnitude of the permittivity of the mixed Fe/Al_2O_3 powder as $\epsilon'_T = 16.6$. This is in very reasonable agreement with the result observed experimentally, bearing in mind that the calculation depends critically on the permittivity value taken for iron (if one assumes $\epsilon'_{Fe} = 10^4$ then, $\epsilon'_T = 14.7$).

7.3 MgO and Mg_3N_2 POWDERS

As a further test of the technique measurements were made on pure MgO (purity 99.99%) powder. This material was chosen because the dielectric properties of both pure and doped single crystals have been fairly fully discussed in a series of papers by Thorp et al[e.g. 7.11], so it gave a useful additional reference standard. The ϵ'_s vs frequency plots (Fig 7.2) again show a large space charge polarization contribution at room temperature (which is not completely removed even at 3×10^4 Hz) and a virtually frequency independent response at 77 K. Taking the 77K data gives a value of $\epsilon'_s = 9.67$ for pure powdered MgO, in excellent agreement with the value of $\epsilon' = 9.62$ quoted by Thorp and Rad for pure single crystal MgO. This gives additional confirmation not only of the experimental technique but also of the validity of using the Looyenga formula for the derivation of ϵ'_s from ϵ'_p with low packing fraction.

In contrast to the behaviour of magnesium oxide the result for magnesium nitride (purity 99%) on which there appears to be no

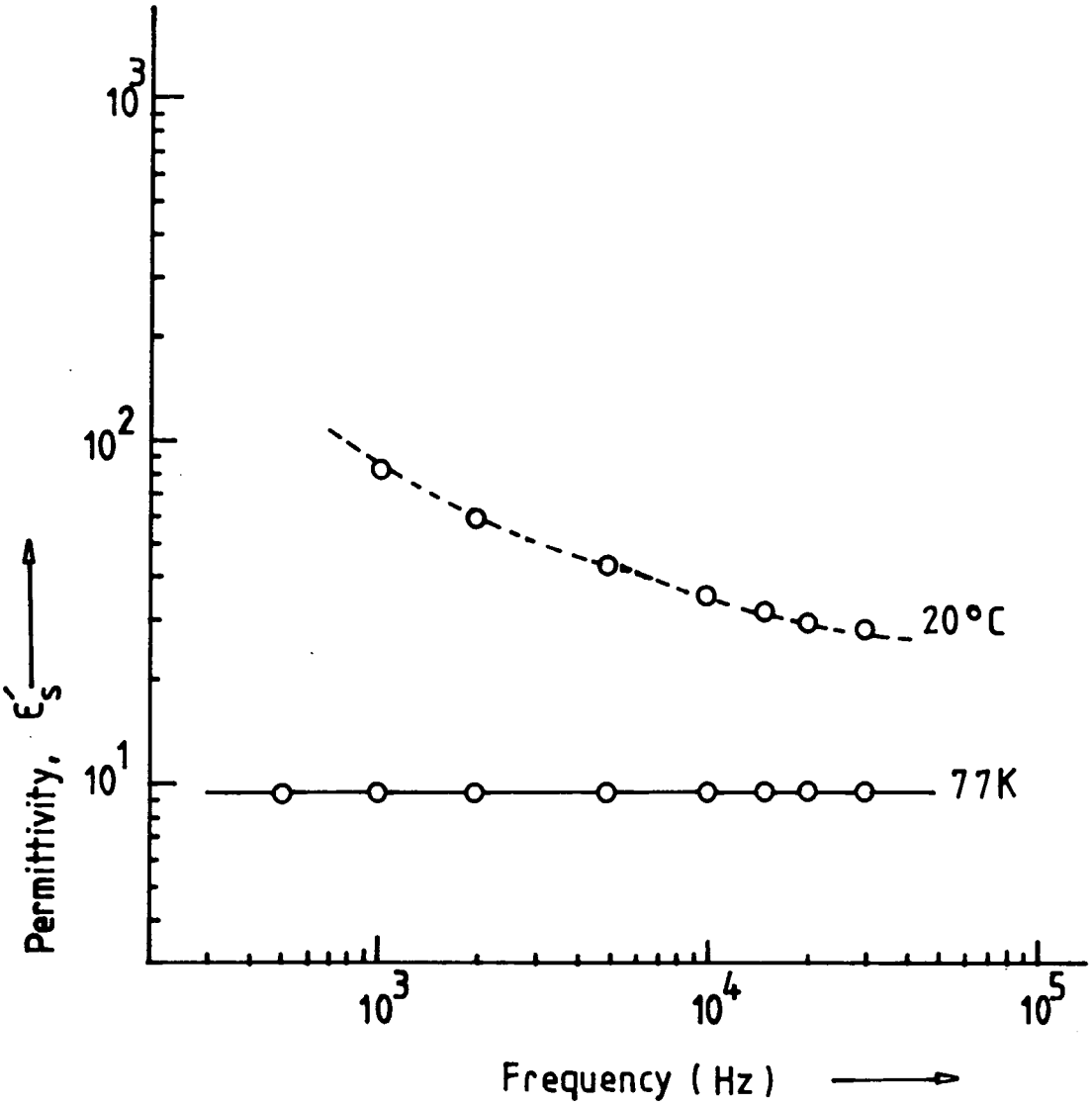

Fig. 7·2 Permittivity vs. frequency variation for Magnesium oxide powder.

dielectric data in the literature, show little evidence for space-charge polarization at room temperature, (Fig 7.3). There is in fact very little difference between the room temperature and 77K values of ϵ'_s and the 77K results give $\epsilon'_s = 46$, independent of frequency up to 3×10^4 Hz. This is much higher than that for the oxide.

7.4 SUPERCONDUCTING AND RELATED OXIDES

Three samples of yttrium-barium-copper oxide superconducting powder having nominal composition, $Y_1Ba_2Cu_3O_7$ were examined together with individual specimens of the separate oxide constituents (Y_2O_3, (purity 99.99%) BaO (purity >98%) and CuO (purity >99.0%)) used in the manufacture of the superconductor. In presenting the result those for the constituent oxides are discussed first. Two of these materials, yttrium oxide and barium oxide are usually classified as insulators and might therefore be thought of as broadly comparable with alumina. Cupric oxide, on the otherhand, is a semiconductor while little has yet been published regarding the dielectric properties of oxide superconductors.

With both Y_2O_3 and pure BaO, (Fig 7.4) the room temperature measurements reveal only a small amount of frequency dependence - in contrast to the behaviour of either alumina powder or magnesium oxide powder of about the same grain size. At 77K frequency independence of ϵ'_s is observed. For yttrium oxide the permittivity value of 77K is 11.3, while at room temperature and 3×10^4 Hz $\epsilon'_s = 8.88$. These values compare very favourably with the literature. Although there are no reports of measurements on bulk materials, there are several papers dealing with thin film yttrium oxide. Campbell [7.12] investigated the dielectric properties of thin films of Y_2O_3 fabricated by direct electron beam evaporation in an oxygen atmosphere; using bridge method he obtained an average permittivity value of $\epsilon' = 13.5 \pm 1.5$ at 1×10^3 Hz and 25°C. In similar studies of the dielectric properties of Y_2O_3

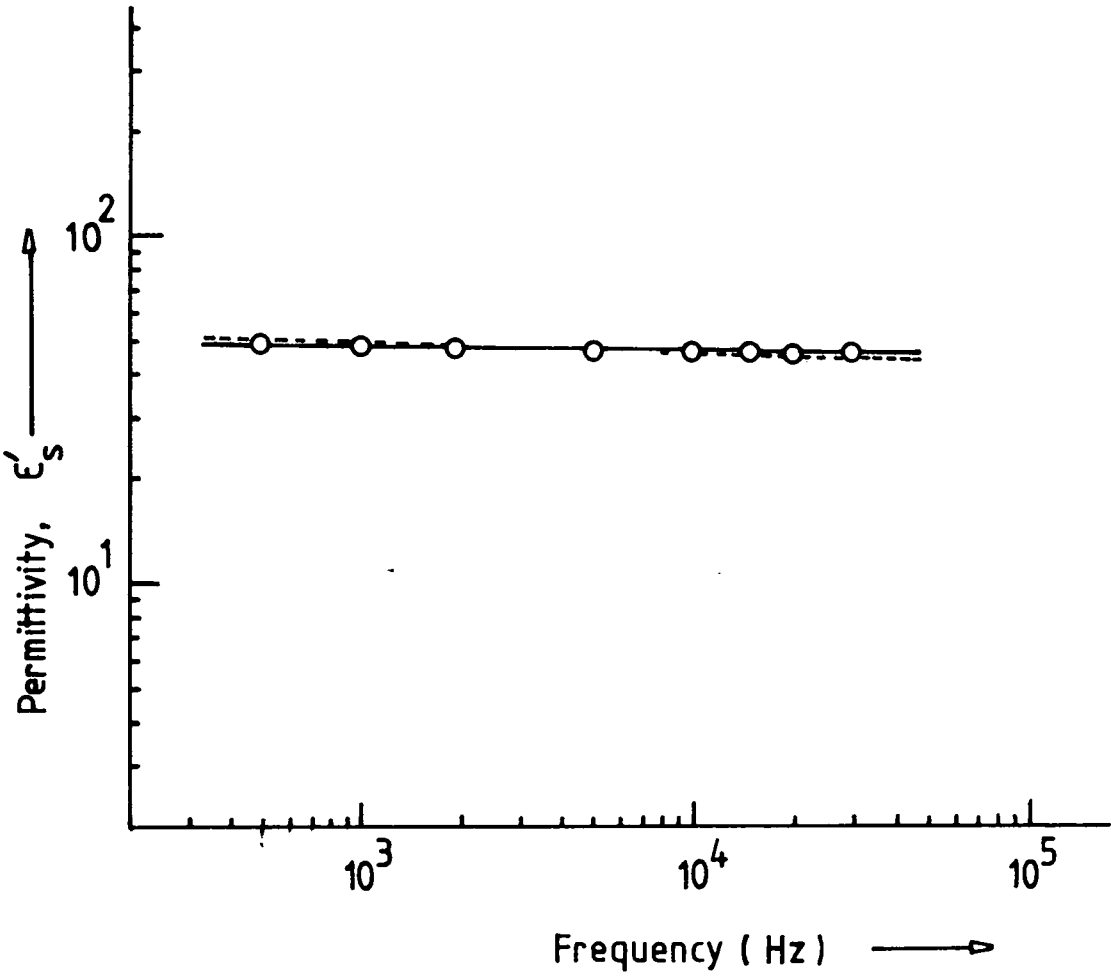

Fig. 7·3 Permittivity vs. frequency variation for magnesium - nitride powder ; 77K (——) and 20°C (- - - - -).

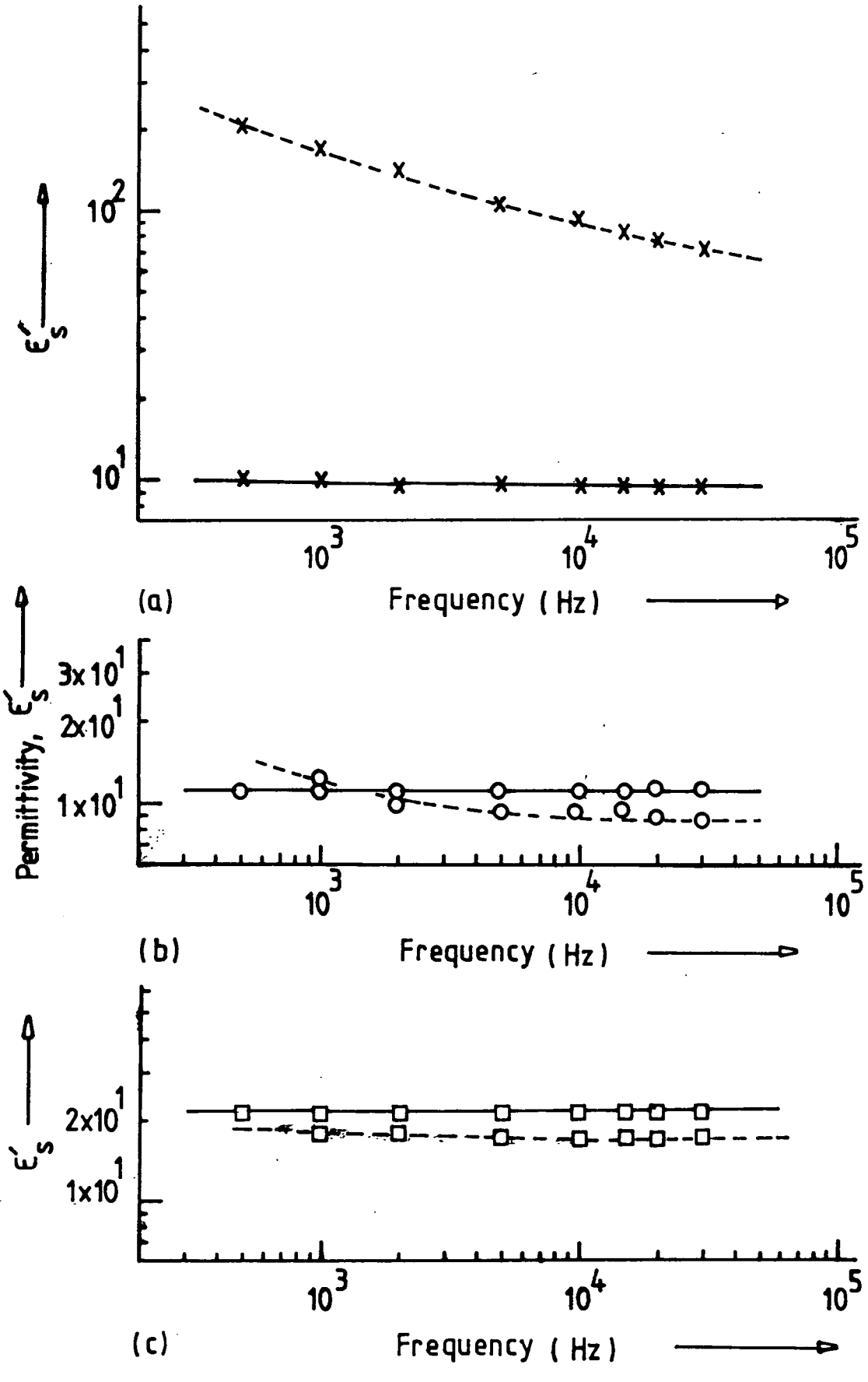

Fig. 7·4 Permittivity vs. frequency variation for (a) CuO, (b) Y_2O_3 and BaO powders; 20°C (----), and 77K (——).

thin films prepared by vacuum evaporation Tsutsumi [7.13] found a permittivity of 13 at room temperature. At optical frequenies, Riemann and Young [7.14] determined the refractive index of electron-beam evaporated yttrium oxide films and quoted a refractive index of 1.75 at 6328 Å; this gave a high frequency permittivity of $\epsilon' = 3.2$ which compared closely with the value of 3.05 obtained by ellipsometry. (It is of course to be expected that high frequency value of permittivity, ϵ', less than the value measured at relatively low frequencies).

For barium oxide powder the corresponding values are $\epsilon' = 16.6$ at 20°C and $\epsilon'_s = 21$ at 77K; both these values are substantially frequency independent. (It was noticeable, with this powder only, that there was some drift in the balance point with time indicating that there was a long-term relaxation of initial polarization on application of the a.c. voltage; the measurements are thus somewhat less reliable than those made on the other powders). The dielectric properties of single crystal BaO were measured by Bever and Sproull [7.15] over a frequency ragne 60 to 6×10^7 Hz and a temperature range -25° to 60°C. They found $\epsilon' = 34$ but commented on the rise in ϵ' at low frequencies observed at and above 20°C which was removed on cooling to -25°C when a frequency independent permittivity was observed between 60 and 6×10^7 Hz. Infrared measurements, also on crystals of BaO, were made by Galtier et al [7.16] who deduced low frequency permittivity value of 32.8 and 37.4 using two different theoretical models. The earlier value of 14.3 which is sometimes quoted is regarded by Bever and Sproull as unreliable because of difficulties in the experimental methods used by the earlier workers; it has however been given by Shepard Roberts [7.17] in discussing the dielectric constants and polarizabilities in simple crystals and barium titanate who gave the value $\epsilon' = 14.4$.

The cupric oxide powder , Fig 7.4, shows the largest room

temperature frequency dispersion of ϵ'_s of any of the constituent materials examined, i.e. from $\epsilon'_s = 224$ at 5×10^2 Hz to $\epsilon'_s = 75$ at 3×10^4 Hz and still falling. At 77K there is still a little variation, ϵ'_s varying from 10.9 at 5×10^2 Hz to 9.5 at 3×10^4 Hz, but the ϵ'_s values above about 2×10^4 are sensibly constant at about 9.5. There are quite a large number of references to the electrical properties of CuO dating from 1929 and corresponding to wide varieties of static permittivity. Rosenholtz and Smith [7.18] made measurements on powders at 60 Hz obtaining a permittivity of 16.2. Several other authors reported rather lower values. A recent detailed study was carried out by Nouguet [7.19] whose results were subsequently analysed by Weichman [7.20] in terms of small inclusions of copper embedded in the semiconducting material. Weichman states that at sufficiently low temperatures the permittivity for all the samples he examined the permittivity was about 7.5. The value of the permittivity at microwave frequencies has been given as 6.9 by Rau [7.21]. The values obtained in the present work fall well within the limits given in the literature.

Three samples of superconducting oxide powder, YBC01, YBC02 and YBC03, were next examined. Precise details of the chemical routes by which they had been prepared were not available although it was thought that they had been made from different starting materials via different preparative routes; thus the exact stoichiometry of the supposed $Y_1Ba_2Cu_3O_7$ product was unknown as was also the nature and amount of any impurity content. The ϵ'_s vs.frequency data obtained at 20°C and 77 K is shown in Fig 7.5. (It is to be noted that the superconducting transition temperature of YBC0 is 86K). At room temperature the space-charge polarization effects in YBC01 and YBC02 are roughly comparable and are relatively small in comparison to the variation found in YBC03. Some numerical data is given in Table 7.1 and it is

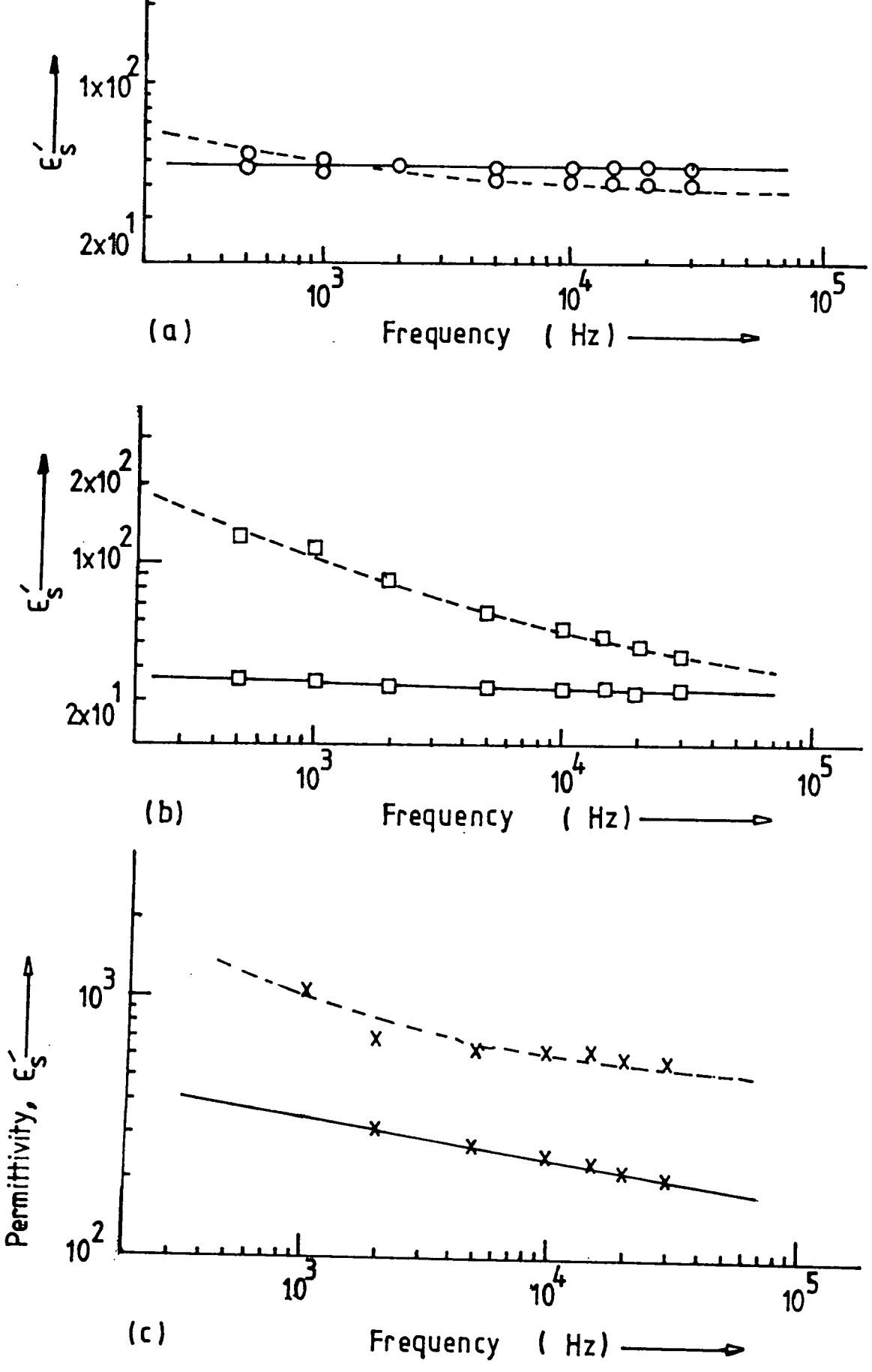

Fig. 7·5 Permittivity vs. frequency variation for superconducting powders: (a) YBCO1, (b) YBCO2 and (c) YBCO3 ; 20°C (----) and 77K (——).

TABLE 7.1: Permittivity data for three samples of YBCO made by different routes.

Frequency (KHz)	Permittivity, ϵ'_s YBCO1	YBCO2	YBCO3
Room temperature, 20°C			
0.5	53.5	127.3	-
1.0	50.7	112.1	1040.0
2.0	47.0	85.6	669.6
5.0	43.3	65.0	669.6
10.0	41.2	56.1	648.8
15.0	40.3	51.9	617.9
20.0	39.6	49.5	592.9
30.0	39.1	46.4	572.2
Low temperature, 77K			
0.5	48.7	34.5	-
1.0	48.2	33.9	-
2.0	47.6	33.5	304.8
5.0	46.9	32.9	289.1
10.0	46.5	32.4	253.6
15.0	46.3	32.3	234.1
20.0	45.7	32.1	219.9
30.0	45.8	32.0	202.2

seen that, taking the 3×10^4 Hz result the apparent ϵ'_s values are 37, 46 and 572 for YBC01, YBC02 and YBC03 respectively. This suggests that YBC03 differs very appreciably from the other two powders, possibly as a result of much increaseed impurity content. This difference is also evident in the 77K results which show that for both YBC01 and YBC02, there is only a very small frequency dispersion. For these, the average values of ϵ'_s over the frequency range 5×10^2 Hz to 3×10^4 Hz are about 46 and 32.5 respectively. In contrast YBC03 still gives very high values of ϵ'_s at 77K with strong frequency dispersion, i.e. 304 at 2×10^3 Hz falling to 202 at 3×10^4 Hz. Returning to the 77K data for YBC01 and YBC02 it may be pointed out that the values of ϵ'_s (46 and 32.5) observed are less than the high frequency room temperature values. At 77K these samples should be superconducting ($T_c \sim 86K$) and hence a large contribution to the permittivity might be expected due to the enhanced conductivity. This does not appear to be present. Preliminary measurements were also made of the dielectric loss ϵ''_s of the three superconducting samples at both room temperature and 77K. For the two samples YBC01 and YBC02 there was some variation in ϵ''_s with frequency at room temperature and at 2×10^3 Hz the respective values of tanδ were $(\tan\delta)^1_{R.T.} = 1.27 \times 10^{-1}$ and $(\tan\delta)^2_{R.T.} = 8.05 \times 10^{-1}$ showing that each could still be regarded as a dielectric though somewhat lossy; for the third sample YBC03 the corresponding values of tanδ at 2.0×10^3 Hz was $(\tan\delta)^3_{R.T.} = 2.17 \times 10^2$ indicating fairly convincingly that this sample was much more lossy and confirming the large difference deduced from the permittivity data (Fig.7.5c). At 77K the values of tanδ also at 2×10^3 Hz found for the three samples were $(\tan\delta)^1_{77K} = 2.74 \times 10^{-2}$, $(\tan\delta)^2_{77K} = 3.29 \times 10^{-2}$ and $(\tan\delta)^3_{77K} = 3.75$. In all cases it is clear that $(\tan\delta)_{R.T.} > (\tan\delta)_{77K}$, i.e. there is apparently no increase in dielectric loss on cooling below the

transition temperature of 86K. Since all the low temperature values of tanδ are less than the room temperature values for corresponding materials.

CHAPTER SEVEN

REFERENCES

7.1 A.K.Chaudhury and K.V.Rao, Physic.Stat.Sol., 32 (1969) 731.

7.2 K.V.Rao and A.Smakula, J.of Appl.Phys. 36 (1965) 2031.

7.3 J.S.Thorp and N.E.Rad, J.of Mat.Sci., Letters, 5 (1986) 157.

7.4 F.L.Weichman, Can.J.Phys., 51 (1973) 680.

7.5 D.C.Dube, J.Phys.D; Appl.Phys., 3 (1970) 1648.

7.6 A.K.Jonscher, Nature, 267 (1977) 673.

7.7 J.Fontanella et al, J.of Appl.Phys., 45 (1974) 2852.

7.8 K.M.Taylor and C.Lenie, J.Electrochem.Soc., 107 (1960) 308.

7.9 K.Lichtenecker, Physik.Z., 10 (1909) 1005.

7.10 J.S.Thorp and H.P.Buckley, J.of Mat.Sci., 8 (1973) 1401.

7.11 J.S.Thorp and N.E.Rad, J.of Mat.Sci., 16 (1981) 255.

7.12 C.K.Cambell, Thin Solid Films, 6 (1970), 197.

7.13 T.Tsutsumi, Japan J.of Appl.Phys., 9 (1970), 735.

7.14 E.Riemann and L.Young, J. of Appl.Phys., 44 (1973) 1044.

7.15 R.S.Bever and R.L.Sproul, Phys.Review, 83 (1951), 801.

7.16 M.Galtier, A.Montaner and G.Vidal, J.Phys.Chem.Solids, 33 (1972) 2295.

7.17 Shepard Roberts, Phys.Rev., 76 (1949) 1215.

7.18 J.L.Rosenholtz and D.T.Smith, An.Mineral, 21 (1936) 115.

7.19 C.Noguet, 1969. These, Universite de Strasbourg, Strasbourg, France.

7.20 F.L.Weichman, Can.J.Phys., 51 (1973) 680.

7.21 R.R.Rau, 1955. Dissertation, University of Pennsylvania, Philadelphia, Penn., U.S.A.

CHAPTER EIGHT

CONCLUSIONS

The work reported here divides into three main areas. These are:-

(a) the development and appraisal of techniques for dielectric measurement on both solids and powders at frequencies of between 5 x 10^2Hz and 3 x 10^4Hz and over temperature ranges of 77K to 293K and 20° C to 450°C.

(b) the examination of three materials, aluminium oxide, aluminium nitride and glass-on-metal, which are currently being considered for use as substrates in high performance microelectronic packaging.

(c) the use of the powder techniques developed under (a) to examine the dielectric behaviour of some oxide superconducting powders.

In this Chapter the main conclusions reached under these separate headings will be summarised and some suggestions made for possible future lines of work.

As regards techniques for specimen preparation and measurement it has been shown that adaptations of established methods for obtaining defined-area contacts can be made which are suitable for either polycrystalline samples or thin dielectric layers deposited on a large area conducting metal base. Silver paste and platinum paste were each found to be satisfactory for making the specimen-platinum wire contacts necessary in the low tempeature or high temperature measurements. The main development was that of the co-axial capacitor system for measurements on powders. This has the advantage that the powder can be packed more easily into a well-defined volume than is possible with parallel plate configurations and yields a compact, robust specimen assembly. With regard to measurements on powders, an important result was the demonstration that inter-granular space-charge polarization effects could be overcome by using low temperatures, thus enabling reliable dielectric data on powders to be obtained in the low frequency

region. The main limitation of the present work lies in its restriction to frequencies below about 10^7 Hz. There are many areas in which electronic ceramics are required for operation at much higher frequencies, e.g. microwave window and radome materials and packaging for high frequency and microwave microelectronics; the development of corresponding techniques for the higher frequency regions would form an important topic for future work.

Turning to the substrate materials for microelectronic packaging, the behaviour of various forms and qualities of alumina, aluminium nitride and cordierite glass-on-molybdenum has been examined in some depth. When pure (i.e. containing only trace levels of impurities) each of these gives a nearly frequency-independent variation of both permittivity and dielectric loss at room temperature. In each case the data fits the Universal law of dielectric response extremely well indicating that all may be regarded as hopping conductors. In the two materials where comparison was possible, i.e. for single crystal and polycrystalline alumina and for glass-on-metal as opposed to glass-ceramic on metal, there appeared to be little different between the respective results; this suggested that in high density sintered materials or in the transition from a glass to a glass ceramic, the presence of grain boundaries did not present a problem. However the effect of impurities (in aluminium oxide and aluminium nitride) was shown to be very significant both in respect of altering the permittivity and especially in increasing the dielectric loss; thus emphasised that dielectric measurements could form a very useful means of quality control both in the selection of starting materials and the subsequent processing and sintering stages of the production of high performance substrate materials. The temperature coefficients of permittivity, $[(\epsilon'-1)(\epsilon'+2)]^{-1}\left(\frac{\partial \epsilon'}{\partial T}\right)_p$ were also determined. Here it was found that at temperatures up to about 150°C the variation of ϵ'

with temperature was linear for both aluminium nitride and glass-on-molbydenum (pure) specimens and up to about 260°C for pure alumina; for each however, the linear range was limited and, at high temperatures the variation changed to an exponential form. Some comparative data is listed in Table 8.1. This has implications for the choice of the most suitable substrate bearing in mind the operational temperature range specification required, Al_2O_3 gives the least change in ϵ' over the widest temperature range. It should be noted also that impurities have a major effect in reducing the temperature at which the exponential rise begins. The actual choice of substrate materials depends on many factors, not solely on their dielectric properties. Thermal expansion coefficient matching is important as is also thermal conductivity and chemical stability. The three substrate materials examined here were compatible with silicon technology. The demand for high performance microelectronic packages which are capable of higher frequency operation is increasing and it seems likely that for these silicon technology may be replaced by gallium arsenide technology. If this turns out to be the case, a new series of substrate will be required which are compatible with gallium-arsenide and this could form an important new area of investigation.

It is appropriate to add a few comments on the results obtained with the superconducting oxide ceramic powders (YBCO) since, despite the voluminous literature on the new-superconductors, there are very few references to their dielectric properties. The first point to note is that, although the d.c. resistance of pressed pellets of the material is usually only a few ohms, there was no undue difficulty with these powders in obtaining good bridge balances on both the C and G ranges, i.e. the powders behaving as reasonable though rather lossy dielectrics at room temperature. The transition temperature for YBCO is near 86K, so at 77K the sample should be superconducting. Taking a

TABLE 8.1: Summary of dielectric parameters of Al_2O_3, AlN and glass-on-molybdenum substrates.

Frequency (1.0 KHz)	Al_2O_3		AlN		Glass-on-Mo
	Pure	Impure	Pure	Impure	Pure
ϵ' (20°C)	10.2	12.2	9.2	9.8	6.5
Tanδ (20°C)	1.4×10^{-3}	1.3×10^{-1}	2.17×10^{-3}	2.0×10^{-2}	4.0×10^{-3}
$[(\epsilon'-1)(\epsilon'+2)]^{-1}\left(\frac{\partial\epsilon'}{\partial T}\right)_p$ (/K) (20°C-150°C)	9.31×10^{-6}	1.2×10^{-4}	1.1×10^{-5}	2.05×10^{-5}	1.25×10^{-5}
Linear-exponential transition temperature (°C)	260	Non-linear above 100K	160	130	130

simple model based on an analogy with a metal loaded composite dielectric one might expect therefore to see some increased permittivity and a large increase in dielectric loss as the powder is cooled through the transition temperature. This was not observed. Time restrictions did not permit the making of independent checks of the transition temperature of the specimens available, nor of a more detailed theoretical survey of the behaviour to be expected. The topic is important however because of the potential application of the new superconductors in r.f. shielding and warrants much closer examination.